



Structural Integrity Assessment of Engineering Components under Cyclic Loading at High Temperature

Nak-Kyun Cho

Structural Integrity and Lifetime Assessment Research Group

Department of Mechanical and Aerospace Engineering

University of Strathclyde, Glasgow

2019

This thesis is the result of the author's original research. It has been composed by the author and has not been previously submitted for examination which has led to the award of a degree.

The copyright of this thesis belongs to the author under the terms of the United Kingdom Copyright Acts as qualified by University of Strathclyde Regulation 3.50. Due acknowledgement must always be made of the use of any material contained in, or derived from, this thesis

Signed:

Date:

Acknowledgements

I would like to praise and to send all glory to my Lord Jesus Christ for His abundant grace and love for the accomplishment of this thesis. Without His guidance, I confess that my family and I could not manage well to live here in the United Kingdom until my study was finished and that I was able to submit this thesis with his grace.

Firstly, I would like to thank my supervisor Dr Haofeng Chen for his support and guidance. Dr Chen is the primary supervisor of my PhD study at the University of Strathclyde and he provided me with supports in supervising my research works and travel grants for my conference attendance.

I would like to thank my colleagues in Structure Integrity and Lifetime Assessment research group and in Mechanical and Aerospace Engineering department, and academic visitors from East China University of Science Technology, who all made my PhD life joyful and meaningful. I wish the best luck to all my colleagues for the bright futures.

I would also like to thank external advisors, Mr Spindler and Prof Ainsworth, for their advice and answers to my academic questions raised during my PhD study and to thank Engineering Analysis Service Limited for providing me industrial data so that I can compare analysed results.

I would like to express my gratitude to my dear parents in Korea and U.K. and siblings (Yong-Kyun, Se-il, Jae Eun, and Young Kuk), close friends, and church members who all offered a great support and encouragement during the course of this study. Special thanks to Mr Joohyun Ahn who encourage my family every time he visited Glasgow.

Finally, my sincerest goes to greatly thank to my family. Especially, I am so grateful that my two children, Eunyu and Eunsung, have been growing well since they had overcome the hard time. Both of you are treasures of my life. I love you both so much! I want to say to my beloved wife that I will love you forever and I could not finish this study without your love and patience.

Abstract

Structural integrity assessment is essential for many industries, especially for industries which have machinery components and structures in operation at high temperature. Nuclear power plant industry is one of a good example, and they have planned to introduce the very high temperature reactor to increase efficiency. The high temperature operations may improve power productions but cause severe structural problems due to creep, fatigue, creep-fatigue failure mechanisms. Hence, performing structural integrity assessment accurately and developing effective assessment methods are vital tasks in these industries.

In order to contribute to the research field of the high temperature industries, this thesis have achieved the following three main objectives:

Firstly, this thesis provides insights into cyclic plasticity and creep-cyclic plasticity behaviours of high temperature engineering problems which have not been explored in the past. A numerical study investigates cyclic plasticity behaviours of 90° back-to-back pipe bends under cyclic thermo-mechanical load and constant pressure. Another numerical study investigates creep-cyclic plasticity behaviours of Particle Reinforced Titanium Matrix Composites (PRTMCs), which is a futuristic engineering material, subjected to a cyclic thermo-mechanical load. Both numerical studies are carried out using a novel direct method called The LMM Framework.

Secondly, this thesis has enhanced the LMM Framework allowing to evaluate the structural response in non-isothermal condition and multiple dwell periods. In order to demonstrate this, the extended method is applied to analyse creep-cyclic plasticity behaviour of a superheater outlet tube plate subjected to a cyclic thermo-mechanical load, and to evaluate creep-fatigue damage endurance.

Finally, this thesis introduces a critical high temperature failure mechanism, named as Structural Creep Recovery Mechanism (SCRM), utilising a numerical technique involving cyclic creep and plastic behaviours. This study identifies the cause of this critical failure mechanism and defines factors that have substantial influences on the structural integrity in the presence of SCRM. Chaboche nonlinear kinematic hardening model and temperature dependent material parameters are employed to demonstrate the effectiveness of SCRM in practical problems.

Achievements (Publications and Awards)

Peer Reviewed Publications

1. **Cho, N-K.,** & Chen, H. Investigation of structural creep strain recovery and its impact on structural integrity. 24th International Conference on Structural Mechanics in Reactor Technology, Volume 1, Page 655-665.
2. **Cho, N-K.,** & Chen, H. Shakedown, ratchet, and limit analyses of 90° back-to-back pipe bends under cyclic in-plane opening bending and steady internal pressure. European Journal of Mechanics - A/Solids, Volume 67, January 2018, Pages 231-242.
3. **Cho, N-K.,** Chen, H., Boyle, J., & Xuan, F-Z. Enhanced fatigue damage under cyclic thermo-mechanical loading at high temperature by structural creep recovery mechanism. International Journal of Fatigue, Volume 113, August 2018, Pages 149-159.
4. **Cho, N-K.,** & Chen, H. Cyclic plasticity behavior of 90° back-to-back pipe bends under cyclic bending and steady pressure. 26th International Conference on Nuclear Engineering, Volume 9, ICONE26-82386. July 2018.
5. Giugliano, D., Barbera, D., Chen, H., **Cho, N-K.,** & Liu, Y. Creep-fatigue and cyclically enhanced creep mechanisms in aluminium based metal matrix composites. European Journal of Mechanics - A/Solids, Volume 74, March–April 2019, Pages 66-80.
6. Giugliano, D., **Cho, N-K.,** Chen, H. Gentile, L. Cyclic plasticity and creep-cyclic plasticity behaviours of the SiC/Ti-6242 Particulate Reinforced Titanium Matrix Composites under thermo-mechanical loadings. Composite Structure, In Press, Accepted Manuscript, March 2019.
7. **Cho, N-K.,** Chen, H., Mackenzie, D., Giugliano, D. Investigating the effects of cyclic thermo-mechanical loading on cyclic plastic behaviour of a ninety-degree back-to-back pipe bend system. Journal of Pressure Vessel Technology, In Press, Accepted Manuscript, March 2019.
8. **Cho, N-K.,** Wang, R., Ma, Z., Chen, H., Xuan, F-Z. Creep-fatigue endurance of a superheater tube plate under non-isothermal loading and multi-dwell condition. International Journal of Mechanical Sciences, Under Review.

Awards

1. Engineering the Future (ETF) Studentship, University of Strathclyde, July 2015.
2. Postgraduate Research Travel Award, University of Strathclyde, Feb 2017.
3. Qualified Student Award, ASME 26th International Conference on Nuclear Engineering, Apr 2018.
4. Akiyama Medal (Best Student Award), ASME 26th International Conference on Nuclear Engineering, July 2018.



ICONE-26 ORGANIZING COMMITTEE

Presents a
Certificate of Appreciation
to

Nak-Kyun Cho

For the paper:

**Cyclic Plasticity Behavior of 90° Back-to-Back Pipe Bends
Under Cyclic Bending and Steady Pressure
ICONE26-82386**

Selected as a

**Winner in the
ICONE-26 Student Best Paper Competition:
UK / Europe**

at the

26th International Conference on Nuclear Engineering

ICONE-26

London, United Kingdom

July 22 - 26, 2018

Lei Zengguang
Chair, Chinese Nuclear Society

Guoqiang Wang
Chair, ASME Nuclear Engineering Division

Nobuyuki Ueda
Chair, JSME Conference

Shripad Revankar
Chair, Technical Program

Contents

Abstract	IV
Achievements (Publications and Awards).....	V
Contents	VII
List of Figures.....	X
List of Tables	XV
Nomenclatures	XVII
Acronyms.....	XXIII
1. Introduction.....	1
1.1 Research Background.....	1
1.2 Objectives of the thesis	3
1.3 Outline of the thesis	4
1.4 Engineering Units.....	5
2. High Temperature Component Design and Design Assessment Codes	6
2.1 Introduction	6
2.2 Structural Responses under Cyclic Load at High Temperature.....	6
2.2.1 Cyclic Plasticity.....	6
2.2.1.1 Elastic Shakedown	7
2.2.1.2 Plastic Shakedown	8
2.2.1.3 Ratchetting.....	13
2.2.2 Creep-Cyclic Plasticity	13
2.2.3 Creep-Fatigue Damage Evaluations.....	16
2.3 Design Codes and procedures for Assessing Structural Integrity under High Temperature.....	20
2.3.1. R5 Assessment Procedure for the High Temperature Response of Structure.....	20
2.3.2. ASME BPVC Section III Subsection NH	28
2.4 Chapter Summary	39
3. Advanced Numerical Direct Method.....	40
3.1 Introduction	40
3.2 Shakedown Analysis	41
3.3 Direct Steady Cycle Analysis (DSCA).....	43
3.4 Extended Direct Steady Cycle Analysis (eDSCA).....	44
3.4.1 Original numerical procedure for creep strain and flow stress.....	47

3.4.2	The modified numerical procedure for creep strain and flow stress	48
3.5	Chapter Summary	50
4.	Cyclic Plasticity of 90° Back-to-Back Pipe Bends under Cyclic Thermal Loading, Cyclic Bending, and Constant Internal Pressures	51
4.1	Introduction	51
4.2	Finite Element Model	52
4.2.1	Geometry of the 90° back-to-back pipe bends	52
4.2.2	Material properties and Boundary and loading conditions.....	53
4.3	Cyclic In-Plane Bending and Constant Internal Pressures.....	55
4.3.1	Limit load, shakedown limit, and ratchet limit boundaries.....	55
4.3.2	Verification of results	57
4.3.3	Parametric studies and discussions.....	59
4.3.3.1	Geometry effects of the pipe bends structure	59
4.3.3.2	Effect of the horizontal straight pipe length.....	63
4.4	Cyclic Out-of-Plane Bending and Constant Internal Pressures.....	65
4.4.1	Limit load, shakedown limit and ratchet limit boundaries.....	65
4.4.2	Verification of results	66
4.4.3	Parametric studies and discussions.....	68
4.4.3.1	Geometry effects of the pipe bends.....	68
4.4.3.2	Effects of the horizontal straight pipe length	71
4.5	Cyclic Thermal Loading, Cyclic Out-of-Plane Bending and Constant Internal Pressures.....	74
4.5.1	Geometry effects of the pipe bends.....	77
4.6	Chapter Summary	79
5.	Creep-Cyclic Plasticity Behaviours of Metal Matrix Composite.....	81
5.1	Introduction	81
5.2	Finite Element Model	82
5.3	Creep-cyclic plasticity of PRTMCs under thermo-mechanical loading.....	86
5.3.1.	Effect of spatial particle distribution on the creep-cyclic plasticity response.....	87
5.3.2.	Effect of varying dwell time and tensile load level on the creep-cyclic plasticity response	89
5.3.3.	Effect of volume fractions on the creep-cyclic plasticity response for a fixed particle arrangement	91
5.4	Chapter Summary	93

6. Creep-fatigue endurance of a superheater outlet tube plate under non-isothermal loading and multi-dwell condition.....	94
6.1 Introduction	94
6.2 Investigation Procedures.....	96
6.3 Problem Description.....	97
6.3.1. Finite element model and boundary conditions.....	97
6.3.2. Material properties and modelling parameters	100
6.4 Numerical Results and Discussions.....	106
6.4.1. Creep-cyclic plasticity behaviour.....	106
6.4.2. Creep-fatigue damage endurance.....	112
6.5 Chapter Summary	118
7. Advanced Numerical Investigations of a Critical Failure Mechanism at Elevated Temperature.....	120
7.1 Introduction	120
7.2 Problem Description and the Finite Element Model	122
7.2.1 Geometry and Loadings for the Analysis.....	122
7.2.1 Material properties and FE model.....	123
7.3 Results and Parametric Studies	125
7.3.1 Investigation of the Structural Creep Recovery Mechanism	125
7.3.2 Effect of Dwell Time and Load Level on the Structural Creep Recovery Mechanism.....	129
7.3.3 Effect of Temperature Dependent Parameters on the Structural Creep Recovery Mechanism	133
7.3.4 Effect of Practical Hardening Parameters on the Structural Creep Recovery Mechanism	136
7.4 Discussions	139
7.4.1 Practical Problems Involving the Structural Creep Recovery Mechanism.....	139
7.4.2 Limitations of the Elastic Follow-up Factor in the Structural Creep Recovery Mechanism	140
7.4.3 Structural Integrity Assessment in the Presence of the Structural Creep Recovery Mechanism	142
7.2 Chapter Summary	144
8. Conclusions	146
8.1 Future Work.....	148
References	150

List of Figures

Figure 1.1 (a) creep crack in the fir-tree bottom serration [7] and (b) creep-fatigue damage in the gas turbine blade[8].....	2
Figure 2.1 Structural response subjected to cyclic loading condition.....	7
Figure 2.2 Low cycle fatigue $\frac{\Delta\varepsilon}{2} - N_f$ curve.....	9
Figure 2.3 Basic creep curve for constant stress and temperature.....	14
Figure 2.4 Different creep-cyclic plasticity responses at tensile creep peak [39]: (a) elastic response, (b) elastic shakedown, (c) creep enhanced plasticity, and (d) creep enhanced plastic shakedown[39].....	16
Figure 2.5 The creep-fatigue damage envelope.....	17
Figure 2.6 Procedures of creep-fatigue damage evaluation.....	18
Figure 2.7 Effective creep stress parameter Z for simplified inelastic analysis using test b-1 and b-3 [11].....	34
Figure 2.8 Effective creep stress parameter Z for simplified inelastic analysis using test b-2 [11].	35
Figure 2.9 Creep-fatigue damage envelope provided in ASME NH [11].....	36
Figure 4.1 Geometry of the 90° back-to-back pipe bends with two attached vertical straight pipe sections.....	53
Figure 4.2 Full model of 90° back-to-back pipe bends with 3D solid elements meshed.	53
Figure 4.3 (a) loading paths for the classic bree problem and (b) a loading domain for the three load combinations.	55
Figure 4.4 Equivalent stress contours from linear elastic stress analyses for a) in-plane opening bending moment M_L b) internal pressures P_L	56
Figure 4.5 The limit, shakedown limit, and ratchet limit boundaries of the pipe bends structure under cyclic in-plane opening bending and constant internal pressures.	56
Figure 4.6 Plastic strain increment history (<i>PEMAG</i>) over number of loading instance for cyclic loading points (A, B, C, D, and E).....	58
Figure 4.7. Geometries of the pipe bends structure for the parametric studies; (a) fixed $r/t=10$ with varying R/r ratio and (b) fixed $r/t=10$ with varying length L_m	59
Figure 4.8 The effects of varying R/r with (a) $r/t=5$, (b) $r/t=10$, and (c) $r/t=20$ on the limit load, shakedown limit and ratchet limit boundaries.	61

Figure 4.9. Reverse plasticity limit and limit pressure trends with respect to bend characteristic in a rage from $h = 0$ to $h = 1$	62
Figure 4.10 The effects of varying length L_m with (a) $r/t=5$, (b) $r/t=10$, and (c) $r/t=20$ under the cyclic in-plane bending and constant internal pressures.....	64
Figure 4.11 Equivalent stress contours from linear elastic stress analyses for (a) out-of-plane bending moment M_L (b) internal pressures P_L	65
Figure 4.12 The limit, shakedown limit, and ratchet limit boundaries of the pipe bends structure under cyclic out-of-plane opening bending and constant internal pressures.....	66
Figure 4.13 Plastic strain increment history (<i>PEMAG</i>) of cyclic loading points (A, B, C) in Figure 4.12.....	67
Figure 4.14 Effect of varying R/r with (a) $r/t=5$, (b) $r/t=10$, and (c) $r/t=20$ under the cyclic out-of-plane bending and constant internal pressures.....	69
Figure 4.15 Reverse plasticity limit and trends of the ratio $RT = RP_{OP}/RP_{IP}$ against the bend characteristic in a rage from $h = 0$ to $h = 1$	71
Figure 4.16 Effect of varying length L_m with (a) $r/t=5$, (b) $r/t=10$, and (c) $r/t=20$ under the cyclic out-of-plane bending and constant internal pressures.....	73
Figure 4.17 Linear elastic solutions; (a) max. principal stress under thermal load, (b) equivalent stress under out-of-plane bending moment, and (c) equivalent stress under internal pressures.....	75
Figure 4.18 (a) shakedown and ratchet boundaries of the 90° back-to-back pipe bends subjected to cyclic thermal load, cyclic out-of-plane bending and constant internal pressure and (b) shakedown domain in the three-dimensional loading space.	75
Figure 4.19 Shakedown and ratchet boundary of the pipe bends ($r/t=5$) subjected to cyclic thermal load and constant internal pressure with respect to varying R/r ratio.....	77
Figure 4.20 Plastic strain history (<i>PEMAG</i>) of R/r ratio of 3 and 4 at cyclic loading point d and of R/r ratio of 5 at cyclic loading point e.	78
Figure 4.21 Shakedown boundary of the pipe bends ($r/t=5$) subjected to cyclic thermal load and constant internal pressure and bending moment with respect to varying R/r ratio.....	79
Figure 5.1 Groups of nodes on the boundary faces of the RVEs (a) inner face nodes, (b) inner edge nodes and (c) corner nodes [91].	82

Figure 5.2 Typical FE models with six particles and (a) $V_f=10\%$, (b) $V_f=14\%$, (c) $V_f=25\%$ [91].	83
Figure 5.3 (a) RVE with tensile mechanical load $\sigma_p(t)$ and cyclic thermal load $\Delta\theta(t)$ and (b) load history applied [91, 92].	83
Figure 5.4 Shakedown boundaries for different particle arrangements with N_{part} 2, 4, 6, 8, and 10 and (a) $V_f=10\%$, (b) $V_f=14\%$ and (c) $V_f=25\%$ [91, 92].	86
Figure 5.5 Creep strain contours for the micro-scaled SiC-Ti6242 prtmcs subjected to a cyclic load point P2 for a dwell time of 10hrs; analysed by (a) abaqus step-by-step method and (b) the LMM eDSCA.	87
Figure 5.6 Steady state hysteresis loops of the RVE models subject to cyclic loading P2 for dwell time 10hrs; (a) $N_{part}=10$ with $V_f=10\%$, (b) $N_{part}=2$ with $V_f=25\%$ and (c) $N_{part}=6$ with $V_f=25\%$.	88
Figure 5.7 Steady-state hysteresis loops of an RVE model that has $N_{part} = 6$ with $V_f=10\%$ for variations of dwell 1hr, 10hrs, and 100hrs at cyclic load point; (a) P1, (b) P2 and (c) P3.	89
Figure 5.8 Maximum principal stress distributions of a RVE model $N_{part} = 6$ with $V_f = 10\%$ for dwell time 10hrs: (a) $\sigma_p = 0$ and (b) $\sigma_p = 0.15\sigma_{p0}$.	90
Figure 5.9 Steady-state hysteresis loops of RVE models that have a fixed particle arrangement subjected to cyclic loading P2 and dwell time of 10hrs with variations of volume fractions: (a) $N_{part}=6$ and (b) $N_{part}=10$.	92
Figure 6.1 A proposed flow chart for the study of the tube plate through the modified LMM eDSCA method.	96
Figure 6.2 Simplified 3-dimensional tube plate model with certain surfaces selected: (a) internal surface, (b) external surface, (c) tube holes, and (d) sheath tube weld surface.	97
Figure 6.3 (a) side view of the tubeplate model, (b) front view of the tubeplate model, and (c) meshed tube plate.	98
Figure 6.4 Loading waveform under multi-dwell for six months operations.	99
Figure 6.5 Inelastic strain energy which leads to the creep damage: a) $\bar{\sigma}_s > \bar{\sigma}_c$ and b) $\bar{\sigma}_c > \bar{\sigma}_s$.	105
Figure 6.6 Creep-fatigue damage envelope for type 316 stainless steel in ASME NH design codes.	106
Figure 6.7 Elastic stress solutions: (a) mechanical load only, (b) thermal load only, and (c) both mechanical and thermal loads.	107

Figure 6.8 (a) temperature distribution at the 1 st dwell, (b) non-isothermal creep parameters at the 1 st dwell, (c) temperature distribution at the 2 nd dwell, and (d) non-isothermal creep parameters at the 2 nd dwell.....	108
Figure 6.9 Equivalent stress distribution contours: (a) the 1 st loading, (b) the 1 st dwell, (c) the 2 nd loading, (d) the 2 nd dwell, and (e) unloading.....	109
Figure 6.10 Effective creep strain increment contours at: (a) the 1 st dwell (element number: 15107) and (b) the 2 nd dwell (element number: 2).....	110
Figure 6.11 Saturated stress-strain hysteresis loops for the critical locations: (a) element 15107 and (b) element 2.	110
Figure 6.12 Creep damage contours at the 1 st dwell: (a) TF model with σ_{RUP} , (b) DE model with MDF, and (c) SEDE model with MDF_{WEN}	113
Figure 6.13 Creep damage contours at the 2 nd dwell: (a) TF model with σ_{RUP} , (b) DE model with MDF, and (c) SEDE model with MDF_{WEN}	113
Figure 6.14 Maximum principal stress contours at dwell periods: (a) start of the 1 st dwell, (b) end of the 1 st dwell, (c) start of the 2 nd dwell, and (d) end of the 2 nd dwell.	114
Figure 6.15 (a) total strain range and (b) fatigue damage per cycle.....	115
Figure 6.16 Design fatigue curve $\Delta\varepsilon - N_d$ for 316 stainless steel in ASME NH[11].....	116
Figure 6.17 Total damage per cycle: (a) TF model with σ_{RUP} , (b) DE model with MDF, and (c) SEDE model with MDF_{WEN}	116
Figure 7.1 (a) geometry of the holed plate and loading conditions and (b) FE meshed model.	122
Figure 7.2 Loading instances: (a) mechanical loading and (b) thermal loading.....	122
Figure 7.3 Shakedown and ratchet limit boundaries for the holed plate subjected to the thermo-mechanical loads and six load cases for investigations of the structural creep recovery mechanism.....	123
Figure 7.4 von-Mises stress distribution at load case 1 for dwell time of 200hrs at the last loading cycle: (a) loading, (b) creep, (c) unloading, and (d) corresponding creep strain increment.	125
Figure 7.5 Creep stress relaxation curves and creep strain increment with load case 1 for a dwell time of 200hrs at the point of interest.	126
Figure 7.6 Stress component σ_{11} distributions for each load instance with load case 1 for dwell time of 200hrs: (a) loading, (b) creep, (c) unloading.	127

Figure 7.7 Elastic stress solutions: (a) stress component σ_{11} from monotonic thermal gradient only with $\Delta\theta=0.7$ and (b) stress component σ_{11} from monotonic mechanical load only with $\sigma_p=0.5 \sigma_{p0}$	128
Figure 7.8 Response of steady state stress-strain hysteresis loop corresponding to load case 1 for a dwell time of 200hrs.....	129
Figure 7.9 Response of steady state stress-strain loop corresponding to load case 1 for a dwell time of 100hrs and 200hrs each.....	130
Figure 7.10 Response of steady state stress-strain loop corresponding to load cases 1, 2, and 3 for a dwell time of 200hrs.....	131
Figure 7.11 Creep stress relaxation curves for a dwell time of 200hrs per load case.	132
Figure 7.12 Creep stress relaxation curves in load case 3 for a dwell time of 60,000hrs.	133
Figure 7.13 Response of steady state stress-strain loop corresponding to load case 5 for dwell time of 200hrs.	135
Figure 7.14 Cyclic test result at 600°C [116] and simulation result, $\Delta\varepsilon = \pm 0.6\%$	137
Figure 7.15 Structural responses in a transition from the first cycle to the saturated cycle at the 10 th cycle for load case 6.....	139
Figure 7.16 Definition of general elastic follow-up factor Z.....	141

List of Tables

Table 4.1. Key dimensions of the 90° back-to-back pipe bends and the two straight pipes (all dimensions in mm).	53
Table 4.2. Temperature dependent yield stress.	54
Table 4.3. Reference loads of cyclic bending moment and constant internal pressure and axial pressure with respect to r/t ratio.	59
Table 5.1 Mechanical properties at 500°C.	85
Table 5.2 Creep parameters.	85
Table 5.3 Creep strain and ratchetting strain from the cyclic creep and plastic analyses of all the RVE models.	88
Table 5.4 Creep and ratchetting strain from the creep behaviour analyses of $N_{part} = 6$ with $V_f = 10\%$	90
Table 5.5 Creep and ratchetting strains for $N_{part} = 6$ and $N_{part} = 10$ of RVE models that have a fixed particle arrangement subjected to cyclic loading P2 and dwell time of 10hrs with variations of volume fractions.	92
Table 6.1 Geometry dimensions of the tube plate (all dimensions in mm)	98
Table 6.2 Temperature dependent yield stresses of Type 316 stainless steel	100
Table 6.3 Creep parameters for calculating creep strain.	100
Table 6.4 Material constants for TF model of Type 316 stainless steel.	102
Table 6.5 Material constants for creep ductility of Type 316H stainless steel [99].	103
Table 6.6 Material constants for SEDE model of Type 316H stainless steel.	104
Table 6.7 Coefficient of Eq.(6.13).	106
Table 6.8 Stresses and creep strain histories for the element 15107 at the 2 nd dwell: creep stress $\bar{\sigma}_c$, effective creep strain $\bar{\epsilon}^c$, principal stresses $\sigma_1, \sigma_2, \sigma_3$ and mean stress σ_m	111
Table 6.9 Comparisons of creep-fatigue damage lives for six months operation.	118
Table 7.1 Stress history between signed von-mises stress and stress component σ_{11}	127
Table 7.2 Comparison of critical values and features with load case 1 for different dwell time.	130
Table 7.3 Comparison key values and feature for dwell time of 200hrs with different mechanical load cases.	131
Table 7.4 Temperature dependent material parameters and creep material constants of the SS316.	134

Table 7.5 Key values and feature with load case 5 for dwell time of 200hr.	135
Table 7.6 Material properties for the simulation.	137
Table 7.7 Key values and feature at the initial cycle and saturated cycle with load case 6 for a dwell time of 10hr.	138

Nomenclatures

$\dot{\bar{\epsilon}}^c$	Effective creep strain rate
\dot{w}_{in}	Inelastic strain energy density rate
$\bar{\epsilon}^c$	Effective creep strain
$\bar{\epsilon}_f^c$	Creep ductility considering effects of multiaxial ductility factor
$\bar{\sigma}_c$	Effective end of creep stress
$\bar{\sigma}_s$	Effective start of creep stress
$\Delta\sigma_{ML}$	Cyclic mechanical load by bending moment
A^*	Frequency factor for A
\bar{E}	Effective Young's modulus
L_m	Horizontal pipe length between pipe bends
R_{gas}	Global gas constant
ϵ_p	Plastic strain
θ_0	Temperature at outside surface of the holed plate
B^*, m^*	Material parameters for uniaxial creep ductility
B_1, B_2	Material constants for w_f
C_0, c_1, β_0, b_1	Coefficients for the unified creep-fatigue equation
C_k, α_k	Material constants for kinematic hardening
D_1, D_2, D_3	Dummy nodes
D_c	Creep damage
D_f	Fatigue damage
D_m	Mean pipe diameter
F_A	Axial tension

L_{RVE}	Length of Representative Volume Element(RVE)'s edge
M_L	Limit bending moment
N_0	Number of cycles to initiate a crack having size of a_0 at total strain range
N_{cf}	Number of cycles to creep-fatigue damage failure
N_d	Number of designed allowable cycles
N_f	Number of cycles to fatigue failure
N_{part}	Number of particle of PRTMCs RVE
P_L	Limit pressure
P_{gas}	Gas pressure
P_{steam}	Steam pressure
Q_∞	Maximum change in the yield surface size
Q_{eng}	Activation energy
RP_{IP}	Reverse plasticity limit under cyclic in-plane bending
RP_{OP}	Reverse plasticity limit under cyclic out-of-plane bending
T_{gas}	Gas temperature
T_{steam}	Steam temperature
V_f	Volume fractions of PRTMCs RVE
X_k	Back stress for kinematic hardening
a_0	Crack size
a_i	Nucleation of a defect size
d_{Total}	Total creep-fatigue damage per cycle
d_{Total}^{ASME}	Total creep-fatigue damage per cycle with ASME NH designed fatigue curve
d_{Total}^{MUSM}	Total creep-fatigue damage per cycle with the Modified Universal Slope Method

$d_{Total}^{unified}$	Total creep-fatigue damage per cycle with the unified creep-fatigue equation
d_c	Creep damage per cycle
d_c^{1st}	Creep damage at the 1 st dwell
d_c^{2nd}	Creep damage at the 2 nd dwell
$d_c^{DE \cdot MDF}$	Creep damage per cycle based on Ductility Exhaustion method with the multiaxial ductility factor
$d_c^{SEDE \cdot MDF_{WEN}}$	Creep damage per cycle based on Strain Energy Ductility Exhaustion method with the multiaxial ductility factor proposed by Wen <i>et al.</i>
$d_c^{TF \cdot \sigma_{RUP}}$	Creep damage per cycle based on Time Fraction rule with the multiaxial creep stress
d_f	Fatigue damage per cycle
d_f^{ASME}	Fatigue damage per cycle according to ASME NH designed fatigue curve
d_f^{MUSM}	Fatigue damage per cycle based on the Modified Universal Slope Method
t_1, t_2	Time point at loading instance and unloading instance respectively
t_f	Creep rupture time
t_r	Dwell time for creep strain being fully recovered
t_s	Dwell time for the structural creep recovery mechanism to occur
\dot{u}	Displacement rate
u_i	Nodal variable at a specific node
w_f	Failure strain energy density
$\dot{\epsilon}$	Strain rate
ϵ_{BR}^c	Creep strain before the structural creep recovery mechanism to occur
ϵ_L	Lower shelf creep ductility at high strain rate
ϵ_L^e	Elastic strain at loading instance
ϵ_L^p	Plastic strain at loading instance
ϵ_R^c	Creep strain in the process of the structural creep recovery mechanism to occur

ε_U	Upper shelf creep ductility at high strain rate
ε_{UL}^e	Elastic strain at Unloading instance
ε_{UL}^p	Plastic strain at Unloading instance
ε_f	Fatigue ductility
ε_f^c	Creep ductility
σ_{PL}	Constant mechanical load by internal pressure
$\bar{\sigma}$	Effective stress
σ^0	Yield surface size of isotropic hardening
$\sigma_1, \sigma_2, \sigma_3$	Maximum, Medium, Minimum Principal stresses
σ_{11}	Stress component in x-axis
σ_B	Tensile strength of a material at room temperature
σ_P	Tensile mechanical load
$\sigma_P(t)$	Tensile mechanical load over time period
σ_{P0}	Reference tensile mechanical load
σ_{RUP}	Multiaxial rupture stress
σ_a	Stress amplitude
σ_m	Hydrostatic stress or Mean stress
σ_y	Yield stress
σ_θ	Thermal load
$\Delta\bar{\varepsilon}_{Total}$	Effective total strain range
$\Delta\bar{\varepsilon}^c$	Effective creep strain increment
$\Delta\bar{\varepsilon}^e$	Effective elastic strain increment
$\Delta\varepsilon_e$	Elastic strain range

$\Delta\varepsilon_{ie}$	Inelastic strain range
$\Delta\varepsilon_p$	Plastic strain range
ΔG_{SEDE}	Activation energy range in Strain Energy Ductility Exhaustion method
$\Delta\theta_0$	Reference temperature/thermal load range
$\Delta\sigma_0^{pr}$	Cyclic reference mechanical load by pressure
$\Delta\sigma^{pr}$	Cyclic mechanical load by pressure
$\Delta\sigma_\theta$	Cyclic thermal load
$\Delta t, t$	Time period or Dwell time
$\Delta\varepsilon$	Total strain range
$\Delta\theta$	Temperature/thermal load range
$\Delta\theta(t)$	Cyclic thermal load over time period
A	Creep coefficient
D	Total creep-fatigue damage
E	Young's modulus
$J(\hat{\sigma})$	Invariant equivalent stress tensor
k, α	Material constants for power law equation of creep rupture time
LP	Limit pressure against the pipe bend parameter h for the 90° back-to-back pipe bends
m	Time exponent for creep power law
n	Stress exponent for Norton's creep law
p, q	Empirically derived constants for $\bar{\varepsilon}_f^c$
R	Saturated constant value for yield surface change in isotropic hardening
RT	Ratio of RP_{IP} to RP_{OP}
T	Temperature

U	Creep usage
V	Volume
X	Overall back stresses for kinematic hardening
Z	Elastic follow-up factor
γ	Shear strain
ε	Strain
θ	Temperature at the inside of the holed plate
$\theta(t)$	Temperature variation at the inside of the holed plate over time
ν	Poisson's ratio
σ	Stress

Acronyms

ASME NH	American Society of Mechanical Engineers Boiler and Pressure Vessel Code Section III Subsection NH
C.S.R	Creep Strain Recovery
CAE	Computer Aided Engineering
CEGB	Central Electricity Generating Board
DE	Ductility Exhaustion
DMMCs	Discontinuous Metal Matrix Composites
DRTMCs	Discontinuously Reinforced Titanium Matrix Composites
DSCA	Direct Steady Cycle Analysis
ECM	Elastic Compensation Method
EDF	Électricité de France
eDSCA	extended Direct Steady Cycle Analysis
EPP	Elastic Perfectly Plastic
FEA	Finite Element Analysis
JAEA	Japan Atomic Energy Agency
JRC	Joint Research Centre
LCF	Low Cycle Fatigue
LDS	Linear Damage Summation
LMMF	Linear Matching Method Framework
MDF	Multiaxial Ductility Factor
MECM	Modified Elastic Compensation Method
MMCs	Metal Matrix Composites
MUSM	Modified Universal Slope Method

PEEQ	Equivalent Plastic Strain
PEMAG	Plastic Strain Magnitude
PRTMCs	Particle Reinforced Titanium Matrix Composites
R5	Assessment procedure for the high temperature response of structure
RCC-MR _x	Design and Construction Rules for Mechanical Components in high-temperature structures, experimental reactors and fusion reactors
RVE	Representative Volume Element
SCRM	Structural Creep Recovery Mechanism
SEDE	Strain Energy Ductility Exhaustion
SiC	Silicon Carbide
SMDE	Stress Modified Ductility Exhaustion
TF	Time Fraction
TMCs	Titanium Matrix Composites
U.S	United States
UMAT	User subroutine to define a material's mechanical behaviour

This page intentionally left blank

1. Introduction

1.1 Research Background

According to the World Electricity Generation provided in DNV GL's Energy Transition Outlook, global energy demand is expected to exceed more than twofold in 2050, and three times by 2100. To meet such a huge demand, many renewable energy sources have been developed for generating electricity, and the role of the nuclear power plant is also becoming more important as a future energy source [1].

Raising the operating temperature to increase electricity production in the nuclear power industry is a practical solution in the aspect of efficiency and emissions reduction. It also reduces the cost of power production. In terms of enhancing efficiency, a next-generation nuclear reactor design which is called Generation IV reactor (Gen IV) is being developed through new research and development [2]. Gen IV design considers mainly two types of reactors which are thermal reactors with three systems and fast reactors with three system [3]. The thermal reactor includes a very high temperature reactor (VHTR), a supercritical water cooled reactor (SCWR), and a molten salt reactor (MSR). The fast reactor includes a gas-cooled fast reactor (GFR), a sodium-cooled fast reactor (SFR), and a lead-cooled fast reactor (LFR). Among Gen IV reactors, SFR type is expected to be commercialised first. SFR uses sodium as a coolant that has a melting point of 98 and a boiling point of 883 at atmospheric pressure, thus forming a liquid state in the operating temperature of 550. Unlike conventional light water reactor (LWR) the primary and intermediate loops where liquid sodium flows can be operated at atmospheric pressure. Consequently, the thickness of the reactor vessel and piping equipment can be a thin-walled design which can reduce capital expenditure and operating expense [4]. Moreover, the high temperature liquid sodium increases the thermal efficiency considerably.

However, regarding structural integrity, such high temperature has a significant impact on the life of nuclear power plant components [5]. At high temperatures, failure mechanisms can include creep, fatigue, creep-fatigue, and thermal fatigue [6]. Creep causes damages which can take place in several forms. For example, pure creep induces dimensional changes that cause distortions and wall thinning to steam turbine casing and piping systems. Localised creep deformation can cause swelling and leaks due to crack in headers and steam pipes. Long-term creep failure generally takes place from superheated reactor tubes and rotor serrations, which

involves cavitation and crack growth at interfaces and high stressed area. Figure 1.1-(a) shows creep induced crack in the fir-tree bottom serration.



Figure 1.1 (a) creep crack in the fir-tree bottom serration [7] and (b) creep-fatigue damage in the gas turbine blade[8].

Creep-fatigue failure induced by thermal stresses is also a significant problem in many high temperature components [9]. Literature has reported typical failure cases that occur in the power plant industry due to the creep-fatigue interaction [10]. The damage can be either creep dominated or fatigue dominated depending on the stress type that drives structural response within the loading cycle. In general, creep-fatigue damage that occurs in power plant is caused by thermal stresses which are generated by restriction of thermal expansions. Since crack initiation occurs in less than 1000 cycles due to thermally induced stresses, this sort of creep-fatigue damage is also referred to as thermo-mechanical fatigue and low cycle fatigue. Furthermore, rotor grooves and header boreholes are components that may have potential failures due to considerable plastic strain caused by this creep-fatigue failure. Figure 1.1-(b) shows creep-fatigue damage in gas turbine rotor blades. These complex high temperature failure mechanisms make the relationship between the actual stresses and strain occurring in the structure more complicated, making it difficult to predict the service life. Hence, due to the trend of increasing high temperature operating conditions, it is imperative to evaluate the accurate structural integrity of the reactors.

Many efforts had been made to develop standardised methods for high temperature integrity assessment. The American Society of Mechanical Engineers Boiler and Pressure Vessel Code Section III subsection NH (ASME NH) [11] and the R5 Procedures for Assessing the High Temperature Response of Structure (R5) [12] are results of the efforts. They are frequently used to assess the component's lifetime when put in high temperature conditions. However,

these code and procedure are validated for a limited number of materials and predict lifetime based on the simplified approach such as the rule-based method, resulting in conservative service life calculation. The ruled based methods do not provide detailed evaluation procedures for the complex inelastic response of the high temperature structures. Furthermore, they have other limitations in predicting the structural integrity; they cannot consider the environmental effects such as oxidation film breakage and impurities in helium, and cannot be applied to other materials of which damage accumulated do not follow the linear damage summation rule. It also requires the development of a guideline for materials that do not follow typical creep curves. Therefore, more effort is required in this research field to predict the service life of high temperature components more accurately.

As part of such efforts, the Linear Matching Method Framework (LMM Framework) has been developed as an alternative method [13, 14] and used for various engineering problems [15-17]. The LMM Framework consists of Linear Matching Method (LMM), Direct Steady Cycle Analysis (DSCA), and extended Direct Steady Cycle Analysis (eDSCA). The design code and procedure as mentioned earlier provide minimum design requirements that allow the user to evaluate whether structures are showing a strict shakedown response or whether they have significant effects of creep, but the results are overly conservative. The LMM is capable of calculating limit load and strict shakedown boundaries, even ratchet and creep rupture boundaries with DSCA. Moreover, eDSCA[18] can evaluate the accurate behaviours of the inelastic creep and plasticity much faster than conventional non-linear Finite Element Analysis (FEA). This alternative method can be utilised to optimise high temperature structure design, and to validate the structural response assessed by the rule-based method. Based on the reliability of the LMM Framework, R5 has acknowledged it as one of the structural response evaluation methods. Therefore, it is also vital to develop other Direct Methods or to extend the current Direct Method, for solving many other engineering problems that occur at high temperature. In this thesis, structural responses of engineering problems will be analysed utilising the LMM Framework, and the conventional full incremental cyclic analysis method will validate the obtained results.

1.2 Objectives of the thesis

The rule-based method may predict conservative load levels or short service life of the structure at elevated temperature. In other words, under the name of securing safety, the

running cost may be increased, as structures have premature retirement. Furthermore, if the structure shows a significant inelastic response that requires a detailed inelastic analysis with the conventional FEA, it may expend much computational resource to evaluate the structural response or may have convergence problems. Under the circumstance, demands for the alternating approaches are arising from power industries such as EDF Energy, Rolls Royce, and Siemens, and these industries U.K. based have shown interests in the LMM Framework [19-21].

The following three objectives have been defined to meet these demands from the industries, by solving engineering problems that will be presented in from chapters 4 to chapter 7:

- 1) Investigating cyclic plasticity and creep-cyclic plasticity behaviours of both an engineering structure in macroscopic scale and a futuristic material in the microscopic scale, which have not been studied in the past.
- 2) Many high temperature components equipped with the forced cooling system are running in service under non-isothermal condition. The present LMM eDSCA method has been widely used for predicting creep-cyclic plasticity behaviour of many engineering problems but has some limitations, which are not capable of considering effects of non-isothermal creep parameters and multiple dwell periods.
- 3) Through performing advanced numerical investigations, a new high temperature failure mechanism is identified, which is named as Structural Creep Recovery Mechanism (SCRM). This thesis will investigate the effects of the SCRM on the structural integrity assessment.

1.3 Outline of the thesis

This thesis is structured as follows:

Chapter 2 provides essential theoretical backgrounds for cyclic plasticity and creep-cyclic plasticity and existent methods to structural integrity assessment involving creep-fatigue interaction. Crack initiation assessment procedures of the design procedure and code, R5 and ASME NH, are briefly summarised in step by step order.

Chapter 3 describes detailed numerical procedures of the LMM Framework for shakedown analysis, Direct Steady Cycle Analysis (DSCA), extended Direct Steady Cycle Analysis (eDSCA), and the modified eDSCA which considers effects of non-isothermal load and multiple dwell condition.

Chapter 4 presents cyclic plasticity behaviour of a 90° back-to-back pipe bends structure subjected to cyclic thermo-mechanical loading (cyclic thermal load, cyclic in-plane bending, cyclic out-of-plane bending, and constant internal pressures) employing the LMM.

Chapter 5 investigates creep-cyclic plasticity behaviours of Metal Matrix Composites (MMCs) material subjected to cyclic thermal load and constant mechanical load through the LMM eDSCA. Titanium matrix reinforced with silicon carbide (SiC) particles (PRTMCs) has been selected for this investigation due to a high potential to exploit in the aerospace industry.

Chapter 6 investigates creep-cyclic plasticity behaviour of a superheater outlet tube plate under thermo-mechanical loading condition and evaluates creep-fatigue damage endurance, using the modified LMM eDSCA. Temperature-dependent material properties are employed to calculate more practicable structural behaviour and lifetime prediction.

Chapter 7 introduces the newly identified failure mechanism at high temperature utilising full incremental cyclic analysis. Utilising combined hardening model and temperature dependent material parameters, it proves that the failure mechanism can occur in practical operating condition.

Chapter 8 concludes researches of the thesis and offers recommendations for further works.

1.4 Engineering Units

All data presented in this thesis follows the International System of Units (SI system). Length in mm, stress in Mega Pascal (MPa), and absolute strain value are adopted. Some strain values are shown in symbols which have the relevant symbols.

2. High Temperature Component Design and Design Assessment Codes

2.1 Introduction

This chapter provides essential theoretical backgrounds for understanding high temperature structural behaviour under cyclic loading condition. Features of cyclic plasticity response such as shakedown, alternating plasticity, and ratchetting are described. Effects of creep behaviour on cyclic plasticity such as cyclically enhanced creep and creep enhanced plasticity are examined. This chapter also offers comprehensive reviews of creep-fatigue damage assessment procedures and design code which are R5 and ASME NH. Reviewing scope of both the procedure and the design code is focused on crack initiation assessment which is in line with the research scope of this thesis.

2.2 Structural Responses under Cyclic Load at High Temperature

2.2.1 *Cyclic Plasticity*

Under monotonic loading condition, a load level where a structure can withstand before plastic collapse is known as a limit load. For cyclic loading condition, a structure is likely to fail at a lower level than the limit load. Because accumulated residual stress and plastic strain affect structural responses of following cycles, particularly non-symmetry structures subjected to complex cyclic loadings may experience incremental plastic collapse at a far lower level than the limit load. The structure under cyclic load exhibits the following structural responses: elastic response, elastic shakedown (strict shakedown), plastic shakedown (global shakedown), and ratchetting. The structural responses can be shown by Bree diagram in Figure 2.1.

When a structure has a cyclic load level under elastic response region, no plastic deformation will develop. If the cyclic load level exceeds the elastic response limit, plastic strains begin to develop, and it will lead to following structural responses:

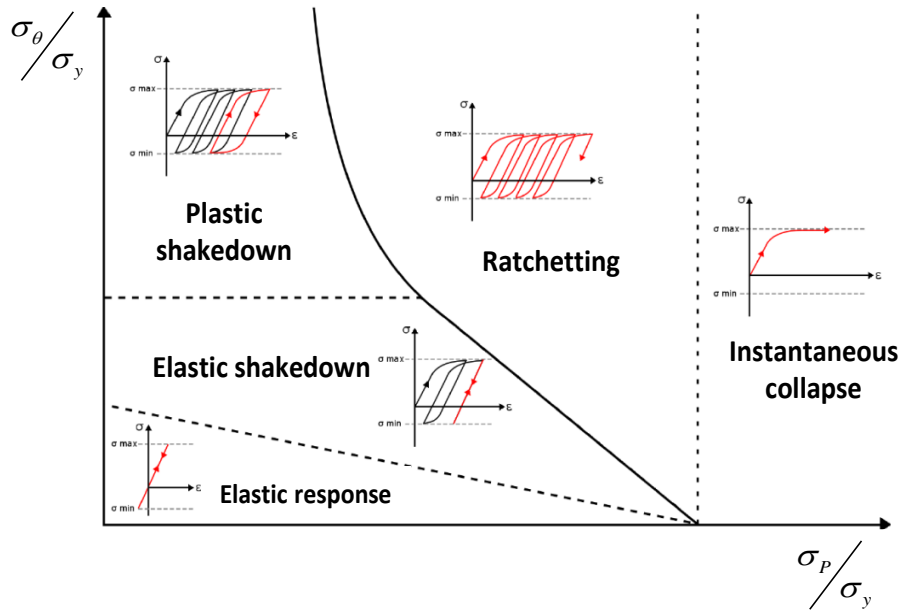


Figure 2.1 Structural response subjected to cyclic loading condition.

- Elastic shakedown: plastic strains develop within the first loading cycles due to yielding, but the following cycle remains inelastic response.
- Plastic shakedown: a fixed range of plastic strains develop over the entire loading cycle, but no increments in total strain accumulations.
- Ratchetting: plastic strains develop with every loading cycle, leading to an incremental plastic collapse.

2.2.1.1 Elastic Shakedown

The shakedown static and kinematic theorems were introduced for elastic-perfectly plastic material. Among these theorems, Melan[22] and Koiter's[23] theorems are widely used for constructing the elastic shakedown region which solves many engineering problems.

Melan's theorem is defined as "For a given cyclic load set the structure will shakedown if a constant self-equilibrating residual stress field can be found such that the yield condition is not violated for any combination of cyclic elastic and residual stresses". Melan's theorem is known as the lower bound shakedown theorem due to the calculated limit value is equal to or less than the actual elastic shakedown limit.

Koiter's theorem is defined as "For a prescribed load set $P(t)$ with a cyclic period t , if any kinematically admissible strain rate can be found during a time interval $(0, t)$ such that the

strain field is compatible with a displacement field u (which satisfies the applied displacement boundary conditions) and $\int_0^t \sum P \dot{u} \geq \int_0^t \int_V \dot{D} dV dt$, where \dot{D} is the rate of plastic dissipation per unit volume corresponding to the admissible strain rate $\dot{\epsilon}$, then elastic shakedown has not occurred". Koiter's theorem is known as the upper bound shakedown theorem of which the calculated value is equal to or greater than the actual elastic shakedown limit.

Melan's theorem provides conservative results, thus popularly being selected for the development of numerical technique as discussed in Section 3.1. However, it is worth mentioning that when the elastic shakedown limit of complex geometry is calculated by Finite Element Method, Melan's theorem might predict very conservative elastic shakedown limit for finite element model that has local stress concentrations which result in abnormally large stress magnitude. Koiter's theorem predicts the elastic shakedown limit based on the energy balance of internal and external work done. Thus it is known, generally, providing more accurate results than Melan's theorem. However, the predicted limit is un-conservative to the actual limit. Therefore, the predicted elastic shakedown limit needs to be taken from the least value between the upper and lower bound limits.

2.2.1.2 Plastic Shakedown

Cyclic load located in the plastic shakedown region does not cause the incremental plastic collapse of a structure but a fixed range of plastic deformation which may affect the lifetime of the structure by Low Cycle Fatigue (LCF). To evaluate the LCF damage, generally, total strain range is measured from strain controlled experiment. The total strain range $\Delta \mathcal{E}$ can be expressed as the sum of the elastic strain range $\Delta \mathcal{E}_e$ and the plastic strain range $\Delta \mathcal{E}_p$. The high cycle fatigue can be expressed by the relationship between the stress amplitude σ_a and the number of cycles to failure N . The elastic strain range can be expressed as $\Delta \mathcal{E}_e = C_e N^b$, where C_e and b are material constants. In the case of low cycle fatigue, it can be expressed by the Manson-Coffin equation so that the plastic strain range can be defined as $\Delta \mathcal{E}_p = C_p N^c$, where C_p and c are material constants. With the equations above, the relationship between the total strain range and a number of cycle to fatigue failure N_f can be expressed as:

$$\Delta \mathcal{E} = \Delta \mathcal{E}_e + \Delta \mathcal{E}_p = C_e N_f^b + C_p N_f^c \quad (2.1)$$

Eq.(2.1) can be expressed for a number of reversals to failure $2N_f$ as

$$\frac{\Delta\varepsilon}{2} = \frac{\Delta\varepsilon_e}{2} + \frac{\Delta\varepsilon_p}{2} = \frac{\sigma_f'}{E}(2N_f)^b + \varepsilon_f'(2N_f)^c \quad (2.2)$$

where σ_f' and b are the fatigue strength coefficient and exponent respectively; ε_f' and c are the fatigue ductility coefficient and exponent respectively. The relationship between total strain range and a number of cycle to failure can be illustrated as $\varepsilon - N_f$ curve in Figure 2.2.

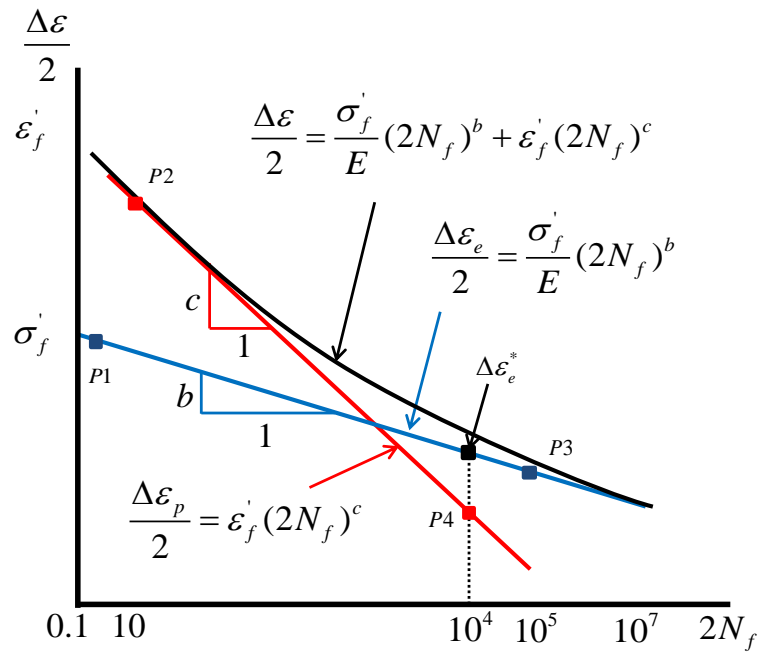


Figure 2.2 Low cycle fatigue $\frac{\Delta\varepsilon}{2} - 2N_f$ curve

The method of estimating the $\varepsilon - N$ curve is mostly based on the use of mechanical properties and the use of hardness. This section provides a brief introduction only to the method based on the use of mechanical properties which is popularly used in industries. The method using of the mechanical properties can be divided into a method using tensile strength σ_B and fatigue ductility ε_f and a method using only tensile strength σ_B .

A method using tensile strength σ_B and fatigue ductility ε_f

i) Original four-point correlation method by Manson

This classic method uses two points to construct each linear relationship between $\Delta\varepsilon_e$ and N_f and between $\Delta\varepsilon_p$ and N_f . Points P1 and P3 of $\Delta\varepsilon_e - N_f$ relationship are corresponding to $\left(N_f = 0.25, \Delta\varepsilon_e = 2.5 \frac{\sigma_f}{E}\right)$ and $\left(N_f = 10^5, \Delta\varepsilon_e = 0.9 \frac{\sigma_B}{E}\right)$. Points P2 and P4 of $\Delta\varepsilon_p - N_f$ relationship are corresponding to $\left(N_f = 10, \Delta\varepsilon_p = \frac{1}{4} \varepsilon_f^{\frac{3}{4}}\right)$ and $\left(N_f = 10^4, \Delta\varepsilon_p = \frac{0.0132 - \Delta\varepsilon_e^*}{1.91}\right)$. Those four points from P1 to P4 are utilised to express the $\Delta\varepsilon - N_f$ relationship which is the same as Eq.(2.1), but it is known that the agreement with the actual test results is not very good.

ii) Original universal slopes method by Manson [24]

This method uses the following equation to present $\Delta\varepsilon - N_f$ the relationship of all metallic materials:

$$\Delta\varepsilon = \Delta\varepsilon_e + \Delta\varepsilon_p = 3.5 \frac{\sigma_B}{E} N_f^{-0.12} + \varepsilon_f^{0.6} N_f^{-0.6} \quad (2.3)$$

Eq.(2.3) is very convenient and easy to use, but it tends to predict shorter fatigue life than the actual lifespan about long lifespan.

iii) *Modified universal slopes method by Muralidharan and Manson [25]*

This is the modified method of Eq.(2.3) and expressed as:

$$\Delta\varepsilon = 1.17 \left(\frac{\sigma_B}{E} \right)^{0.832} N_f^{-0.09} + 0.0266 \varepsilon_f^{0.155} \left(\frac{\sigma_B}{E} \right)^{-0.53} N_f^{-0.56} \quad (2.4)$$

Eq.(2.4) is known as the best fit to steel material [26]. Therefore, it will be employed to calculate fatigue damage life in Chapter 6.

iv) *Modified four-point correlation method by Ong [27]*

This is the modified method of the original four-point correlation method by Manson,

which points P1 and P3 are corresponding to $\left(N_f = 10^0, \Delta\varepsilon_e = \frac{\sigma_f}{E} \right)$ and

$\left(N_f = 10^6, \Delta\varepsilon_e = 0.16 \left(\frac{\sigma_B}{E} \right)^{0.81} \right)$ and points P2 and P4 are corresponding to

$\left(N_f = 10^0, \Delta\varepsilon_p = \varepsilon_f \right)$ and $\left(N_f = 10^4, \Delta\varepsilon_p = \frac{0.00737 - \frac{\Delta\varepsilon_e^*}{2}}{2.074} \right)$. The results predicted are

better than the original method but it is not so good.

v) *Mitchell's method [28]*

This method is the designed method particularly for steel materials, and the $\Delta\varepsilon - N_f$ relationship is expressed as:

$$\frac{\Delta\varepsilon}{2} = \frac{(\sigma_B + 345)}{E} (2N_f)^{\frac{1}{6} \log \left\{ \frac{2(\sigma_B + 345)}{\sigma_B} \right\}} + \ln \left(\frac{100}{100 - RA} \right) (2N_f)^c \quad (2.5)$$

where RA is the reduction of area; c can be obtained from a relationship between transition fatigue life and hardness.

vi) *Modified Mitchell's method by Park and Song [29]*

This is the modified method of Eq.(2.5) and designed mainly for predicting the fatigue life of aluminium alloy and titanium alloy.

$$\frac{\Delta\varepsilon}{2} = \frac{(\sigma_B + 335)}{E} (2N_f)^{\frac{1}{6} \log \left\{ \frac{2(\sigma_B + 335)}{0.446\sigma_B} \right\}} + \ln \left(\frac{100}{100 - RA} \right) (2N_f)^{-0.664} \quad (2.6)$$

Eq.(2.6) shows the best agreement with experimental results of titanium alloy.

A method using only tensile strength σ_B

i) *Uniform material law by Bäumel and Seeger [30]*

This is the method only using tensile strength of individual metallic material and provides two equations as:

$$\frac{\Delta\varepsilon}{2} = 1.5 \frac{\sigma_B}{E} (2N_f)^{-0.087} + 0.59\psi (2N_f)^{-0.58} \quad (2.7a)$$

$$\frac{\Delta\varepsilon}{2} = 1.67 \frac{\sigma_B}{E} (2N_f)^{-0.095} + 0.35\psi (2N_f)^{-0.69} \quad (2.7b)$$

where $\frac{\sigma_B}{E} \leq 0.003$, $\psi = 1$; $\frac{\sigma_B}{E} > 0.003$, $\psi = 1.375 - 125 \frac{\sigma_B}{E}$. Eq.(2.7a) is used for unalloyed steel and low-alloy steel. Eq.(2.7b) is used for aluminium alloy and titanium alloy.

ii) *Medians method by Maggiolaro and Castro* [31]

Maggiolaro and Castro introduced a method using the median value from each parameter of $\frac{\Delta\varepsilon}{2} - 2N_f$ the curve concerning 845 types of materials. This method also only requires tensile strength.

$$\frac{\Delta\varepsilon}{2} = 1.5 \frac{\sigma_B}{E} (2N_f)^{-0.09} + 0.45(2N_f)^{-0.59} \quad (2.8)$$

$$\frac{\Delta\varepsilon}{2} = 1.9 \frac{\sigma_B}{E} (2N_f)^{-0.11} + 0.28(2N_f)^{-0.66} \quad (2.9)$$

Eq.(2.8) and Eq.(2.9) have good predictions for steel material and aluminium alloy respectively. It is noteworthy that Eq.(2.9) shows the best results for aluminium alloy compared to other methods.

2.2.1.3 Ratchetting

If cyclic load level increased to a point within the ratchetting zone, plastic strain develops incrementally with every cycle. Eventually, the structure may collapse before reach the designed service cycle. Ratchetting is a complex structural behaviour and usually associated with a load cycle that has a non-zero mean stress level, mainly affected by mechanical load but sometimes by varying thermal load. Ratchetting response is the failure mechanism which can coincide in several places of a structure, unlike to elastic shakedown response which is considered as a localised mechanism. Therefore, the cyclic load level for operation should not be located in the ratchetting zone unless designed service life is extremely very short such as a designed operation cycle less than 20 cycles. The assessment procedure and the design codes such as R5[12], ASME NH[11], and RCC-MRx [32] allow the maximum load level to the extent that it causes an elastic shakedown structural response, but if plastic shakedown occurs, a low cycle fatigue damage assessment shall be performed.

2.2.2 Creep-Cyclic Plasticity

As described above in Section 2.2.1, structural behaviour under cyclic loading is much more complicated than that shown under monotonic loading. If the advanced hardening model such as the combined isotropic and kinematic models is considered, cyclic plasticity of a structure is more difficult to understand. To make matters worse, if the structure under cyclic loading is subjected to high temperature, the strength of materials is not only degraded but also effects of visco-plasticity due to creep shall be considered. In this case, the total strain range of a structure can be expressed as:

$$\Delta\varepsilon = \Delta\varepsilon_e + \Delta\varepsilon_p + \Delta\varepsilon_{ie} \quad (2.10)$$

where $\Delta\varepsilon_{ie}$ is the inelastic strain increment due to creep.

Creep is a time-dependent inelastic response that occurs when a material is loaded at high temperature, and the temperature has a significant effect on deformation [33]. The creep deformation is caused by microstructural defect rearrangement of which process is accelerated at high temperature. Generally, mathematical modelling of creep deformation is performed as shown in the creep test of Figure 2.3. The obtained creep curve is described in three parts: the primary creep is a part of decreasing creep strain rate; the secondary creep is a part of constant creep strain rate; the tertiary creep is a part of increasing creep strain rate which leads to fracture.

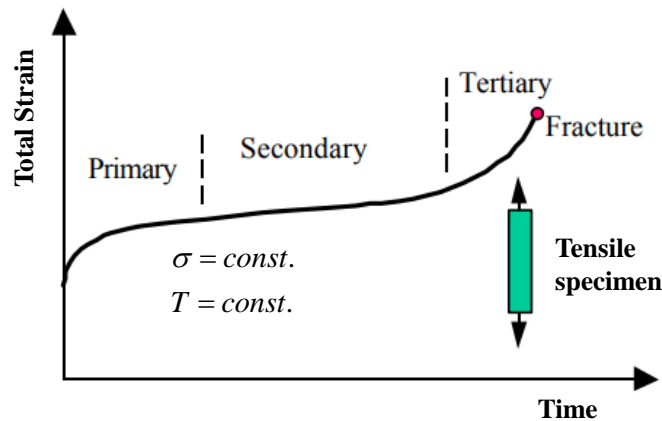


Figure 2.3 Basic creep curve for constant stress and temperature.

There are various mathematical creep models because the creep deformation state is different according to the type of material and stress state. However, this thesis will restrict the application of creep stage to primary and secondary creep utilising the time hardening power

law which is very common in creep analysis. Detailed creep constitutive models or various creep mechanisms associated with the creep process will not be described either in this section. Meng and Wang introduced a comprehensive review of the related equations and various creep mechanisms [34].

Under cyclic loading, creep may enhance fatigue damage process of high temperature structure. The typical failure mechanisms associated with the synergistic creep-fatigue interaction are crack initiations due to “low cycle fatigue” (LCF) and “creep ratchetting”. LCF induces a finite lifetime of components due to high-stress levels and a low number of cycles to failure. Common factors that have been attributed to creep ratchetting are “cyclic enhanced creep” and “creep enhanced plasticity” [12, 18]. On the one hand, creep deformation is generally enhanced by cyclic loading, especially for a more extended dwell period. Stress-strain interaction often reports non-closed hysteresis loop due to the enhancement in creep strains, where it is referred to cyclic enhanced creep. On the other hand, if significant stress relaxation occurs within small creep deformation, it can also lead to the creep ratchetting due to considerable unloading plasticity, where it is referred to the creep enhanced plasticity. If an applied cyclic loading level is under either strict or global shakedown limit without creep, no ratchetting mechanism appears in the steady state response [35]. However, with creep, for the same loading level applied, the ratchetting response can take place due to either cyclically enhanced creep or creep enhanced plasticity depending on primary load level, known as rupture reference stress, or duration of dwell period [36-38].

Barbera *et al.* presented different creep-cyclic plasticity graphically in Figure 2.4 [39]. Figure 2.4(a) and (b) show no incremental plastic strain in the absence of creep, but the inelastic strain increases at every cycle due to the effect of creep, resulting in ratchetting. In this case, the ratchetting is called creep ratchetting enhanced by cyclic creep effects. Figure 2.4(c) and (d) also show the creep ratchetting mechanism. Figure 2.4(c) is called creep enhanced plasticity that causes ratchetting with unloading plasticity due to significant creep stress relaxation. In the case of Figure 2.4(d), the structure without creep effect has only a fixed range of plastic deformation, but it causes severe creep ratchetting due to cyclically enhanced creep.

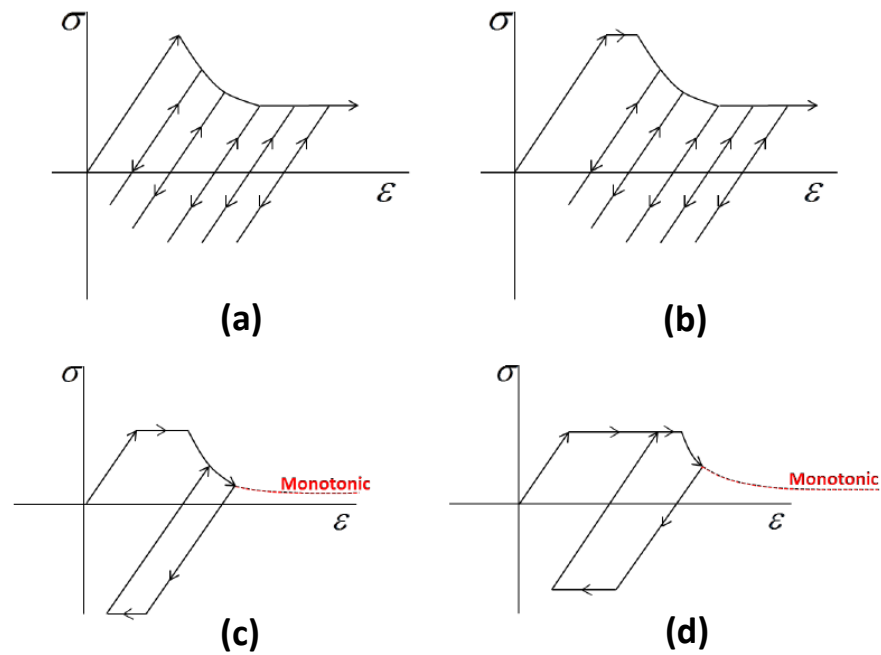


Figure 2.4 Different creep-cyclic plasticity responses at tensile creep peak [39]: (a) elastic response, (b) elastic shakedown, (c) creep enhanced plasticity, and (d) creep enhanced plastic shakedown[39].

It is noteworthy that if tensile creep ratchetting occurs at tensile creep peak, the induced creep ratchetting can be judged as a phenomenon caused by cyclically enhanced creep. However, if compressive creep ratchetting occurs at tensile creep peak, the primary mechanism that induces the creep ratchetting is the creep enhanced plasticity.

For ensuring the structural integrity, R5 procedure also recommends to evaluate lifetime of a high temperature component against following failure mechanisms: plastic collapse failure, creep rupture failure, ratchetting collapse, crack initiation due to creep-fatigue interaction, and excessive cyclic enhanced creep deformation [12]. In order to satisfy the design requirements, cyclic plastic analysis and cyclic creep and plastic analysis have to be carried out independently.

2.2.3 Creep-Fatigue Damage Evaluations

Although creep ratchetting could occur in early load cycles, the creep ratchetting mechanism may or may not be found in the steady cyclic state due to the complex interaction of creep and cyclic plasticity. Whether or not creep ratchetting occurs, the structural integrity being deteriorated can be seen due to the augmented total strain range caused by the inelastic strain

increment in Figure 2.4. For ensuring structural integrity, it is necessary to evaluate the total damage caused by creep and fatigue interaction. Generally, the high temperature design codes evaluate total damage in the following way:

$$D_c + D_f \leq \Phi_{CF} \quad (2.11)$$

where D_c and D_f are the total creep damage and total fatigue damage; Φ_{CF} is the allowable total creep-fatigue damage factor which is depending on the type of material. This creep-fatigue damage relationship can be depicted as Figure 2.5 that shows the creep-fatigue damage envelopes. If the total damage factor Φ_{CF} is equal to unity the total damage envelope can be expressed with a linear line. However, if allowable creep and fatigue damage is equal to 0.3 or other factors, the damage envelope can be created with an intersection point reflecting each damage factor.

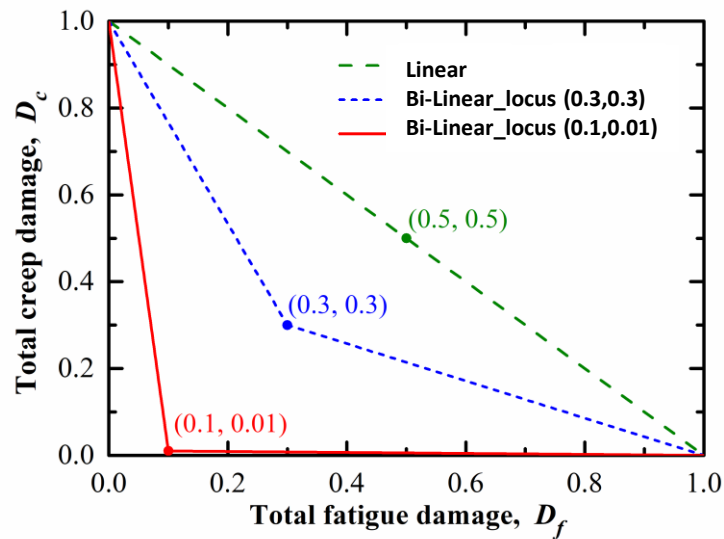


Figure 2.5 The creep-fatigue damage envelope.

To evaluate the total creep-fatigue damage, ASME BPVC and RCC-MRx codes use the procedure of creep-fatigue damage evaluation as shown in Figure 2.6. According to the procedure, creep damage and fatigue damage are separately evaluated based on generally elastic analysis solutions with various coefficients which take into account inelastic behaviours. However, the total damage calculated based on the procedure is predicting a generally conservative lifetime. It is worth to know that for creep damage evaluation the design codes ASME NH and RCC-MRx use Time Fraction approach (TF), and R5 use Ductility Exhaustion

method (DE). Spindler introduced a modified DE method (SMDE) that reduce the over-conservatism of DE model by reflecting the stress effect on DE model [40]. Takahashi *et al.* developed energy based ductility exhaustion model (SEDE) and showed its predictability through systematic evaluation of creep-fatigue life with several materials which are popularly used in the nuclear industry[41]. In chapter 6, creep damage life will be evaluated with TF, DE, and SEDE models and some discussions for the results will be made.

The fatigue damage can be calculated from the equations shown in Section 2.2.1.2 using total strain range. In the case of the design codes, ASME NH, provides $\varepsilon - N_f$ curve for several materials: 304SS, 316SS, Alloy 800H, 2.25Cr-1Mo Steel.

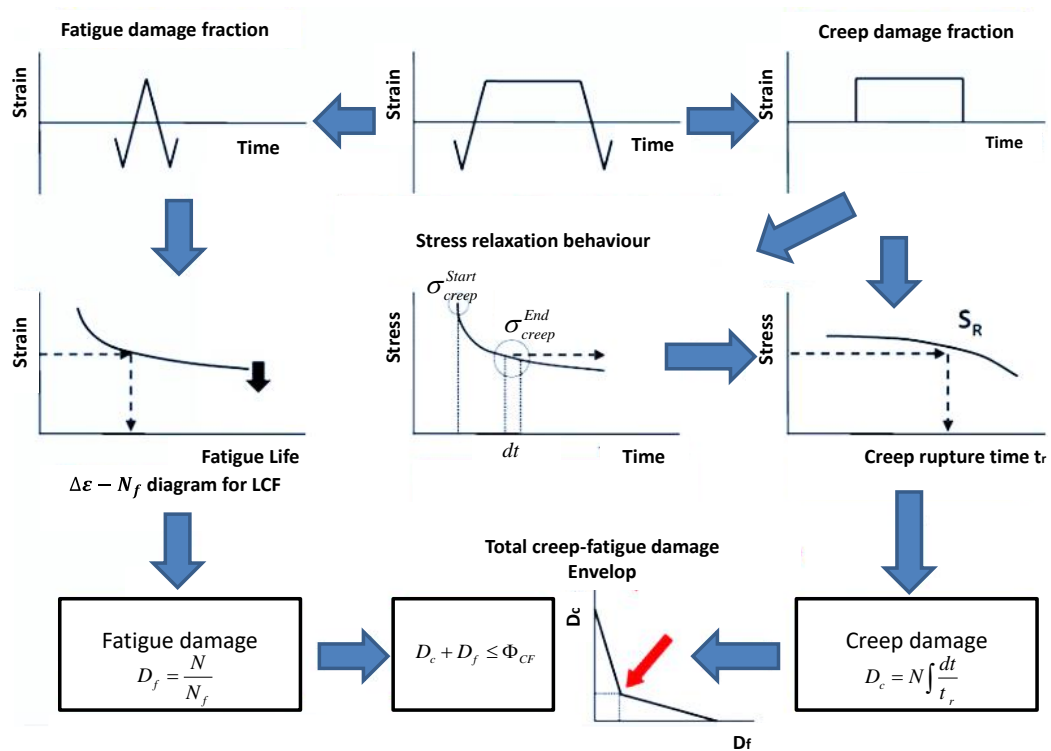


Figure 2.6 Procedures of creep-fatigue damage evaluation.

Apart from the separated damage assessment methods, there are simplified creep-fatigue damage assessment models that predict a number of cycles to creep-fatigue failure. For stainless steel 316, Liu *et al.* introduced a unified creep-fatigue equation that predicts fatigue damage considering the effect of inelastic strain [42]. The unified equation can be expressed in a strain form: $\varepsilon_p = C_0 c(T, t, \varepsilon_p) N^{-\beta_0}$ and a power law form: $\varepsilon_p = C_0 c(T, t, \varepsilon_p) N^{-\beta_0 b(T, t)}$. According to the authors, the unified model has been verified on stainless steel 316. Thus the

unified equation in the power law form will be used to calculate creep-fatigue damage in Chapter 6. For example, in the case of P91 steel, following two simplified models [43, 44] have been introduced to calculate the creep-fatigue life cycles:

$$N_{C-F}(t_h) = \frac{N_{f0}}{1 + \frac{k^{cf}}{\frac{A^{MH}}{t_h} (N_{f0})^{\frac{m^c+b}{m^c}}}} \quad (2.12a)$$

$$\Phi_{C-F}(\Delta\varepsilon, t_h, T) = A_1 + \frac{A_2}{\Delta\varepsilon} + A_3 \cdot \log(t_h) + A_4 \cdot T \quad (2.12b)$$

where parameters A^{MH} and m^c are derived from creep rupture models; k^{cf} is the curve fitting parameter; b is the elastic exponent of the Manson-Coffin equation shown in Eq.(2.2); A_1 , A_2 , A_3 , and A_4 are parameters to optimise creep-fatigue data obtained from experiments. Eq.(2.12a) is the Manson-Halford creep-fatigue life cycle prediction model, and Eq.(2.12b) is the Φ model using the Wilsher equation [45]. Japan Atomic Energy Agency (JAEA) data reported that these simplified models successfully predict the Joint Research Centre (JRC) creep-fatigue test data for specific temperature range [46]. However, it has been reported that the evaluated results of the damage envelop based on the simplified models are derived from the test conditions using relatively large strain range and short hold time. Thus the creep damage evaluated is more significant than actual creep damage [47]. Usually, high temperature structures are run for several months as short-term or a couple of years as long-term during one operation, so creep testing under long hold time condition is required for proper creep damage evaluation, and this should be used to improve understanding of long-term microstructural evolution.

So far, the structural responses and the integrity assessment methods of high temperature components subjected to cyclic loading have been briefly described. The next section will briefly describe two design codes, R5 and ASME NH that are widely used for the high temperature integrity assessment.

2.3 Design Codes and procedures for Assessing Structural Integrity under High Temperature

2.3.1. R5 Assessment Procedure for the High Temperature Response of Structure

Over 30 years ago the life assessment procedures of high temperature components were developed within the UK Central Electricity Generating Board (CEGB). It enabled to assess structural integrity at high temperature, but the old procedures did not handle some details such as weldments and defect tolerance. Therefore, further development of the procedure was carried out within the CEGB, and then the R5 high temperature assessment procedure was out by British Energy (now EDF Energy) and mainly used in the UK nuclear power industry.

Structure operating under high temperature may have life limitation due to following failure mechanisms: instantaneous plastic collapse, creep rupture, ratchetting, enhanced creep deformation and crack initiation and crack propagation due to creep-fatigue interaction. R5 is the lifetime assessment procedure that provides step-by-step instructions covering mechanisms above. R5 consists of following five volumes:

Volume 1: Overview

Volume 2/3: Creep-fatigue initiation procedure for defect-free structures

Volume 4/5: Procedures for assessing defects under creep and creep-fatigue loading

Volume 6: Assessment procedure for dissimilar metal welds

Volume 7: Behaviour of similar welds: guidance for steady creep loading of CrMoV pipework components

Among those five volumes, this section mainly describes a procedure of volume 2/3 of which aim is to evaluate the steady cyclic state by a simplified technique for defect-free structures subjected to cyclic loading involving creep effects. The volume 2/3 provides step-by-step procedures that estimate the number of cycles to create a crack of a defined size. Then the number of cycles obtained is used to estimate the total damage of a structure under creep-fatigue loading.

The step-by-step procedure consists of a series of eighteen steps in total, but the last two steps are not considered in this review due to having little to do with creep-fatigue damage assessment. Brief introductions to each step are made as follows.

Step 1. Resolve load history into cycle types

Step 1 is a simplification process of a real operational load history so that the reduced number of different loading cycles is used for the crack initiation assessment. A similar process has also been adopted by other codes, such as RCC-MRx and ASME.

Step 2. Perform elastic stress analysis

Elastic stress analysis is performed to define critical zones in a structure investigated where show maximum stress levels, stress range, maximum temperature levels. For the elastic stress analysis, finite element methods are commonly used, and it calculates equivalent elastic stress and strain, and equivalent elastic stress and strain ranges.

Step 3. Demonstrate sufficient margins against plastic collapse

In R5 it is ensured that a structure does not have the instantaneous collapse under the first loading before the steady cyclic state is reached. To define the load level that causes the plastic collapse is the limit load analysis. There are various ways to perform the limit load analysis but R5 acknowledges the modified elastic method. The Linear Matching Method, which is mainly used for studies in this thesis, is one of the numerical methods acknowledged by R5.

Step 4. Determine whether creep is significant

If the following equation is satisfied R5 suggest the effects of creep may be neglected, where NC_i is the total number of cycle of each cycle type i ; t and t_m are the dwell time and the maximum time respectively at the reference temperature T .

$$\sum_i NC_i [t/t_m(T)]_i < 1.0 \quad (2.13)$$

R5 also provides curves of t_m against temperatures for ferritic and austenitic steels.

Step 5. Demonstrate that creep rupture endurance is satisfactory

A rupture reference stress σ_{ref}^R is used for creep rupture assessment in R5. The rupture reference stress is calculated using primary load reference stress σ_{ref} :

$$\sigma_{ref} = P_{prime} \sigma_y / P_{Limit} \quad (2.14)$$

where P_{prime} is the prime load level; σ_y is the yield stress; P_{Limit} is the limit load at plastic collapse. For creep ductile material the rupture stress can be calculated from Eq.(2.15), but other materials are calculated from Eq. (2.16), where χ is the stress concentration factor which is calculated from $\chi = \bar{\sigma}_{el,max} / \sigma_{ref}$ where $\bar{\sigma}_{el,max}$ is the maximum equivalent elastic stress and when $\chi \leq 4.0$, the evaluation is acceptable; n is the stress exponents for Norton's creep law.

$$\sigma_{ref}^R = [1 + 0.13(\chi - 1)] \sigma_{ref} \quad (2.15)$$

$$\sigma_{ref}^R = [1 + (1/n) \cdot (\chi - 1)] \sigma_{ref} \quad (2.16)$$

The creep usage U can be expressed as a summation of the total number of cycles of each cycle type is less than 1.0, where t_f is the allowable time from the creep rupture curve.

$$U = \sum_i NC_i \left[\frac{t}{t_f(\sigma_{ref}^R, T)} \right]_i < 1.0 \quad (2.17)$$

Step 6. Perform simple test for shakedown and check for insignificant cyclic loading

This step is to ensure if the structure experience ratchetting which causes incremental plastic failure. If the structure is subjected to insignificant cyclic loading, then Steps from 7 to 14 can be exempted and directly go to step 15. Otherwise, a following simple test for shakedown, which is called as stress linearization method, needs to be performed.

$$\bar{\sigma}_{el,lin}(x, t) \leq K_s S_y \quad (2.18)$$

$\bar{\sigma}_{el,lin}(x,t)$ is the equivalent elastic stress at the point x of over the structure within the overall period t ; K_s is the parameters provided by R5; S_y is the 0.2% proof stress of the material. If an additional condition Eq.(2.18) is satisfied, where r_{pi} and r_{po} are the extent of the length of the stress classification line at inner and outer surfaces respectively; w is the section thickness, then Step 7 can be exempted as applying r_{pi} or r_{po} to the cyclic plastic zone size r_p . As an alternative way, the shakedown limit can be computed simply by the LMM.

$$r_{pi} + r_{po} \leq 0.2w \quad (2.19)$$

To determine the insignificant cyclic loading following criteria needs to be fulfilled: a) the most severe cycle is within the elastic range, b) the total fatigue damage is less than 0.05 and c) Creep behaviour is not affected by cyclic loading as satisfying $\Delta\bar{\sigma}_{el,max} \leq \sigma_{ss} + (K_s S_y)_{nc}$, where σ_{ss} is the steady-state creep stress; the subscript nc refers to value at non-creep end of the cycle.

Step 7. Perform global shakedown check and calculate cyclic plastic zone size

Global shakedown which is a structural response that causes a fixed range of plastic deformation over entire loading cycle without an incremental plastic strain should be ensured for a structure assessed in R5. Although a structure experiences the shakedown with constant residual stress, the structure may have additional residual stresses over the cyclic history with creep. Therefore if the creep is insignificant to a structure forming the global shakedown, the steady cyclic stresses $\hat{\sigma}_s(x,t)$ can be expressed by $\hat{\sigma}_s(x,t) = \hat{\sigma}_{el}(x,t) + \hat{\rho}(x)$, where $\hat{\sigma}_{el}(x,t)$ is the elastic stress solution; $\hat{\rho}(x)$ is the residual stress field. The $\hat{\sigma}_s(x,t)$ replaces the equivalent elastic stress history as the steady cyclic history of equivalent stress $\bar{\sigma}_s(x,t)$ which then needs to satisfy the shakedown criterion $\bar{\sigma}_s(x,t) \leq K_s S_y$. If global shakedown is not achieved then it may require detailed inelastic analysis to ensure the structural integrity over the designed life. As an alternative method, the global shakedown limit can be calculated by the LMM without considering creep effects.

Step 8. Calculate shakedown reference stress, reference temperature and the start of dwell stress

In this step, a shakedown reference stress and associated reference temperature are calculated to evaluate the overall creep deformation and the creep rupture life of a structure under cyclic loading. The $\bar{\sigma}_s(x,t)$ calculated in Step 7 is used to calculate modified the reference stress which is termed as the shakedown reference stress σ_{ref}^S for the corresponding temperature T_{ref}^S . If a structure is within the global shakedown the σ_{ref}^S and T_{ref}^S produce a conservative creep usage. If there is no residual stress accumulated after the first cycle, it can be seen the structure within the elastic shakedown, the start of dwell stress σ_s may converge to the primary load reference stress σ_{ref} at the steady cyclic state. Start of the dwell stress can be estimated from

$$\sigma_s = \Delta \bar{\sigma}_{el,max} - (K_s S_y)_{nc} \quad (2.20)$$

It is noteworthy that if the investigated point is within the global shakedown then σ_s may provide too large value. In the case, it is recommended to adopt a less pessimistic number provided in R5.

Step 9. Estimate elastic follow-up factor and associated stress drop during creep dwell

When high temperature structures are subjected to cyclic thermal loading, it can be seen the stress relaxation during a dwell period. This relaxation may cause extra residual stresses that affect following elastic-plastic behaviours. The stress drop can be expressed by elastic follow-up factor Z which can be defined as a ratio of effective creep strain increment $\Delta \bar{\epsilon}^c$ to equivalent elastic strain increment $\Delta \bar{\epsilon}^e$ over a designed dwell time.

$$Z = - \frac{\Delta \bar{\epsilon}^c}{\Delta \bar{\epsilon}^e} \quad (2.21)$$

R5 provides three options for evaluations of the elastic follow-up factor. The first option is to assume no stress relaxation taking place within a dwell, leading to $Z = \infty$. The second option is to assume $Z = 3$, provided that the high temperature structure is under the isothermal

condition and primary loads are smaller than secondary loads that satisfy a condition of $(P_L + P_B) < 0.2\sigma_s$, where P_L and P_B are the primary stresses, in everywhere of the structure. The last option is to calculate Z from an inelastic analysis using a simplified manner rather than full inelastic analysis. In this case, Z can be estimated from

$$Z = \left(\Delta \bar{\epsilon}_{total} + \Delta \sigma_{rD} / \bar{E} \right) / \left(\Delta \sigma_{rD} / \bar{E} \right) \quad (2.22)$$

where $\Delta \bar{\epsilon}_{total}$ is the total strain increment; $\Delta \sigma_{rD}$ is the stress drop from experiment test results; \bar{E} is the effective Young's modulus $\bar{E} = 3E/2(1+\nu)$. If $Z > 1$ then $\Delta \sigma_{rD}$ in Eq.(2.22) needs to be replaced by a consistent value of $\Delta \sigma'$ where is taken from cyclic relaxation data.

Step 10. Calculate the total strain range

For the total strain range calculation, it can follow the simplified methods described in previous sections if resultants are satisfied with the required criteria. Otherwise, the total strain range is computed by using the enhanced elastic stress range $\Delta \bar{\sigma}_{el,r} = \Delta \bar{\sigma}_{el} + \Delta \sigma_{rD}$. If a material behaviour follows cyclic stress-strain curve represented by a Ramberg-Osgood equation, the total strain range is calculated using the total stress range $\Delta \bar{\sigma}$ which is solved by Neuber's rule, where A^* and β are constants used for Ramberg-Osgood equation; $\Delta \bar{\epsilon}_{vol}$ is the increase in volume. Procedures to calculate $\Delta \bar{\epsilon}_{vol}$ can be referred to RCC-MR code.

$$\Delta \bar{\sigma}_{el,r} \Delta \bar{\epsilon}_{el,r} = (\Delta \bar{\sigma}_{el} + \Delta \sigma_{rD})^2 / \bar{E} = \Delta \bar{\sigma} \left[\Delta \bar{\sigma} / \bar{E} + (\Delta \bar{\sigma} / A^*)^{1/\beta} \right] \quad (2.23)$$

$$\Delta \bar{\epsilon}_{Total} = \left[\Delta \bar{\sigma} / \bar{E} + (\Delta \bar{\sigma} / A^*)^{1/\beta} \right] + \Delta \bar{\epsilon}_{vol} \quad (2.24)$$

Step 11. Check limits on cyclically enhanced creep and calculate creep usage factor

This step checks if a structure has no creep ratchetting due to accumulations of the creep deformation under cyclic loading by calculating the creep usage factor W .

$$W = \sum_i NC_i \left[\frac{t}{t_f(\sigma_{ref}^S, T_{ref}^S)} \right]_i < 1.0 \quad (2.25)$$

The shakedown reference stress σ_{ref}^S at the reference temperature T_{ref}^S is calculated from

$$\text{when } Y(1-X) < 1, \quad \sigma_{ref}^S = [Y - 2\sqrt{Y(1-X)+1}]S_y \quad (2.26)$$

$$\text{when } Y(1-X) \geq 1, \quad \sigma_{ref}^S = XYS_y \quad (2.27)$$

where $X = \sigma_{ref} / S_y$ and $Y = Q_{range} / S_y$, where Q_{range} is the maximum elastic thermal stress range.

Step 12. Summarise assessment parameters

This step summarises the parameters obtained from previous steps. The identified ones are like as follows and will be used for creep-fatigue damage calculations in following steps 14 and 15: r_p the cyclic plasticity zone; T_{ref}^S the shakedown reference temperature; σ_s the start of the dwell stress; Z the elastic follow-up factor; $\Delta\sigma'$ the dwell stress drop range; $\Delta\bar{\epsilon}_{Total}$ the total strain range; W the creep usage factor.

Step 13. Treatment of weldments

For treatment of weldments, the assessment methods are similar with those parent materials, but the following additional points are considered in the previous sections.

- Potential mismatch of materials properties.
- The introduction of welding defects.
- The presence of high local residual stress.
- The effect of surface finishes creating the difference between ‘dressed’ and ‘undressed’ welds.

Appendix A4 in R5 provides modification details to the procedure that describe relevant fatigue strength reduction factors and guidance for use.

Step 14. Calculate fatigue damage per cycle

Fatigue damage per cycle d_f is calculated from Eq. (2.28), where N_0 is the number of cycles to initiate a crack having a size of a_0 at the total strain range $\Delta\bar{\varepsilon}_{Total}$. R5 defines the nucleation of a defect size a_i of 0.02mm for fatigue damage accumulation.

$$d_f = 1/N_0 \quad (2.28)$$

Generally N_0 can be calculated from empirical equations derived in fatigue endurance data. R5 suggests the following three steps:

- Obtain the relevant fatigue endurance data.
- Partition the endurance data into curve describing the number of the cycle for nucleation N_i and growth N_g . $\ln(N_i) = \ln(N_f) - 8.06N_i^{-0.28}$ where N_f is the number of cycles to failure.
- Calculate the number of cycles $N'_g = M \cdot N_g$ to grow the crack from size a_i to a_0 , where the calculating procedure of M can be found in R5. The fatigue endurance for a_0 is calculated from $N_0 = N_i + N'_g$.

Step 15. Calculate creep damage per cycle

For insignificant cyclic loading the creep damage per cycle can be calculated from:

$$d_c = t/t_f(\sigma_{ss}) \quad (2.29)$$

where $t_f(\sigma_{ss})$ is the rupture time at the steady state end of the dwell stress. For general stress relaxation case R5 suggests a ductility exhaustion method to calculate the creep damage per cycle, where $\bar{\varepsilon}_f(\dot{\varepsilon}_c)$ is the creep ductility that considers effects of stress state and instantaneous creep strain increment during the dwell period.

$$d_c = \int_0^t \frac{\dot{\varepsilon}_c}{\bar{\varepsilon}_f(\dot{\varepsilon}_c)} dt \quad (2.30)$$

If creep damage in transition phase under the cyclic loading is more significant than the damage at the steady state, the creep damage per individual cycle must be calculated and summed for the total creep damage calculation.

Step 16. Calculate total damage

R5 suggests the linear damage summation method for the assessment of the total damage D_{c-f} , which can be expressed as $D_{c-f} = D_c + D_f$:

$$D_c = \sum_i n_i d_{ci} \quad (2.31)$$

$$D_f = \sum_i \frac{n_i}{N_{0i}} = \sum_i n_i d_{fi} \quad (2.32)$$

where D_c and D_f are the total creep and fatigue damage respectively; n_i is the number of the loading cycle.

If $D_{c-f} < 1.0$ the structure is free from a risk of the crack initiation, otherwise crack growth assessment should be performed following R5 volume 4/5.

2.3.2. ASME BPVC Section III Subsection NH

For the life evaluations of the high temperature components, ASME (Boiler and Pressure Vessel) code also has been used in many countries. ASME code covers more general and contains a broad range of rules such as general specification, material selection, design, fabrication, tests and certification process. In this section, review of those codes is performed for the integrity assessment procedure of the high temperature component, i.e. ASME BPVC Section III subsection NH (ASME NH).

ASME NH defines six loading categories consisting of design loading, service loadings (level from A to D) and test loadings. Stresses employed for analysis in ASME NH code can be mainly classified into primary stress (primary membrane stress P_m , local primary membrane stress P_L and primary bending stress P_b), secondary stress Q and peak stress F . ASME NH

also suggests taking into account the stress intensity based on the maximum shear stress theory for the multiaxial stress state.

The first stage in ASME NH is the design of components satisfying the low-temperature operating range defined by ASME code Section III NB. Operation at the high temperature may cause time-dependent damage cases, therefore following six damage modes to be considered:

- I. Creep rupture under monotonic loading*
- II. Enhanced creep deformation under monotonic loading*
- III. Creep ratchetting under constant primary load and cyclic secondary load*
- IV. Creep-fatigue damage under cyclic primary, secondary and peak stresses*
- V. Creep crack growth and non-ductile fracture*
- VI. Creep buckling*

To design the high temperature components ASME NH also defines mechanical and physical properties consisting of the time function.

ASME NH can be mainly categorised in seven subsections:

- 1) Stress intensity limit*
- 2) High temperature limit under cyclic loading*
- 3) Deformation and strain limits for structural integrity*
- 4) Creep-fatigue damage evaluation*
- 5) Creep crack growth and non-ductile fracture*
- 6) Time-independent buckling*
- 7) Time-dependent buckling*

Out of the seven subsections above, items 5, 6, and 7 are outside the scope of this thesis. Thus they are not covered here. Regarding the concerning subsections from 1 to 4, essential equations and conditions to be met are examined one by one.

Subsection 1. Stress intensity limit

In the stress intensity limit, the allowable limit of overall primary membrane stress intensity S_m should be considering temperature and time-dependent stress intensity for creep effects as S_t .

- a) For base metal in high temperature, the S_m is defined as S_{mt} which is a lower value between S_m and S_t . In the case of the material not following the typical creep curve, the definition of S_t should be modified.
- b) For weldments S_{mt} shall be taken as the lower value between S_{mt} and $0.8S_r \times R$ where S_r is the expected minimum stress to rupture strength; R is the appropriate ratio of the weld metal creep rupture strength to the base metal creep rupture strength.
- c) In ASME NH, the general membrane stress, local membrane stress, and bending stress shall satisfy the following conditions for different service loadings.

For service loading A and B (normal operation and moderate incidents), where K is the section factor for the cross-section being considered; K_t is the factor accounting for the reduction in extreme fibre bending stress due to the effect of creep, which is defined by $K_t = (K + 1) / 2$.

$$P_m \leq S_{mt} \quad (2.33a)$$

$$\begin{aligned} P_L + P_b &\leq K S_m \\ P_L + P_b / K_t &\leq S_t \end{aligned} \quad (2.33b)$$

For service loading C (infrequent incidents),

$$P_m \leq \left\{ \begin{array}{l} 1.2 S_m \\ S_t \end{array} \right\} \quad (2.34a)$$

$$\begin{aligned}
P_L + P_b &\leq 1.2KS_m \\
P_L + P_b / K &\leq S_t
\end{aligned}
\tag{2.34b}$$

For service loading D (limiting faults),

$$P_m \leq \begin{Bmatrix} 2.4S_m \\ 0.7S_u \\ 0.67S_r \\ 0.8RS_r \end{Bmatrix}
\tag{2.35a}$$

$$\begin{aligned}
P_L + P_b &\leq \begin{Bmatrix} 3.6S_m \\ 1.05S_u \end{Bmatrix} \\
P_L + P_b / K_t &\leq \begin{Bmatrix} 0.67S_r \\ 0.8RS_r \end{Bmatrix}
\end{aligned}
\tag{2.35b}$$

where S_u is the tensile strength at a given temperature. In addition, the use fraction sum for service loadings A, B and C should be less than 1.0.

Subsection 2. High temperature limit under cyclic loading

In the case of the effect of creep is significant, the inelastic analysis should be performed for the high temperature material (Austenitic steel $T > 427^\circ C$ and Ferritic steel $T > 371^\circ C$) in ASME NH. The detailed non-mandatory requirement can be found in Appendix NH-T.

Subsection 3. Deformation and strain limits for structural integrity

Deformation and strain limits at elevated temperature are provided in ASME NH so that it can prevent that the principal strains accumulated over the service life exceed the allowable inelastic strain limit for the different service loading conditions, but exceptional for service loading D.

- a) Based metal has the limits for inelastic strains which shall not exceed following conditions; a) strains averaged through thickness 1%, b) strains at the surface, due to an

equivalent linear distribution of strain through the thickness 2%, and c) local strains at any point 5%.

b) The welded region shall have the inelastic strain accumulations not exceeding a half strain value of the parent material.

c) In order to satisfy strain limits, elastic analysis can be employed through three tests numbered as A-1, A-2 and A-3. If anyone of those three tests is satisfied, the strain limits are considered as satisfied. These tests are expressed by X and Y , where

$$X = \frac{(P_L + P_b / K_t)_{\max}}{S_{y,average}} \text{ and } Y = \frac{\Delta Q_{\max}}{S_{y,average}}.$$

For test A-1:

$$X + Y \leq S_a / S_y \quad (2.36a)$$

where S_a is the lower value taken from between $1.25S_y$ and the average value of S_y .

For test A-2:

$$X + Y \leq 1.0 \quad (2.36b)$$

It is applicable for those cycles during which the average wall temperature at one of the stress extremes defining the maximum secondary stress range is below the appropriate temperature.

For test A-3: as pre-conditions, limits of NB-3222.2, NB-3222.3, and NB-3222.5 shall be fulfilled. Then additional requirements followed by shall be satisfied:

$$\sum_i \frac{t_i}{rt_{id}} \leq 0.1 \quad (2.36c)$$

$$\sum_i \varepsilon_i^c \leq 0.2\% \quad (2.36d)$$

where t_i is the total service time; t_{id} is the maximum allowable time, stress to rupture; ε_i^c is the creep strain at a stress level of $1.25S_y$. If the above conditions are satisfied, finally the following condition has to be met:

$$\Delta(P_L + P_b)_{\max} + \Delta[Q]_{\max} \leq 3\bar{S}_m \quad (2.37)$$

$3\bar{S}_m$ should be the lesser of $3S_m$ and $3\bar{S}_m$ where $1.5S_m + S_{rH}$ when only one extreme of stress difference occurs at a temperature above those effects of creep not to be negligible; $S_{rH} + S_{rL}$ when both extreme of stress difference occurs at a temperature above those effects of creep not to be negligible.

- d) In order to satisfy strain limits, simplified inelastic analysis can be employed utilising three tests numbered as B-1, B-2, and B-3.

For test B-1 and B-2, there are eight general requirements are satisfied. Essential five requirements are summarised as below:

- i) Test B-1 shall be used for structures where the peak stress is negligible, but test B-2 applies to any structures and loading.
- ii) The individual cycle as defined in the Design Specification cannot be split into sub-cycles.
- iii) Secondary stresses with elastic follow-up are classified as primary stresses for evaluations.
- iv) At least one of the maximum and minimum values of the stress cycle must be lower than the temperature where creep is negligible.
- v) Loading combination within the ratchetting regime R_1 in Figure 2.7 is not allowed.

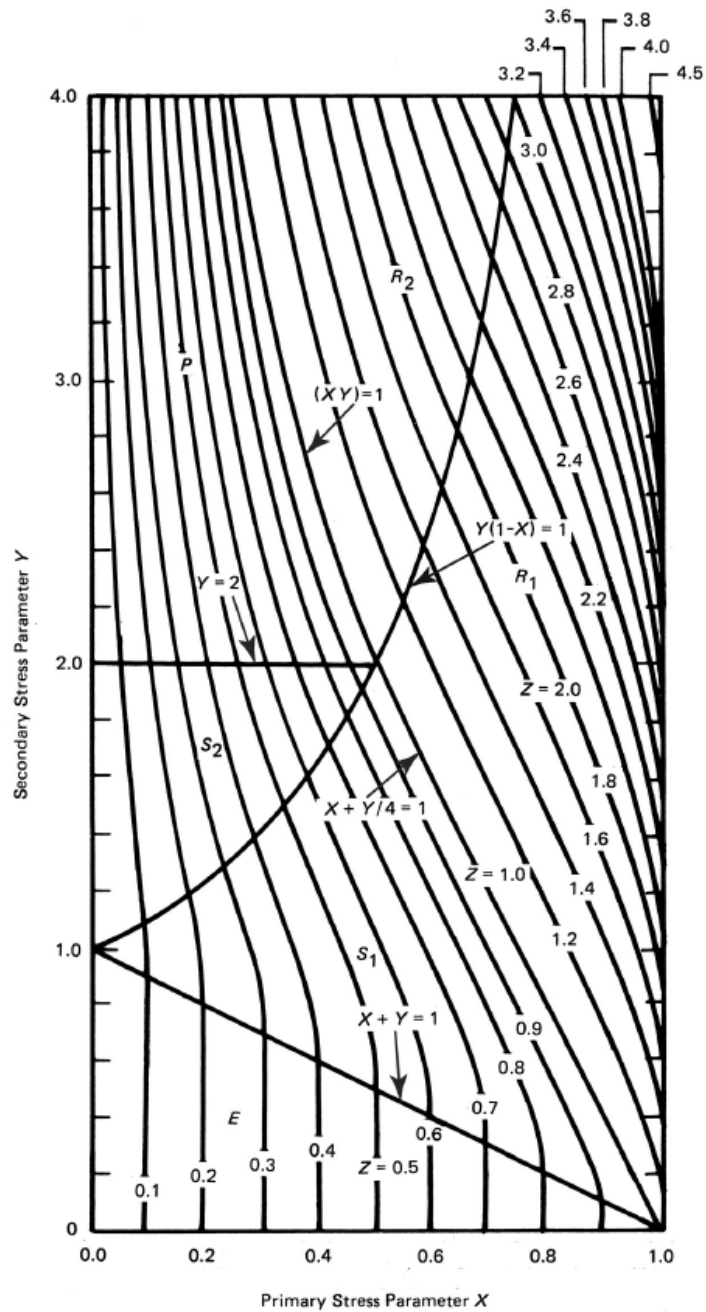


Figure 2.7 Effective creep stress parameter Z for simplified inelastic analysis using Test B-1 and B-3 [11].

If the general requirements are satisfied, for test B-1, effective creep stress can be calculated from $\sigma_c = ZS_{yL}$, where S_{yL} is the S_y value at the average wall temperature with respect to the minimum stress of the secondary stress range; Z is the creep stress parameter for Test B-1 and B-3 in Figure 2.7. If σ_c is less than S_{yH} , creep strain can be

evaluated with $1.25\sigma_c$ stress held constant throughout the temperature-time history of the entire service life.

For test B-2, the creep stress parameter can be taken from Figure 2.8.

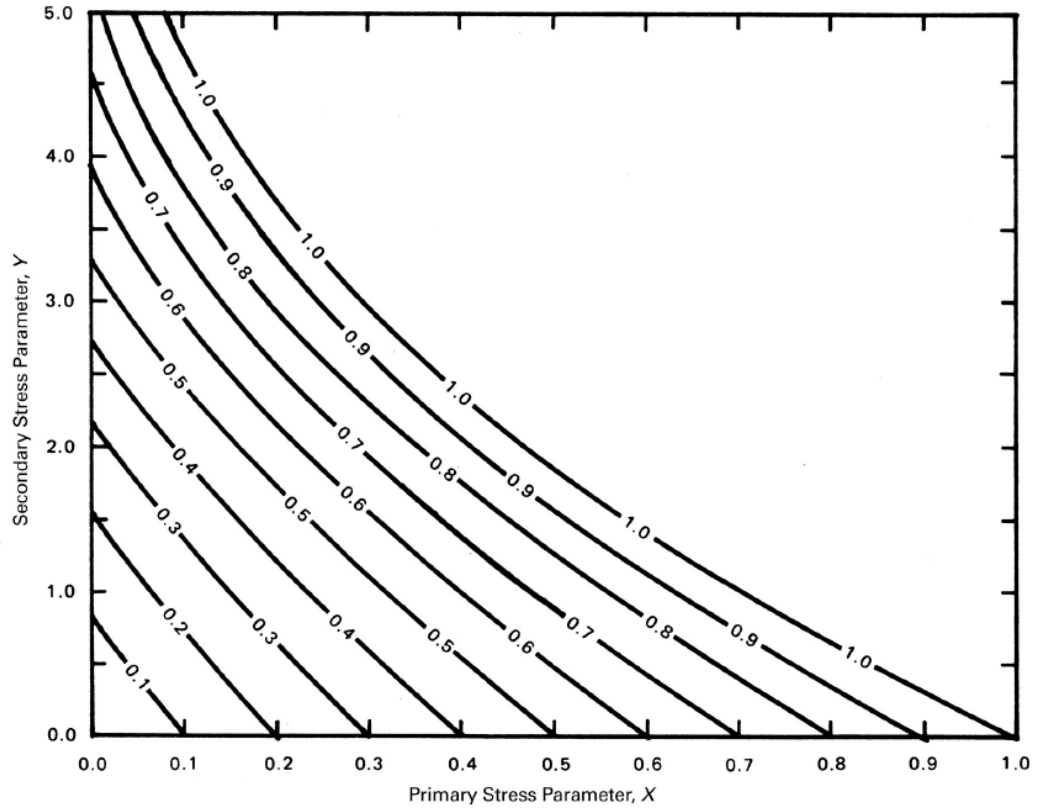


Figure 2.8 Effective creep stress parameter Z for simplified inelastic analysis using Test B-2 [11].

Test B-3 is the least conservative and allow for cycles in all regimes shown in Figure 2.7, but only applicable to the axis-symmetry structure. For cycles evaluated using test B-3, the resulting plastic ratchet strains and the enhanced creep strains must be added to strains calculated by test B-1 or B-2. The detailed equations can be found in the code NH-T-1333.

Subsection 4. Creep-fatigue damage evaluation

a) Damage equation

Combined loading of service levels A, B, and C shall be evaluated for accumulated creep-fatigue damage, including hold time and strain rate effects. The relation can be expressed as:

$$\sum_{j=1}^p \left(\frac{n}{N_d} \right)_j + \sum_{k=1}^q \left(\frac{\Delta t}{T_d} \right)_k \leq D \quad (2.38)$$

where D is the total creep-fatigue damage; $(N_d)_j$ is the number of designed allowable cycles for cycle type j corresponding to the maximum temperature occurring during the cycle; $(T_d)_k$ is the allowable time duration for given stress and the maximum temperature at the point of interest and occurring during the time interval k . Figure 2.9 presents the relation of Eq.(2.38) as creep-fatigue damage envelopes for different materials.

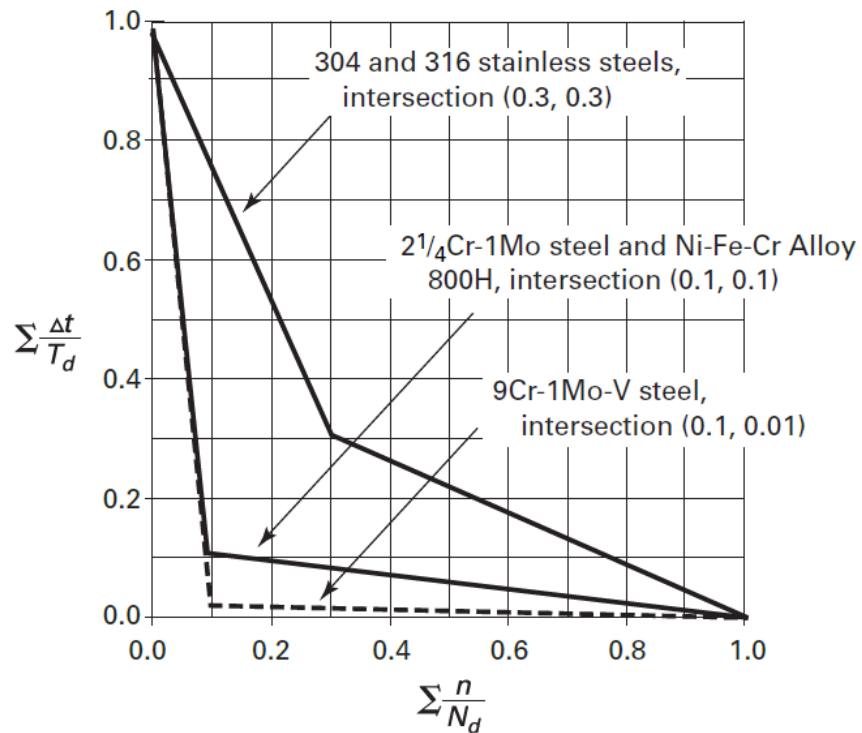


Figure 2.9 Creep-fatigue damage envelope provided in ASME NH [11].

An equivalent strain range is used to evaluate the fatigue damage for both elastic and inelastic analysis. ASME NH code provides calculation procedure of the equivalent strain range defined by five steps which detailed procedure can be found in NH-T-1413. The equivalent strain range is calculated from

$$\Delta\bar{\varepsilon}_i = \frac{\sqrt{2}}{2(1+\nu^*)} \left[\left(\Delta\varepsilon_{xi} - \Delta\varepsilon_{yi} \right)^2 + \left(\Delta\varepsilon_{yi} - \Delta\varepsilon_{zi} \right)^2 + \left(\Delta\varepsilon_{zi} - \Delta\varepsilon_{xi} \right)^2 \right]^{1/2} + \frac{3}{2} \left(\Delta\gamma_{xyi}^2 + \Delta\gamma_{yzi}^2 + \Delta\gamma_{zxi}^2 \right) \quad (2.39)$$

where $\nu^* = 0.5$ for inelastic analysis and $\nu^* = 0.3$ for elastic analysis;
 $\Delta\varepsilon_{\max} = \text{MAX}[\Delta\bar{\varepsilon}_i]$.

b) Limit using elastic analysis

There are three requirements to be met for the use of elastic analysis, and the details can be found in NH-T-1430:

- i) Satisfying the test A-1, A-2, and A-3, or the test B-1 using $Z \leq 1.0$.
- ii) If the $3S_m$ limit satisfies $\Delta(P_L + P_b + Q) \leq 3S_m$ in NB-3222.2, using for $3S_m$ the lesser of $3S_m$ and $3\bar{S}_m$.
- iii) Pressure-induced membrane and bending stresses and thermal induced membrane stresses are classified as primary stresses.

c) Fatigue damage evaluation

If the three requirements above are met in 4-b), the total strain range $\Delta\bar{\varepsilon}_{Total}$ is calculated using a modified maximum equivalent strain range $\Delta\bar{\varepsilon}_{mod}$.

$$\Delta\bar{\varepsilon}_{Total} = K_\nu \Delta\bar{\varepsilon}_{mod} + K \Delta\bar{\varepsilon}_c \quad (2.40)$$

where K_ν is the multiaxial plasticity and Poisson ratio adjustment factor; K is the local geometric concentration factor; $\Delta\bar{\varepsilon}_c$ is the creep strain increment. The detailed procedure for calculating $\Delta\bar{\varepsilon}_{mod}$, K_ν , and K are provided in NH-T-1432.

d) Creep damage evaluation

ASME NH provides two procedures which one is the general procedure consisting of 10 steps, and the other one is the alternative procedure which cannot be used for any service life if the $\Delta\bar{\varepsilon}_{Total}$ exceeds $3\bar{S}_m / E$. In here, the general procedures are briefly described as five steps, but the alternative procedures can be found in NH-T-1433.

- i) Define the total number of hours t_H at a temperature over $425^\circ C$ and the dwell temperature T_{HT} to be equal to the operating local metal temperature during operation.
- ii) Define the average cycle time \bar{t}_j and select the time-independent isochronous stress-strain curve corresponding to the T_{HT} .
- iii) Evaluate stress relaxation during the \bar{t}_j considering multiaxial stress state or by entering the appropriate isochronous stress-strain curve.
- iv) Define t_{TRAN} , S_{TRAN} , and T_{TRAN} , which are the time point of \bar{t}_j expended during elevated temperature transient condition, load controlled stress intensity at the time point, and the cycle transient temperature respectively.
- v) Create envelope stress-time history using t_{TRAN} , S_{TRAN} , and T_{TRAN} and calculate the allowable time duration T_d considering stress factor K' , finally evaluate creep damage using Eq.(2.38)

e) Creep-fatigue damage using inelastic analysis

An equivalent strain range calculated using inelastic analysis can be used to calculate N_d for the fatigue damage evaluation without modifications. For creep damage evaluation, creep damage term in Eq.(2.38) shall be replaced to integration form as:

$$\int_0^{\Delta t} \frac{dt}{T_d} \quad (2.41)$$

If multiaxial stress state needs to be considered, effective stress is calculated from

$$\sigma_{eff} = \bar{\sigma} \exp \left[C \left(\frac{J_1}{S_s} - 1 \right) \right] \quad (2.42)$$

where $J_1 = \sigma_1 + \sigma_2 + \sigma_3$; $S_s = [\sigma_1^2 + \sigma_2^2 + \sigma_3^2]^{1/2}$; the constant C is defined depending on the type of material. The constant can be found in NH-T-1411.

f) Creep-fatigue at welds

Since the ductility of the weld metal is limited at high temperatures or there is a high probability of strain concentration at the weld heat affected zone, the creep-fatigue evaluation shall use reduced values of an allowable number of cycle N_d and the allowable time T_d in Eq.(2.38). The value of N_d shall be one-half the value permitted for the parent material, and the value of T_d shall be determined by multiplying the parent material stress to rupture value by the weld strength reduction factors. Details can be found in NH-T-1715.

2.4 Chapter Summary

The review of structural behaviours under cyclic load at elevated temperature is provided. It describes expected failure mechanisms for individual structural response and provides concise and essential structural integrity assessment procedures.

For cyclic plasticity behaviour, stress-strain relationship under cyclic load after yielding is clearly defined and explained with Bree diagram. Where plastic shakedown response that may require low cycle fatigue damage assessment, a variety of evaluation methods to construct the $\varepsilon - N$ curves are introduced, and it describes suitable materials which the $\varepsilon - N$ curves show the best predictability.

Creep induced failure mechanisms of structures under cyclic load are introduced by utilising graphical materials which show various creep-cyclic plasticity behaviours. Creep-fatigue damage models of the damage summation method and the unified assessment method are presented, and the typical assessment procedures provided in ASME NH and RCC-MRx codes are described.

Finally, crack initiation assessment procedure provided in the design procedure, R5 procedures and the design code, ASME NH, are summarised in step by step process so that users can overview of the large volume of procedures and rules easily.

3. Advanced Numerical Direct Method

3.1 Introduction

To define the structural response under the cyclic loading is a complex process, and it requires advanced computational analysis such as Incremental Finite Element Analysis. Currently, Incremental Finite Element Analysis has been used to define the structural response of components subjected to a variety of load combination. However Incremental Finite Element Analysis is only able to evaluate that the structure exhibits a specific structural response among shakedown, alternating plasticity and ratcheting, with respect to a given cyclic load condition. Furthermore, it requires a significant number of trial and error calculations in order to create the structural response boundaries like Bree diagram [35]. Consequently, many Direct Methods have been developed and used in order to obtain fast and approximate limit load and shakedown boundaries.

Iterative elastic analysis Direct Methods include the Elastic Compensation Method (ECM) [48], the Dhalla Reduction Procedure [49], the Gloss R-Node Method [50], and the Linear Matching Method (LMM) [51]. The ECM was further modified by Yang *et al.* as Modified Elastic Compensation Method (MECM) [52]. Muscat and Mackenzie presented a superposition method to establish elastic shakedown loads using the lower bound theorem [53]. Muscat *et al.* introduced a non-linear superposition method [54] based on Polizzotto's work [55] to estimate an elastic shakedown boundary of a structure subjected to a combined cyclic and steady mechanical load. Abdalla *et al.* presented shakedown limit loads for a two-bar structure problem and the Bree cylinder problem using a simplified technique [56]. Chen and Ponter extended the scope of the LMM to include ratchet limit, creep rupture limit, and cyclic plasticity considering creep-fatigue interaction [57, 58].

The LMM matches the non-linear material response to a linear material behaviour using iterative computational processes by changing the elastic modulus at each integration point of a finite element model. For the shakedown limit analysis, the LMM computes both upper bound and lower bound limit multipliers under cyclic loadings, creating a load envelope to show a limit of structural responses as Bree diagram. The LMM was extended to the Direct Steady Cycle Analysis (DSCA) [59] that calculates the stabilised response of a structure subjected to cyclic loadings with accuracy and efficiency that supersedes other traditional Direct Methods [20]. The LMM DSCA method was further extended by Chen *et al.* to evaluate

a structural response to creep-cyclic plasticity behaviour in the steady state. The extended Direct Steady Cycle Analysis method (eDSCA) has been actively being utilised to assess the low cycle fatigue, and the creep-fatigue damages [39, 60]. Validity and applicability of the LMM framework have also been acknowledged by a variety of commercial industry partners [17, 19, 60], in particular, R5 have selected the LMM as the commercial standard [12]. Also, the LMM eDSCA has been used recently for a couple of studies regarding investigations on creep-cyclic plasticity behaviours of metal matrix composites [61, 62].

In this chapter, numerical procedures of shakedown analysis, DSCA, and eDSCA which are part of the Linear Matching Method framework are briefly presented. The numerical procedure of shakedown analysis is described in Section 3.2. The numerical procedure of DSCA used for the steady cycle analysis and the ratchet limit analysis is presented in Section 3.3. Section 3.4 describes the numerical procedures of eDSCA including the modified LMM eDSCA which is enhanced by the author of this thesis. The modified eDSCA is the extended version of eDSCA which is capable of predicting more accurate creep-cyclic plasticity behaviour of engineering components under non-isothermal, and multiple-dwell conditions.

3.2 Shakedown Analysis

It is assumed that a structure follows the elastic-perfectly plastic model (EPP) with a volume V and a surface area of S as well as satisfying the von-Mises yield condition. The structure is subjected to the cyclic thermal load $\lambda\theta(t)$ acting across the V and the steady mechanical load $\lambda P(t)$ imposing on the part of the surface S_T over the period $0 \leq t \leq \Delta t$, where λ denotes load parameters. A remaining surface S_R ($S_R = S - S_T$) is constrained by no displacement rate ($\dot{U} = 0$). Upon the loading and boundary conditions, a linear elastic stress solution can be expressed by Eq.(3.1):

$$\hat{\sigma}_{ij}^e(t) = \lambda \hat{\sigma}_{ij}^\theta(t) + \lambda \hat{\sigma}_{ij}^P(t) \quad (3.1)$$

where $\lambda \hat{\sigma}_{ij}^\theta$ and $\lambda \hat{\sigma}_{ij}^P$ denote changing elastic stresses corresponding to $\theta(t)$ and $P(t)$, respectively. For the cyclic problem, a general form of the elastic solution can be expressed by Eq.(3.2) with three different components:

$$\hat{\sigma}_{ij}(t) = \hat{\sigma}_{ij}^e(t) + \bar{\rho}_{ij} + \rho_{ij}^r(t) \quad (3.2)$$

where the elastic stress $\hat{\sigma}_{ij}^e(t)$; the constant residual stress $\bar{\rho}_{ij}$; the varying residual stress $\rho_{ij}^r(t)$. The history of $\rho_{ij}^r(t)$ is the change in the residual stress within the cycle and satisfies $\rho_{ij}^r(0) = \rho_{ij}^r(\Delta t)$, so that the stress and strain rates will become asymptotic to a cyclic state. For the shakedown analysis, $\rho_{ij}^r(0) = 0$ must be achieved. Therefore ratchetting response of the structure will not occur with the zero plastic strain accumulation during the cycles.

The shakedown analysis considers a global minimisation process to evaluate the $\bar{\rho}_{ij}$ imposed by the combined cyclic and steady loads. The shakedown condition and the global minimisation process of the energy based on the Koiter's theorem [23] are integrated, giving a minimisation function in an incremental form as Eq. (3.3), where $\Delta\varepsilon_{ij}$ denotes a plastic strain increment occurring at the time t_n , n increases from 1 to N during the cycle, and λ_{SD}^{UB} is a shakedown upper bound multiplier.

$$I(\Delta\varepsilon_{ij}, \lambda_{SD}^{UB}) = \int_V \sum_{n=1}^N \left\{ \sigma_{ij}^n \Delta\varepsilon_{ij}^n - \lambda_{SD}^{UB} \hat{\sigma}_{ij}(t_n) \Delta\varepsilon_{ij}^n \right\} dV \geq 0 \quad (3.3)$$

Transforming the Eq. (3.3) the λ_{SD}^{UB} can be obtained as Eq.(3.4):

$$\lambda_{SD}^{UB} = \frac{\int_0^V \int_0^{\Delta t} \sigma_y \bar{\dot{\varepsilon}}(\dot{\varepsilon}_{ij}) dt dV}{\int_0^V \int_0^{\Delta t} (\hat{\sigma}_{ij}^{\Delta} \dot{\varepsilon}_{ij}) dt dV} \quad (3.4)$$

where $\dot{\varepsilon}_{ij}$ is a kinematically admissible strain rate and $\bar{\dot{\varepsilon}}$ is the effective strain rate $\bar{\dot{\varepsilon}} = \sqrt{\frac{2}{3} \dot{\varepsilon}_{ij} \dot{\varepsilon}_{ij}}$. The upper bound multiplier is updated by the iterative process till converging to the least upper bound limit, satisfying $\lambda_{SD}^{UB} \geq \lambda_{SD}$, where λ_{SD} is the exact shakedown limit. The shakedown lower bound multiplier λ_{SD}^{LB} is calculated according to Melan's Theorem [22]. By checking the $\rho_{ij}^r(t)$ within the computation process of the upper bound multiplier, the iterative process continues to calculate λ_{SD}^{LB} until where the modified elastic solution at each

integration point does not violate the yield condition of the material, satisfying $\lambda_{SD}^{LB} \leq \lambda_{SD}$, λ_{SD}^{LB} can be expressed by Eq.(3.5).

$$f(\lambda_{SD}^{LB} \hat{\sigma}_{ij}(t) + \bar{\rho}_{ij}) \leq 0 \quad (3.5)$$

3.3 Direct Steady Cycle Analysis (DSCA)

Direct steady cycle response can be achieved by calculating varying residual stress ρ_{ij}^r and corresponding plastic strain range of a steady state by an incremental minimization of the energy function $I(\dot{\epsilon}_{ij}^k, \lambda)$ for the predefined cyclic loads over the time period in Section 3.2:

$$I(\dot{\epsilon}_{ij}^k, \lambda) = \int_V \int_0^{\Delta t} (\sigma_{ij}^k - \sigma_{ij}) \dot{\epsilon}_{ij}^k dt dV \quad (3.6)$$

where σ_{ij}^k denotes a yield stress corresponding to the kinematically admissible strain rate $\dot{\epsilon}_{ij}^k$. Based on a steady cycle response of the structure obtained by DSCA, ratchet limit of the structure is calculated by performing a global minimization of the shakedown theorem with respect to an extra constant load $\hat{\sigma}_{ij}^F$ where the varying residual stress $\rho_{ij}^r(x, t)$ at steady cycle enhances the cyclic elastic solution. Hence the cyclic elastic solution for ratchet limit analysis can be defined by:

$$\hat{\sigma}_{ij} = \lambda \hat{\sigma}_{ij}^F + \hat{\sigma}_{ij}^\Delta(x, t) + \rho_{ij}^r(x, t) \quad (3.7)$$

where $\hat{\sigma}_{ij}^\Delta(x, t)$ is an elastic solution with constant residual stress $\bar{\rho}_{ij}^r$. Direct steady cycle analysis (DSCA) in the LMM framework performs the calculation of the accumulated residual stress history. DSCA utilises a series of iterative cycles defined as $m = 1, 2, \dots, M$. Within each iterative sub cycle m , load instances as $k = 1, 2, \dots, K$ are defined. Both constant residual stress $\bar{\rho}_{ij}^r$ and varying residual stress $\Delta\rho_{ij}^r$ corresponding to the elastic solution can be calculated as Eq.(3.8) and Eq.(3.9):

$$\bar{\rho}_{ij}^r = \sum_{m=1}^M \sum_{k=1}^K \Delta \rho_{ij}^r(x, t_k)_m \quad (3.8)$$

$$\rho_{ij}^r(x, t_k) = \bar{\rho}_{ij}^r(x) + \sum_{l=1}^k \Delta \rho_{ij}^r(x, t_l)_M \quad (3.9)$$

The converged plastic strain developed at time t_k can be expressed as Eq.(3.10):

$$\Delta \varepsilon_{ij}^p(x, t_k) = \frac{1}{2\bar{\mu}_n(x, t_k)} \left[\hat{\sigma}_{ij}^{\Delta'}(x, t_k) + \rho_{ij}^r(x, t_k) \right] \quad (3.10)$$

where $\bar{\mu}$ is the iterative shear modulus calculated by the LMM and (') indicates deviatoric stress and strain. Outlining von-Mises yield criterion in associated with elastic perfectly plasticity, the ratchet upper bound multiplier λ_{UB}^{RC} can be defined by:

$$\lambda_{UB}^{RC} = \frac{\int \sum_{k=1}^K \sigma_y \bar{\varepsilon}(\Delta \varepsilon_{ij}^k) dV - \int \sum_{k=1}^K \left[\hat{\sigma}_{ij}^{\Delta}(t_k) + \rho_{ij}^r(t_k) \right] \Delta \varepsilon_{ij}^k dV}{\int \hat{\sigma}_{ij}^F \left(\sum_{k=1}^K \Delta \varepsilon_{ij}^k \right) dV} \quad (3.11)$$

where $\bar{\varepsilon}$ is the effective strain $\bar{\varepsilon}(\Delta \varepsilon_{ij}^k) = \sqrt{\frac{2}{3} \Delta \varepsilon_{ij}^k \Delta \varepsilon_{ij}^k}$. Based on this procedure, the LMM calculates a series of ratchet upper bounds that converge to the least ratchet upper bound limit. For the ratchet lower bound limit λ_{LB}^{RC} , the varying residual stress field is considered together with the constant residual stress at every iterative process. Modifying Eq.(3.1) with reference to Eq.(3.7), the lower bound multiplier is given by:

$$f \left(\lambda_{LB}^{RC} \hat{\sigma}_{ij}^F + \hat{\sigma}_{ij}^{\Delta} + \rho_{ij}^r \right) \leq 0 \quad (3.12)$$

3.4 Extended Direct Steady Cycle Analysis (eDSCA)

The eDSCA procedure calculates the cyclic stress history at the steady cyclic state associated with residual stresses accumulated by inelastic strains either plastic or creep during the loading cycle. The eDSCA utilise a similar minimisation procedure with Eq.(3.3) which has an assumption that plastic strain only occurs at a time t_n , where N (from $n = 1$ to N) denotes a total number of loading instances. The minimisation function of the eDSCA in an incremental form can be given by Eq.(3.13).

$$I^n(\Delta\varepsilon_{ij}^n) = \int_V \left\{ \sigma_{ij}^n \Delta\varepsilon_{ij}^n - [\hat{\sigma}_{ij}(t_n) + \rho_{ij}^r(t_n)] \Delta\varepsilon_{ij}^n \right\} dV \geq 0 \quad (3.13)$$

By an iterative process, the strain increment $\Delta\varepsilon_{ij}^n$ can be calculated by the minimisation process until the requested a total number of cycles M . The number of load instances N is performed as sub-cycles within each cycle m , where m (from $m = 1$ to M). Hence, the accumulated residual stress for n^{th} load instance at m^{th} the cycle of iterations can be expressed by Eq.(3.14).

$$\rho_{ij}^r(t_n)_m = \sum_{i=1}^{m-1} \sum_{n=1}^N \Delta\rho_{ij}^r(t_n)_i + \sum_{i=1}^n \Delta\rho_{ij}^r(t_i)_m \quad (3.14)$$

For example, if the cycles m and $m+1$ are only considered, the iterative shear modulus $\bar{\mu}_m(t_n)$ at a load instance t_n can be defined by Eq. (3.15), where $\sigma_y(t_n)_m$ denotes the von-Mises yield stress of the EPP model, which is substituted to creep flow stress $\bar{\sigma}_c$ when the t_n involves a load instance of creep.

$$\bar{\mu}_{m+1}(t_n) = \bar{\mu}_m(t_n) \frac{\sigma_y(t_n)_m}{\bar{\sigma}(\hat{\sigma}_{ij}(t_n) + \rho_{ij}^r(t_n)_m)} \quad (3.15)$$

Without consideration of a load instance of creep, the inelastic strain increment $\Delta\varepsilon_{ij}(t_n)_{m+1}$ at the cycle $m+1$ can be calculated by Eq. (3.16), where $\rho_{ij}^r(t_{n-1})$ is the accumulated previous residual stress before the time t_n and the notation (\cdot) refers to the deviatoric component:

$$\Delta \varepsilon_{ij}(t_n)_{m+1} = \frac{1}{2\bar{\mu}_m(t_n)} \left\{ \hat{\sigma}_{ij}(t_n) + \rho_{ij}^r(t_{n-1})_{m+1} + \Delta \rho_{ij}^r(t_n)_{m+1} \right\} \quad (3.16)$$

where the residual stress accumulated at the cycle m is the summation of the previous varying residual stress and constant residual stress.

$$\rho_{ij}^r(t_{n-1})_m = \rho_{ij}^r(t_0) + \Delta \rho_{ij}^r(t_1) + \Delta \rho_{ij}^r(t_2) + \dots + \Delta \rho_{ij}^r(t_{n-1}) \quad (3.17)$$

When Ramberg-Osgood(RO) material model is used for expressing the strain hardening behaviour, the following relationship is considered, where $\Delta \bar{\sigma}$ and $\Delta \bar{\varepsilon}$ are true stress and strain ranges; B and β are hardening constants.

$$\frac{\Delta \bar{\varepsilon}}{2} = \frac{\Delta \bar{\sigma}}{2E} + \left(\frac{\Delta \bar{\sigma}}{2B} \right)^{\frac{1}{\beta}} \quad (3.18)$$

The second term on the right-hand side of Eq.(3.18) is the plastic strain amplitude, and the plastic strain range $\Delta \bar{\varepsilon}_p$ can be expressed as

$$\Delta \bar{\varepsilon}_p = 2 \left(\frac{\Delta \bar{\sigma}}{2B} \right)^{\frac{1}{\beta}} \quad (3.19)$$

Eq.(3.19) can be transformed to half stress range and redefined with respect to iterative von-Mises stress $\sigma_0(t_n)$ which replaces the $\sigma_y(t_n)_m$ in Eq.(3.15).

$$\sigma_0(t_n) = B \left(\frac{\Delta \bar{\varepsilon}(\Delta \varepsilon_{ij}^n)}{2} \right)^{\beta} \quad (3.20)$$

3.4.1 Original numerical procedure for creep strain and flow stress

The following time hardening power law is used to calculate creep strain accumulated during a dwell period:

$$\dot{\bar{\epsilon}}^c = A \cdot \bar{\sigma}^n \cdot t^m \quad (3.21)$$

where $\dot{\bar{\epsilon}}^c$ is the effective creep strain rate; $\bar{\sigma}$ is the von-Mises stress, t is the dwell time; A , n and m are creep constants.

It is assumed that the stress relaxation process follows a linear relation which can be expressed as an elastic follow-up factor Z , where \bar{E} is the effective Young's modulus which can be defined as $\bar{E} = 3E/2(1+\nu)$; E is Young's modulus; ν is the Poisson's ratio; $\dot{\bar{\sigma}} = \dot{\bar{\sigma}}(\sigma_{ij})$.

$$\dot{\bar{\epsilon}}^c = -\frac{Z}{\bar{E}} \dot{\bar{\sigma}} \quad (3.22)$$

Eq.(3.21) and Eq.(3.22) are combined and then integrated the combined equation over the dwell time Δt :

$$\frac{A\bar{E}\Delta t^{m+1}}{Z(m+1)} = \frac{1}{n-1} \left(\frac{1}{\bar{\sigma}_c^{n-1}} - \frac{1}{\bar{\sigma}_s^{n-1}} \right) \quad (3.23)$$

where $\bar{\sigma}_s$ is the start of the dwell stress; $\bar{\sigma}_c$ is the end of the dwell stress (creep flow stress) which replace the $\sigma_y(t_n)_m$ in Eq.(3.15) within the iterative process.

Integrating Eq.(3.22) over the dwell time Δt and then combined with Eq.(3.23) in order to eliminate Z/\bar{E} , where $\Delta\bar{\epsilon}^c$ is the effective creep strain increment over the dwell time.

$$\Delta\bar{\epsilon}^c = \frac{A(n-1)\Delta t^{m+1}(\bar{\sigma}_s - \bar{\sigma}_c)}{(\bar{\sigma}_c^{-n+1} - \bar{\sigma}_s^{-n+1})(m+1)} \quad (3.24)$$

The creep strain rate $\dot{\bar{\epsilon}}^c$ at the end of the dwell time Δt is calculated from Eq.(3.23) and Eq.(3.24).

$$\dot{\bar{\epsilon}}^c = \frac{\Delta \bar{\epsilon}^c (m+1) \bar{\sigma}_c^n}{(n-1)(\bar{\sigma}_s - \bar{\sigma}_c) \Delta t} (\bar{\sigma}_c^{-n+1} - \bar{\sigma}_s^{-n+1}) \quad (3.25)$$

Initially, the iterative process starts with estimated $\bar{\sigma}_s$ and $\bar{\sigma}_c$ values, and the Eq.(3.24) and Eq.(3.25) compute new creep flow stress $\bar{\sigma}_c^f$ using Eq.(3.26) so that the $\bar{\sigma}_c^f$ replace $\sigma_y(t_n)_m$ in Eq.(3.15) to carry out the linear matching condition.

$$\bar{\sigma}_c^f = \left(\frac{\dot{\bar{\epsilon}}^c}{A \Delta t^m} \right)^{\frac{1}{n}} \quad (3.26)$$

3.4.2 *The modified numerical procedure for creep strain and flow stress*

Three modifications have been made by the author of this thesis for calculating the creep strain and flow stress more practically.

The first improvement is to implement non-isothermal creep properties into cyclic creep and plastic analysis.

The second improvement is to calculate instantaneous dwell stress, principal stresses and mean or hydrostatic stresses at user-defined dwell time increment within dwell period, which allows more accurate prediction of creep-fatigue damage life.

The final improvement is to implement the effects of multi-dwells on calculations of the creep strain and flow stress.

In this section, the modified numerical procedures implemented in the UMAT are briefly introduced. UMAT is the user subroutine which can be used to define the mechanical constitutive behaviour of a material provided in a commercial finite element analysis software ABAQUS. It can be used with any procedure that includes mechanical behaviour. Hence user can analyse complex structural behaviour with own developed UMAT subroutine for analysis

functions that ABAQUS do not provide as a default function.

In order to implement the non-isothermal effects, the creep constant A in Eq.(3.21) is defined for the variation of the temperature by adopting Arrhenius law,

$$A = A^* \exp\left(\frac{-Q_{eng}}{R_{gas} T}\right) \quad (3.27)$$

where Q_{eng} is the activation energy [kJ / mol]; R_{gas} is global gas constant [$kJ / mol / K$]; T is the temperature in Kelvin; A^* [$MPa^{-n} \cdot h^{-m}$] is the frequency factor.

In order to predict the creep stress relaxation history, it is assumed that the resulting dwell stress against a time increment has the following relationship [38] for the arbitrary elastic follow-up Z value as Eq.(3.23),

$$\bar{\sigma}_{c,i} = \left\{ \bar{\sigma}_{s,i}^{-n+1} + \frac{1}{Z} \left(\frac{n-1}{m+1} \right) B \bar{E} \Delta t_i^{m+1} \right\}^{\frac{-1}{n-1}} \quad (3.28)$$

where $\bar{\sigma}_{c,i}$ and $\bar{\sigma}_{s,i}$ are the instantaneous end of the dwell stress and the instantaneous start of the dwell stress respectively; B is the creep coefficient for the instantaneous time increment Δt_i over the dwell time Δt . Hence Eq.(3.24) can be transformed into the following equation Eq.(3.29) to calculate the instantaneous effective creep strain increment, and the creep strain increment over the dwell period can be calculated as $\Delta \bar{\epsilon}^c = \Delta \bar{\epsilon}_{\Delta t}^c$:

$$\Delta \bar{\epsilon}_i^c = \frac{A(n-1)\Delta t_i^{m+1}(\bar{\sigma}_s - \bar{\sigma}_{c,i})}{\left(\frac{1}{\bar{\sigma}_{c,i}^{n-1}} - \frac{1}{\bar{\sigma}_s^{n-1}} \right) (m+1)} \quad (3.29)$$

Utilising the dwell stress history, the principal stress history ($\Delta \sigma_1$, $\Delta \sigma_2$, and $\Delta \sigma_3$) and the mean stress history ($\Delta \sigma_m = \frac{\Delta \sigma_1 + \Delta \sigma_2 + \Delta \sigma_3}{3}$) can be predicted over the dwell time using

interpolation techniques, the analysed $\Delta\sigma_1$ and $\Delta\sigma_m$ are used to calculate a creep damage prediction based on time fraction rule and stress modified exhaustion method allowing for multi-axial ductility factors [40, 63]. All the mathematical formula shown in Chapter 6 is also implemented in this modified version of eDSCA for the damage calculations.

For the multi-dwell effects, the eDSCA has been modified as the users can input a number of loading instances in the UMAT subroutines as they wish. The enhanced procedure makes the resultant stress and strain from a prior loading instance to become a residual stress field for stress and strain calculations in the next loading instance.

3.5 Chapter Summary

Structural integrity assessment of engineering components subjected to cyclic loading is more difficult and complex than the one subjected to monotonic loading owing to cyclic plasticity behaviours of materials under variations of loading condition. Therefore, the design and assessment codes have been putting more efforts for many years to calculate more reliable load boundary while avoiding ratchetting response.

The numerical technique, the LMM Framework, introduced in this chapter is a very powerful tool to construct limit load, shakedown limit and ratchet limit boundaries with both upper bound and lower bound approaches. Compared to numerical techniques provided by the design codes, the LMM produces much less conservative results using very small computational resources less than 10% of the conventional methods. For the creep-cyclic plasticity analysis, EDF has acknowledged internally that the Linear Matching Method potentially provides more accurate values of start of dwell stress, elastic follow-up factor and strain range than values obtained using R5 volume 2/3 procedure.

Since the LMM was developed by Chen and Ponter, many researchers have been involved in the development of this powerful method. However, there is room for further development within the framework which includes but not restricted to the inclusion of kinematic hardening model in the shakedown limit analysis and strain hardening creep law in the creep-cyclic plasticity analysis. These further achievements will benefit the use of the framework with confidence in R5 assessment and other design code such as RCC-MRx.

4. Cyclic Plasticity of 90° Back-to-Back Pipe Bends under Cyclic Thermal Loading, Cyclic Bending, and Constant Internal Pressures

4.1 Introduction

Power plant piping systems are designed to avoid plastic collapse under monotonic loading and low cycle fatigue and ratcheting failures under cyclic loading. Piping systems are mainly composed of straight pipe and pipe bend components. Pipe bends are generally employed for routing piping systems by connecting to straight pipes, especially back-to-back pipe bends are necessary components for confined space applications. Structural integrity assessment of pipe bends is more complicated than for a straight pipeline [64-66]. Moreover, when the pipe bends are subjected to cyclic loading at elevated temperature, the yield stress of the material is reduced, potentially leading to severe deformation or even failure due to low cycle fatigue or incremental plastic collapse. It is, therefore, necessary to consider temperature-dependent yield effects when evaluating shakedown and ratchet limit boundaries of pipe bends under operating load conditions. Structural integrity assessment under cyclic loadings is an essential feature in a wide range of engineering applications, and many types of research have reported cyclic plasticity behaviour of engineering problems [67-70].

Integrity assessment of pipe bends subjected to cyclic bending moments and constant internal pressures has been the subject of several previous studies [71-76]. However, no research has been presented for the cyclic plasticity response of the 90° back-to-back pipe bends under thermo-mechanical load with temperature dependent material properties. This research presents the results of a detailed investigation cyclic plastic behaviour of 90° back-to-back pipe bends under cyclic in-plane and out-of-plane bending and cyclic thermal load with constant internal pressure. The obtained results are verified by the full incremental cyclic analyses using Abaqus step-by-step method. Additionally, systematic parametric studies are carried out for investigating the geometry effects of the pipe bend structure on the cyclic plasticity behaviour.

The finite element model of the pipe bends structure including geometry data, material properties and applied boundary conditions are presented in Section 4.2. Numerical results of the pipe bends structure subjected to cyclic in-plane bending and constant internal pressures are presented in Section 4.3. Cyclic plasticity behaviours of the pipe structure subjected to

cyclic out-of-plane bending and constant internal pressures are presented in Section 4.4. For both Sections 4.3 and 4.4 provide comprehensive parametric studies for the geometry effects under the different directions of the cyclic bending. Section 4.5 presents the effects of cyclic thermal loading on the cyclic plasticity behaviours of the identical pipe structure pressurised by the same loading condition of the internal pressures. Section 4.6 concludes this work.

4.2 Finite Element Model

4.2.1 Geometry of the 90° back-to-back pipe bends

The geometry of the 90° back-to-back pipe bends with the two straight pipe ends is shown in . The pipe dimensions conform to U.S standard pipe size 10inch NPS Schedule 40. The mean pipe diameter is D_m , the straight end runs are length L , and the bend connecting run length is L_m . The pipe bend geometry is considered in terms of two ratios: R/r and r/t , where R is the bend radius, r is the mean radius of the pipe, and t is the wall thickness. Dimensions of the configuration are summarised in Table 4.1. Here, the pipe bends have r/t ratio of 14.23 and R/r ratio of 2.89. Bend behaviour is generally described in terms of these ratios and the pipe bend parameter or pipe factor h :

$$h = \frac{R/r}{r/t} = \frac{Rt}{r^2} \quad (4.1)$$

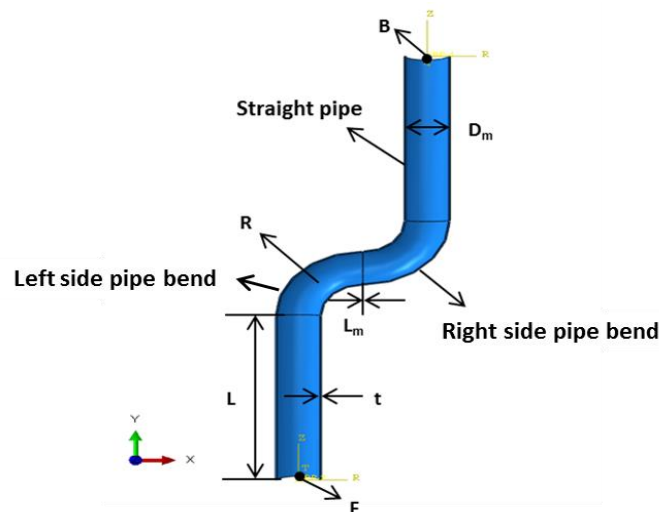


Figure 4.1 Geometry of the 90° back-to-back pipe bends with two attached vertical straight pipe sections.

Complete 3D finite element models of the configurations in Abaqus using 3D solid C3D20R quadratic elements, as shown in Figure 4.2. Following a mesh refinement study, the configuration of the pipe system was meshed with 13,800 elements. Three elements are created through the wall thickness. Each pipe bend has 25 elements along its length and 50 around its circumference. The vertical straight runs L are meshed with fifty elements with the mesh refined towards the intersection with the pipe bend.

Table 4.1. Key dimensions of the 90° back-to-back pipe bends and the two straight pipes (all dimensions in mm).

D_m	t	R	L_m	$L = 5D_m$
263.78	9.27	381	0	1318.9

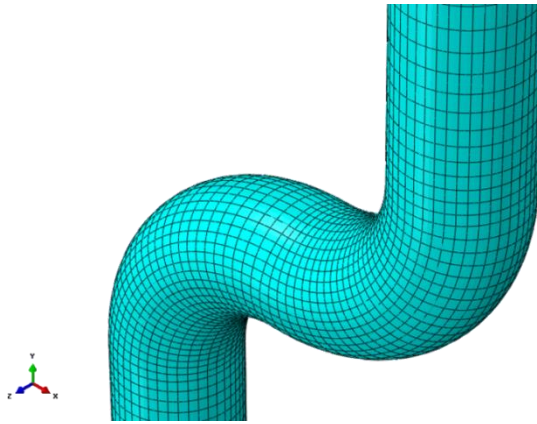


Figure 4.2 Full model of 90° back-to-back pipe bends with 3D solid elements meshed.

4.2.2 Material properties and Boundary and loading conditions

The material used in this work is the same material properties of Type 304 stainless steel. Young's modulus of 193.74 GPa and Poisson's ratio of 0.2642 are used. Temperature-dependent yield stresses up to 550°C used for each analysis are listed in Table 4.2, and the elastic-perfectly plastic model is used. The displacement behaviour of the pipe bend is assumed to follow small deformation theory. The yield stress at room temperature is used for the shakedown and the ratchet analyses including the parametric studies in Sections 4.3 and 4.4. The temperature-dependent parameters are employed for a numerical study involving the cyclic thermal loading in Section 4.5. The material is assumed to have a thermal conductivity

of $43 [Wm^{-1}K^{-1}]$ and the thermal expansion coefficient of $1.7 \times 10^{-5} [^{\circ}C^{-1}]$. The thermal expansion effect of a long pipe is achieved by applying an equation to constrain the top surface of the right side vertical pipe as a plane condition.

Table 4.2. Temperature dependent yield stress.

Temperature [$^{\circ}C$]	20	100	200	300	400	500	550
$\sigma_y [MPa]$	271.93	253	229	207	188	172	156

As shown in , two cylindrical coordinate systems are created at both the top and bottom of the pipe bends model. A reference node is created at the origin of each cylindrical coordinate system as B for the top and F for the bottom. All nodes placed on the bottom surface of the pipe structure are constrained by utilising Kinematic Coupling to follow all motions of the node F except the expansion/contraction in the radial direction. The same constraint applies to all nodes on the top surface, which are restrained against motions of the node B but allowed the pipe to move freely in the radial direction.

The cyclic in-plane bending and the out-of-plane bending are achieved by a clockwise moment about the z -axis and the x -axis each applied on node B . The resultant moment values are normalised by a reference moment, which is the limit moment M_L for the thin wall straight pipe as given:

$$M_L = \sigma_y D_m^2 t \quad (4.2)$$

Constant internal pressure is applied to the inner surfaces of the whole structure. It is assumed that the pipe bends are in a closed-end condition; thus the axial tension is applied on the top surface of the upper straight pipe proportionally to the internal pressure. The internal pressure and axial tension are normalised by the equations which are the limit pressure P_L and axial tension F_A for the thin wall straight pipe as given from:

$$P_L = \frac{2}{\sqrt{3}} (2\sigma_y t / D_m) \quad (4.3)$$

$$F_A = P_L D_m / 4t \quad (4.4)$$

For the cyclic thermal loading, thermal gradient through the wall thickness of the pipe bends are created with a temperature of 550°C at the inside surface and 20°C at the outside surface, so that it implements the most severe thermal loading condition during “start-up”. A reference temperature $\Delta\theta_0 = 550^{\circ}\text{C}$ normalises the thermal loading. It is worth to mention that the thin-walled straight pipe has the normalised values of 1.0 by Eq.(4.2), Eq.(4.3), and Eq.(4.4).

Figure 4.3 (a) illustrates loading paths between the cyclic bending and the constant pressure and between the cyclic thermal loading and the constant pressure that follow the classic Bree problem. Figure 4.3 (b) depicts a cuboid loading domain for the three load combinations (bending, thermal, and pressure). A three-dimensional shakedown boundary of the pipe bends considering the cuboid loading domain will be presented in Section 4.5.

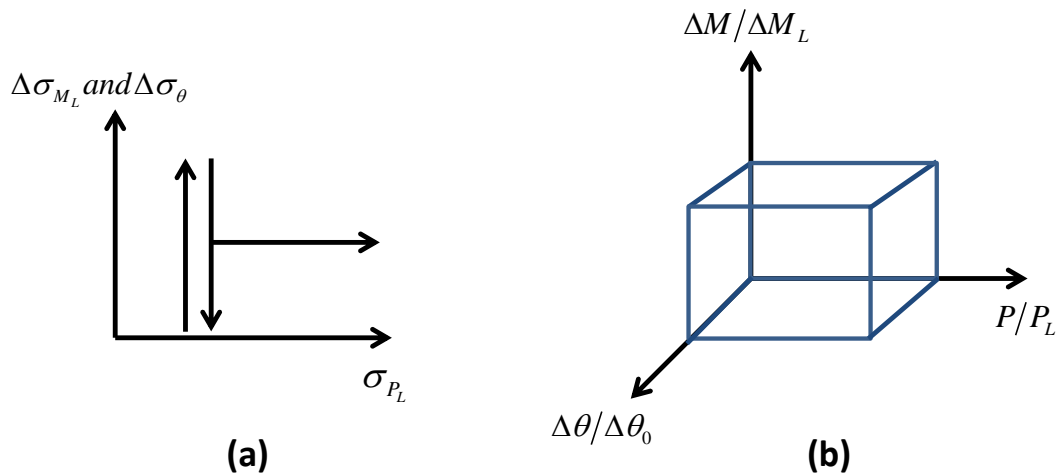


Figure 4.3 (a) loading paths for the classic Bree problem and (b) a loading domain for the three load combinations.

4.3 Cyclic In-Plane Bending and Constant Internal Pressures

4.3.1 Limit load, shakedown limit, and ratchet limit boundaries

Figure 4.4 depicts two linear elastic solutions for the 90° back-to-back pipe structure which is subjected to the cyclic bending moments and the constant internal pressures. The in-plane bending causes the maximum equivalent stress at the flank of the right side pipe bend due to the clockwise moment. The internal pressure causes the maximum equivalent stress at the flank of the left side pipe bend due to the axial tension creating the anticlockwise moment.

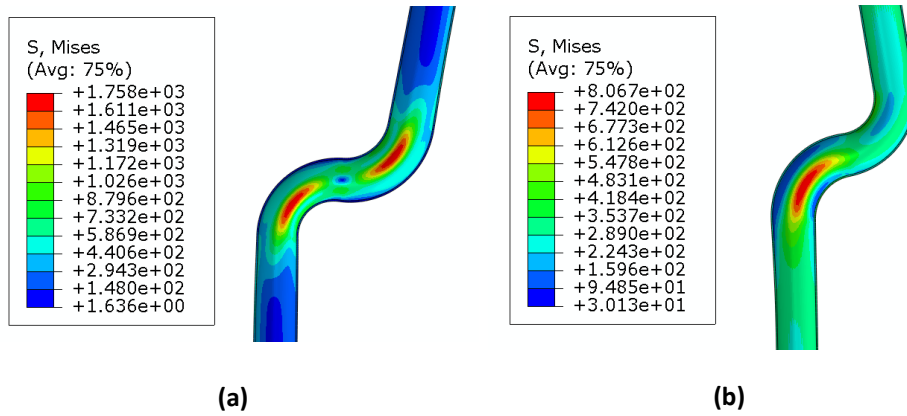


Figure 4.4 Equivalent stress contours from linear elastic stress analyses for a) in-plane opening bending moment M_L b) internal pressures P_L .

Figure 4.5 illustrates the limit load, shakedown, and ratchet limit interaction curves for the 90° back-to-back pipe model under the cyclic in-plane bending moment and the constant internal pressures produced by the LMM. Comparing to the normalised value of the thin-walled straight pipe, the endurance capability of the pipe bends decreases to 47% and 76%, respectively.

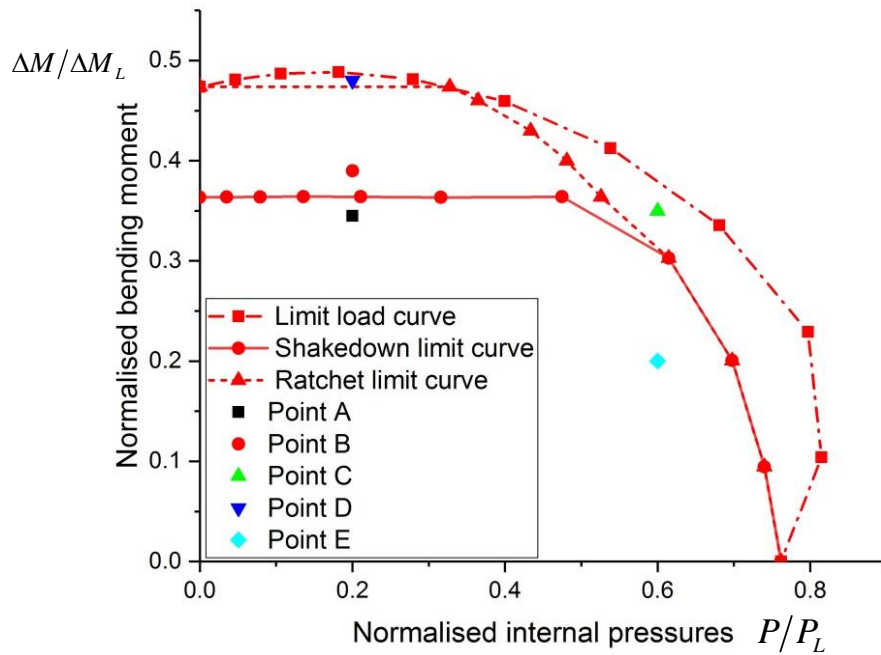


Figure 4.5 The limit, shakedown limit, and ratchet limit boundaries of the pipe bends structure under cyclic in-plane opening bending and constant internal pressures.

The cyclic in-plane bending makes severe impacts on the structural integrity of the pipe bend structure. Interestingly, some points on the limit load boundary show that normalised values are larger than a normalised limit moment at the zero pressure and limit pressures at the zero moment. It is explained that the clockwise bending moments are offset by the axial tension that induced the anticlockwise moment under the combined bending and pressure loadings.

The shakedown boundary has a similar form to Bree diagram with the constant reverse plasticity continuing till $P / P_L = 0.47$. The normalized shakedown boundary at zero pressure is known as the reverse plasticity limit where plastic strains develop overloading cycle but remains a fixed range, also known as “alternating plasticity”. The area between the shakedown and ratchet boundaries is called the reversed plasticity zone where it will cause the alternating plasticity mechanism to occur. If the pipe bend structure is subjected to any load level placed in the reverse plasticity zone, low cycle fatigue damage assessment should be performed to ensure pipeline integrity.

The ratchet boundary has a different shape from the typical Bree diagram as the cyclic moment at zero pressures is intersected with the y-axis. This is because that the applied cyclic load is not the cyclic thermal load. The ratchet boundary has a similar form to the shakedown boundary as keeping horizontal ratchet limit till $P / P_L = 0.33$. Afterwards, it converges to the shakedown boundary where $P / P_L = 0.61$. The area between the ratchet boundary and the limit load boundary is called the ratchetting zone. The limit, shakedown, and ratchet boundaries at the zero moments are converged to a normalised pressure value which is called the limit pressure. If any loading point beyond the limit pressure, the plastic collapse will occur immediately.

4.3.2 Verification of results

The full incremental cyclic plastic analyses are performed for five cyclic loading points (labelled A, B, C, D, and E in Figure 4.5) in order to verify the accuracy of the shakedown and ratchet boundaries obtained. Chen *et al.* [73] proved the accuracy and reliability of results computed by the LMM by showing an error rate of less than 1% from the Abaqus Riks analysis. Therefore, the accuracy of the limit load boundary is not examined within this verification work.

Figure 4.6 depicts the plastic strain increment history using Plastic Strain Magnitude (PEMAG) over the number of loading instances for the cyclic loading points A, B, C, D, and E. The PEMAG considers sign of plastic strain in evolution, giving correct total plastic strain accumulation rather than Equivalent Plastic Strain (PEEQ). The plastic strain history of the five points is referred to the maximum PEMAG value among the eight Gaussian integration points.

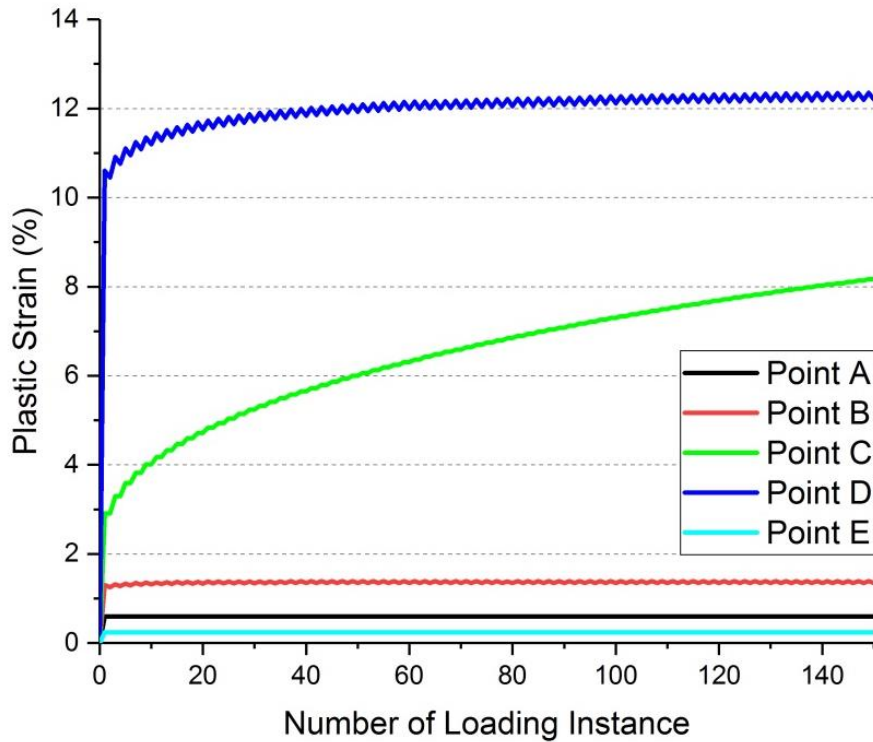


Figure 4.6 Plastic strain increment history (PEMAG) over number of loading instance for cyclic loading points (A, B, C, D, and E).

The point A and E clearly show the elastic shakedown response and the point B shows the reverse plasticity response. Both points C and D display the ratchetting response with the plastic strain accumulating up with every loading cycle. Point C presents a distinguishable increment of the plastic strain thorough the whole number of cycle, whereas the point D appears a small plastic strain increment with every cycle. Due to the small ratchetting zone, point D exhibits insignificant ratchetting response. However, the plastic strain increment in early cycles exceeds 10% and keeps increasing with the small plastic strain increment. Hence the structural response of point D can be taken into account as the ratchetting mechanism.

4.3.3 Parametric studies and discussions

Figure 4.7 illustrates different geometries of the pipe bend structure used for the parametric studies. The r/t ratio is fixed in order to evaluate the effects of R/r ratio on the cyclic plasticity behaviour. Another geometry effect is considered for investigating the cyclic plasticity behaviour with variations of the horizontal straight pipe length L_m against the fixed r/t ratio. With the same equations from (4.2) to (4.4), the cyclic bending and constant pressures for each r/t ratio are normalised. The reference loads are summarised in Table 4.3.

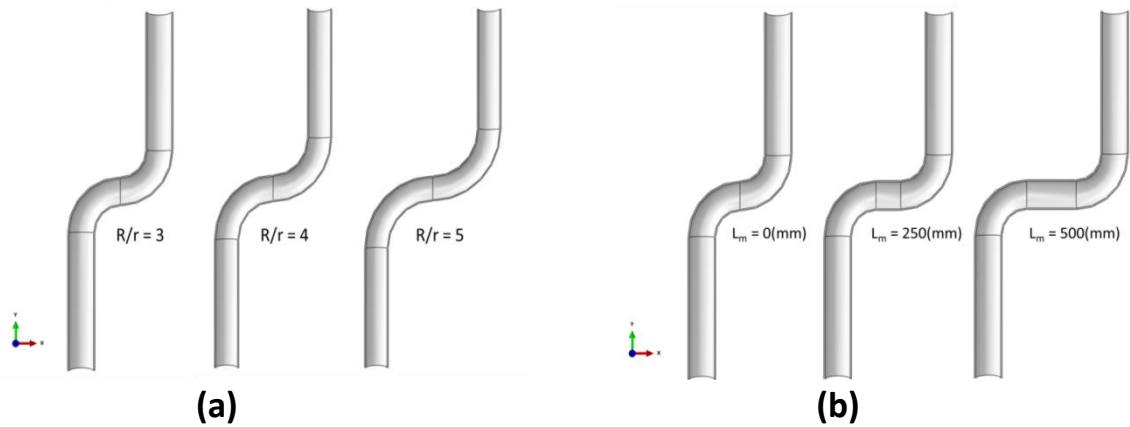


Figure 4.7. Geometries of the pipe bends structure for the parametric studies; (a) fixed $r/t=10$ with varying R/r ratio and (b) fixed $r/t=10$ with varying length L_m .

Table 4.3. Reference loads of cyclic bending moment and constant internal pressure and axial pressure with respect to r/t ratio.

r/t	$M_L [Nmm]$	$P_I [MPa]$	$F_A [MPa]$
5	4.99E+08	62.54	156.36
10	2.50E+08	31.27	156.36
20	1.25E+08	15.64	156.36

4.3.3.1 Geometry effects of the pipe bends structure

Figure 4.8 shows the limit, shakedown limit and ratchet limit boundaries with variations of R/r ratios of 3, 4, and 5 against fixed r/t ratios of 5, 10 and 20. The other geometries such as the mean diameter of the pipe D_m and the length of the vertical straight pipe L are the same as the dimensions in Table 4.1.

As general trends from results obtained, the reverse plasticity limit tends to decrease with an increase of r/t ratio, whereas limit pressure increases. As R/r ratio increase, the reverse plasticity limit increases, but the limit pressure decreases. It is noteworthy that the variation of the ratchet limit boundary of the back-to-back pipe bends is different from a single pipe bend.

For thick-walled pipe bends ($r/t = 5$) in Figure 4.8 (a), the shakedown boundaries for the lower pressures ($P/P_L < 0.3$) have a different shape from the Bree diagram. Moreover, the shakedown boundaries are very close to the limit load boundaries for the lower pressures. Thus the ratchet boundary should be considered as the shakedown boundary. The margins, reverse plasticity zone, between the limit load and shakedown boundaries begin to appear after the lower pressures. Due to the small margin for the lower pressures, allowable load level should be selected conservatively from far below the shakedown boundaries. It is noteworthy that the pipe bend structures with larger R/r ratio have constant limit pressures for $\Delta M / \Delta M_L < 0.75$. Unlike the shakedown boundaries of a single 90° pipe bend structure in [73], the 90° back-to-back pipe bend structure has lower endurance against limit pressures with an increase of R/r . Thus this observation requires consideration when designing a piping network with the double pipe bends.

Shakedown boundaries of thin-walled pipe bends in Figure 4.8 (b) and Figure 4.8 (c) have a similar shape with the Bree diagram. As R/r ratio increase, reverse plasticity limit increases but limit pressure decreases. The margins between shakedown and limit boundaries tend to increase as R/r ratio decreases but increases as r/t ratio increases. For $r/t = 10$, ratchet boundary at $R/r = 5$ should be considered as the shakedown boundary at the same R/r ratio. As R/r ratio decrease, the margins are clearly observed under the ratchet boundary. For $r/t = 20$, ratchet boundaries are noticeable at every R/r ratio.

The shakedown boundaries constructed show that the double pipe bends with $r/t = 10$ are an appropriate design for the operational load levels where normalised cyclic bending and constant pressures are lower than 0.5. The pipe bends with $r/t = 20$ would be appropriate solutions for higher internal pressure to be expected due to lower endurance against cyclic bending.

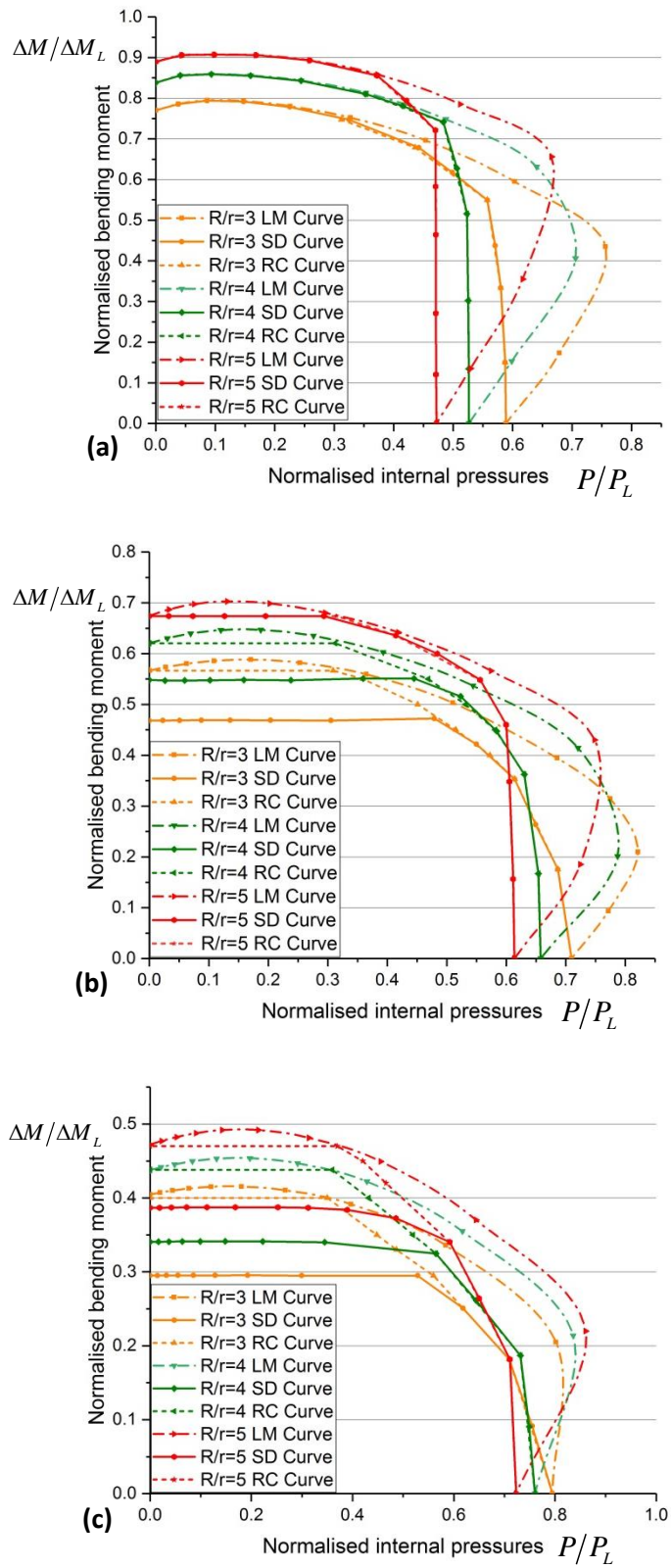


Figure 4.8 The effects of varying R/r with (a) $r/t=5$, (b) $r/t=10$, and (c) $r/t=20$ on the limit load, shakedown limit and ratchet limit boundaries.

Quadratic relationships between the reverse plasticity limit and the bend characteristic for the single 90° pipe bend structure subjected to cyclic in-plane bending and constant internal pressures were derived by Chen *et al.* [73]. The same approach is made to find correlations of the reverse plasticity limit under cyclic in-plane bending RP_{IP} and the limit pressure LP against the bend characteristic h for the 90° back-to-back pipe structure. Figure 4.9 shows trends of the quadratic relationships. Two semi-empirical equations are derived from the relationships, defined by Eqs. (4.5) and (4.6):

$$RP_{IP} = -0.784h^2 + 1.6242h + 0.0492 \quad (4.5)$$

$$LP = 0.2247h^2 - 0.6233h + 0.8751 \quad (4.6)$$

Utilising these derived equations, it helps the pipeline designers predict approximated shakedown boundary of the pipe bend structure with the bend characteristic in a range from 0 to 1 without performing the FEA.

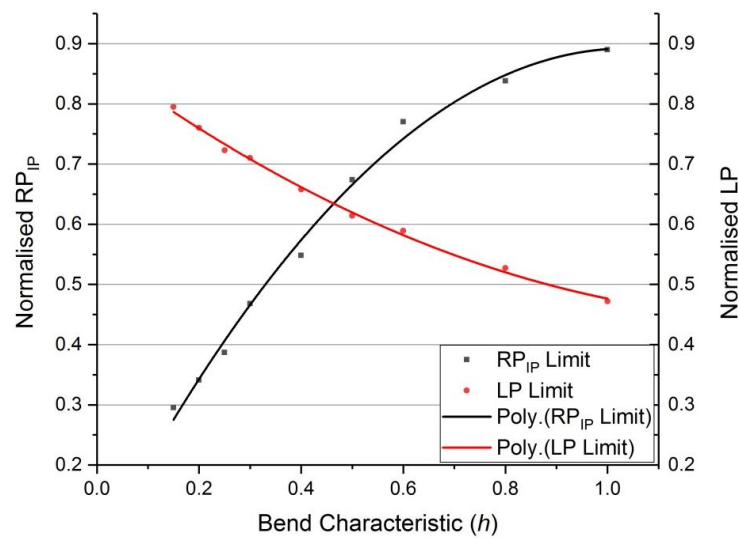


Figure 4.9. Reverse plasticity limit and limit pressure trends with respect to bend characteristic in a range from $h = 0$ to $h = 1$.

From these studies, it can be deduced that the thick-walled pipe bends with a larger R/r ratio is a suitable design for the piping system operated under a high level of cyclic in-plane bending moment and lower constant pressures. It is also found that the reverse plasticity limit and the limit pressure have quadratic relationships against the bend characteristic, which can be expressed by the two 2nd order polynomial equations.

4.3.3.2 Effect of the horizontal straight pipe length

Figure 4.10 illustrates the shakedown, ratchet, and limit load boundaries of the 90° back-to-back pipe bend structure under the cyclic in-plane bending and constant internal pressures with varying horizontal pipe length L_m of 0, 250, and 500 mm against the fixed r/t ratio of 5, 10, and 20. The other geometries such as the bending radius R , mean diameter D_m , and vertical pipe length L are identical to the dimensions in Table 4.1. As general trends observed from investigation results, with an increase of r/t ratio the reverse plasticity limit decreases whereas the limit pressure increases. The longer pipe length L_m is vulnerable to the constant internal pressures rather than cyclic in-plane bending.

The thick-walled pipe bend ($r/t = 5$) shows a more or less the same reverse plasticity limit as the limit moment, regardless of the horizontal pipe length L_m . However, the limit pressure decreases with an increase of the length L_m . Results show that minimal margins are observed between the shakedown and limit load boundaries for the lower pressures ($P/P_y < 0.3$). Thus the ratchet boundary should be considered as the shakedown boundary. Due to the small margin, allowable load level should be limited to far below the shakedown boundary in the case of the low pressures applied.

The thin-walled pipe bends ($r/t = 10$ and $r/t = 20$) show a similar trend in the shakedown, ratchet and limit load boundaries. The thin-walled pipe bends without the horizontal pipe exhibit larger limit load boundary than others with the horizontal pipe. The interesting point is that the horizontal pipe sections have only impacts on the limit pressure but neither on the reverse plasticity limit nor the limit moment. This is because that the anticlockwise bending caused by the axial tension makes significant influences to the left side pipe bend. The limit pressure decreases with an increase of the length L_m , resulting in that ratchet boundaries increases as the length L_m decreases.

These studies provide understandings of the horizontal pipe section between the pipe bends which have significant effects on the limit pressures but minor effects on the cyclic moment. Thus effects of limit pressure level should be a consideration when designing a pipe network with double pipe bends combining with the horizontal pipe section.

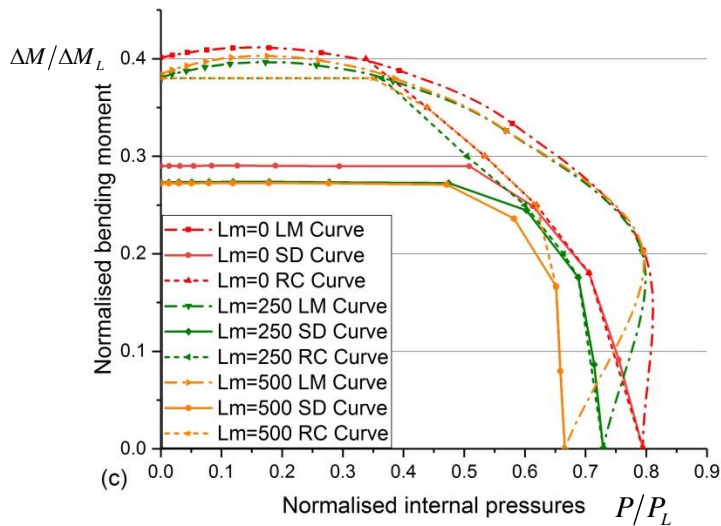
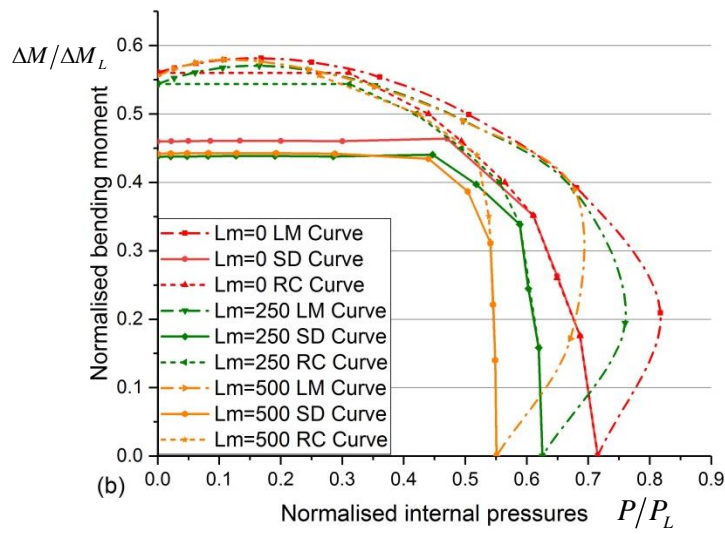
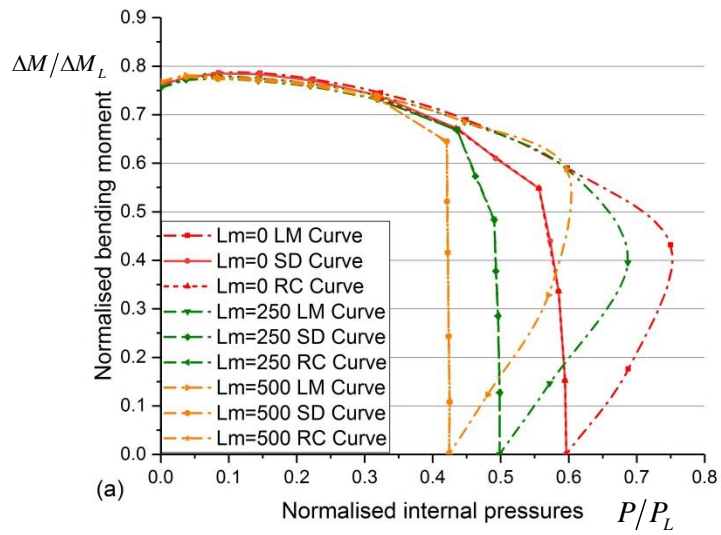


Figure 4.10 The effects of varying length L_m with (a) $r/t=5$, (b) $r/t=10$, and (c) $r/t=20$ under the cyclic in-plane bending and constant internal pressures.

4.4 Cyclic Out-of-Plane Bending and Constant Internal Pressures

4.4.1 Limit load, shakedown limit and ratchet limit boundaries

Figure 4.11 shows two linear elastic solutions for the 90° back-to-back pipe structure subjected to the cyclic out-of-plane bending and the constant internal pressures. The out-of-plane bending moment causes the maximum equivalent stress at the front-inside flank of the left side pipe bend due to the clockwise overturning moment. With the consideration of the symmetry of the pipe geometry in the x-y plane, it is expected that the maximum stress level would occur at the opposite locations if the anticlockwise moment were applied. For the internal pressures only, the maximum equivalent stress develops at the rear-inside flank of the left side pipe bend as same as Section 4.3.1 due to the corresponding axial tension creating the anticlockwise moment.

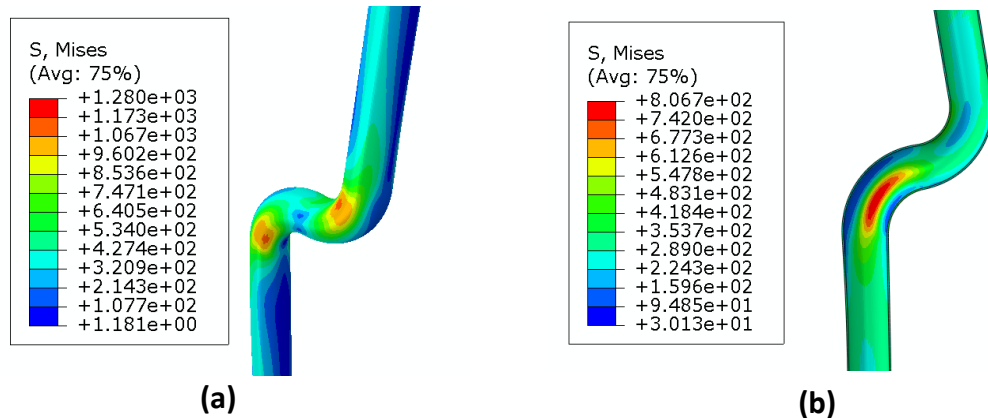


Figure 4.11 Equivalent stress contours from linear elastic stress analyses for (a) out-of-plane bending moment M_L (b) internal pressures P_L .

Figure 4.12 shows the limit load and shakedown boundaries of the 90° back-to-back pipe bends under cyclic out-of-plane bending and constant pressures produced by the LMM. Comparing to the normalised values of the thin-walled straight pipe, the limit moment and limit pressure of the double pipe bends subjected to monotonic out-of-plane bending decreases to 53%, but 6% higher than the pipe bends subjected to monotonic in-plane bending. The out-of-plane bending moment also has severe impacts on the structural integrity of the concerning geometry more than the internal pressures. It is noteworthy that under out-of-plane bending, there is no normalised value more significant than the limit moment at zero pressure and the limit pressures at zero bending moment, unlike the limit load boundary under the in-plane bending and constant internal pressures shown in Figure 4.5. This is because that the out-of-

plane bending is not offset by the anticlockwise moment caused by the axial tension caused by internal pressure.

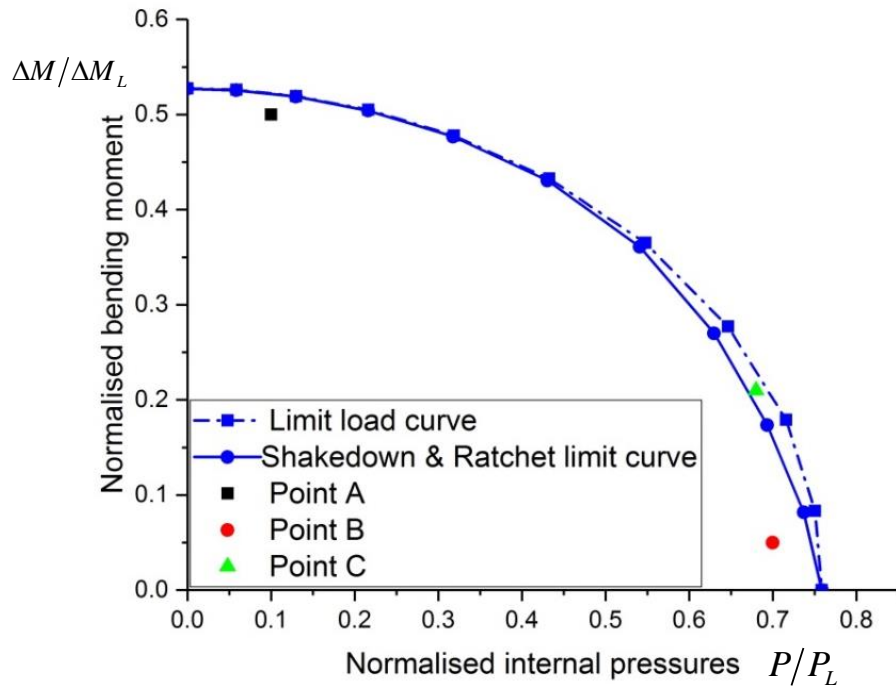


Figure 4.12 The limit, shakedown limit, and ratchet limit boundaries of the pipe bends structure under cyclic out-of-plane opening bending and constant internal pressures.

The interesting point associated with the shakedown boundary under cyclic out-of-plane bending is that the reverse plasticity limit is very close to the normalised limit moment. For the pipe bends under cyclic in-plane bending, the shakedown boundary has a similar form to Bree diagram with enough margins between the shakedown and limit load boundaries. On the contrary, the shakedown boundary under cyclic out-of-plane bending forms very similar shape to resultant limit load boundary with tiny margin where $P/P_L > 0.4$. As results, ratchet boundary for $P/P_L < 0.4$ should be considered as a shakedown boundary. Although there is a small margin for $P/P_L > 0.4$, it is hard to define the ratchet boundary. Upon the case, the whole ratchet boundary requires to be taken into account as the shakedown boundary in a conservative manner.

4.4.2 Verification of results

In order to verify the shakedown and ratchet boundaries constructed, three load points are selected (labelled A, B, C in Figure 4.12), and the full cyclic plastic analysis is performed.

Figure 4.13 shows plastic strain history using Plastic Strain Magnitude (PEMAG) in Abaqus for the points A, B, C against a number of loading steps. The plastic strain history of the three points is referred to the maximum PEMAG value among eight Gaussian integration points. The point A and B demonstrate the elastic shakedown response with no plastic strain increment at the steady cyclic state. The point C shows the ratchetting mechanism with incremental plastic deformation in every cycle.

Due to the small margin between the shakedown and limit load boundaries, corresponding ratchet limit boundary was difficult to be determined, but the plastic strain history at point C confirms that the ratchet limit is very close to the shakedown limit. From these verifications, the structural responses computed are reliable with accuracy.

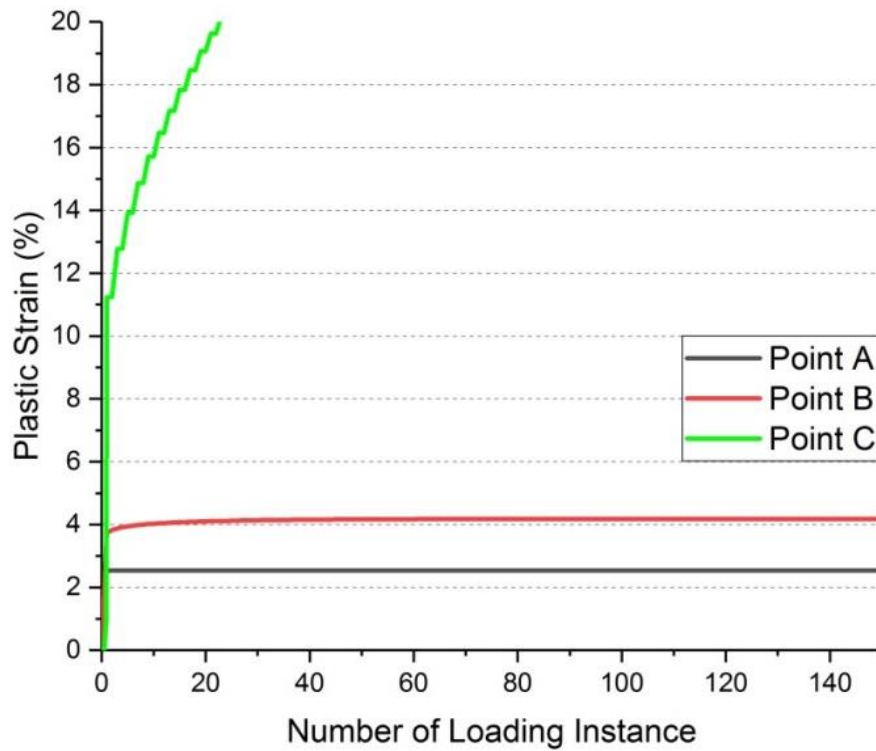


Figure 4.13 Plastic strain increment history (*PEMAG*) of cyclic loading points (A, B, C) in Figure 4.12.

4.4.3 Parametric studies and discussions

The cyclic plasticity behaviours of the same geometry shown in Section 4.3.3 under the cyclic out-of-plane bending and constant internal pressures are investigated. With the same equations from (4.2) to (4.4), the calculated moments and pressures are normalised. The reference loads are summarised in Table 4.3 in Section 4.3.3.

4.4.3.1 Geometry effects of the pipe bends

Figure 4.14 shows shakedown and ratchet boundaries with varying R/r ratios of 3, 4, and 5 against fixed r/t ratios of 5, 10, and 20. The other geometries such as the mean diameter of the pipe D_m and the length of the vertical straight pipe L are the same as the dimensions in Table 4.1. As general features, reverse plasticity limit is very close to the normalised limit moment at zero pressures, which means the changes in geometry seldom affect the reverse plasticity limit under cyclic out-of-plane bending. The reverse plasticity limit tends to increase with a decrease of r/t ratio, whereas the limit pressure decreases. The pipe bends with larger R/r ratio can withstand a higher cyclic bending moment, but the endurance capacity against the internal pressure decreases.

For the thick-walled pipe bends ($r/t = 5$), shakedown boundaries for $P/P_L < 0.3$ are equal to corresponding limit load boundaries. The margins between the shakedown and limit load boundaries begin to form where $P/P_L > 0.3$ but they are small. Although the margins tend to become larger with an increase in R/r ratio, it is still hard to construct the ratchet boundary. Hence it is recommended that the ratchet boundary should be considered as the shakedown boundary. The thick-walled pipe has higher resistance to cyclic out-of-plane bending rather than the internal pressures. As R/r ratio increases, the endurance limits against cyclic out-of-plane bending and constant internal pressures increase for $P/P_L < 0.3$, but decreases for $P/P_L > 0.3$. Compared to the cyclic plasticity under cyclic in-plane bending in Section 4.3.3.1, cyclic out-of-plane bending has larger elastic shakedown boundary but smaller alternating plasticity zone. Therefore, the thick-walled pipe bends are a suitable design for a piping network operated under a high level of cyclic out-of-plane bending moments.

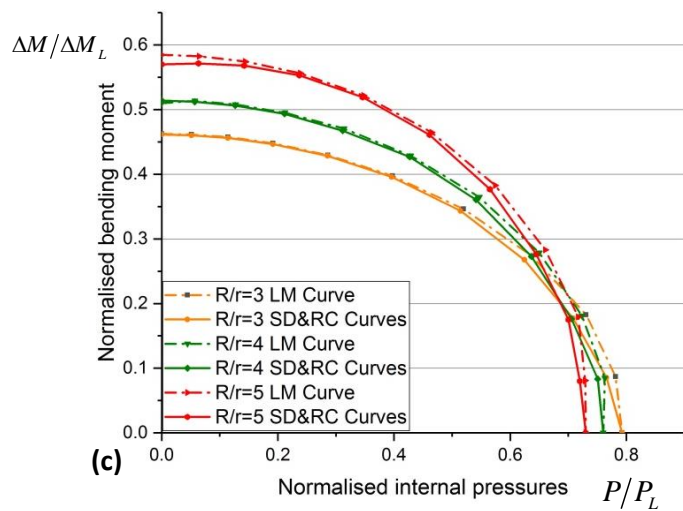
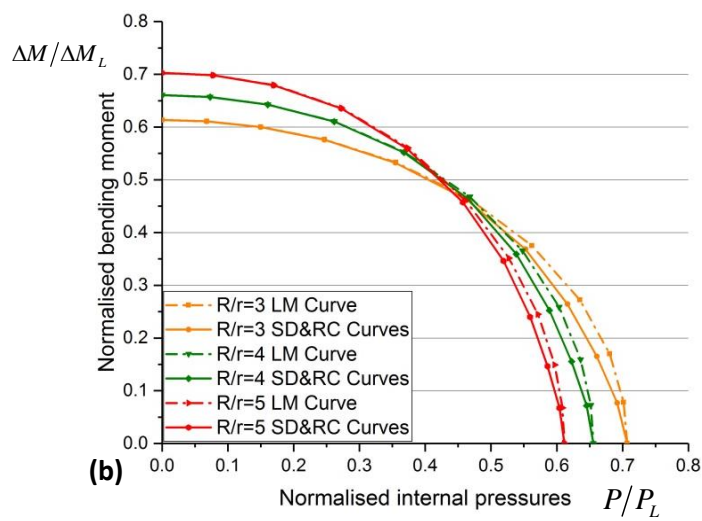
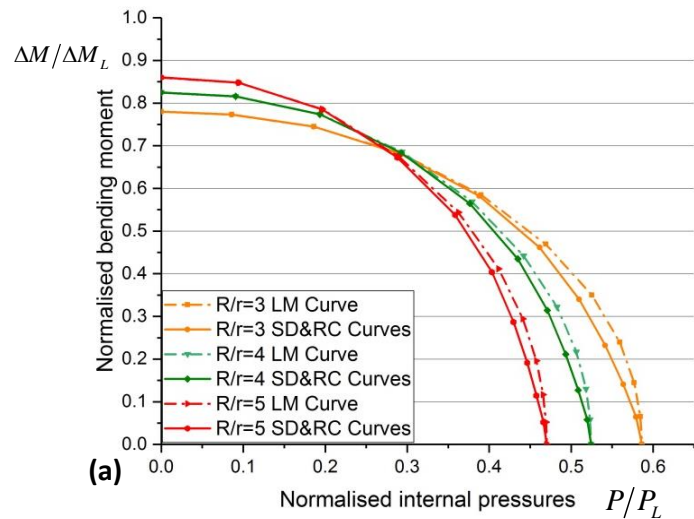


Figure 4.14 Effect of varying R/r with (a) $r/t=5$, (b) $r/t=10$, and (c) $r/t=20$ under the cyclic out-of-plane bending and constant internal pressures.

For the thin-walled pipe bends ($r/t = 10$ and $r/t = 20$) shakedown boundaries have a similar form to their limit load boundaries. The margin is too narrow to construct the ratchet boundary for each R/r ratio so that the ratchet boundary should be considered as the shakedown boundary. As r/t ratio increases, normalised values in out-of-plane bending moment increase, but normalised values in the pressures decrease.

For $r/t = 10$, as R/r ratio increases, shakedown and limit load boundaries increase where $P/P_L < 0.45$, but decreases for $P/P_L > 0.45$. For $r/t = 20$, the larger R/r ratio has more substantial shakedown and limit load boundaries for $P/P_L < 0.68$, whereas they become small for $P/P_L > 0.68$. Reverse plasticity limits for $r/t = 20$ under cyclic out-of-plane bending are higher than cyclic in-plane bending, which means the pipe structure can withstand a high level of cyclic bending moments in the out-of-plane direction than the in-plane.

The correlations of reverse plasticity limit RP_{IP} and limit pressures LP against the bend characteristic h for the pipe bends subjected to the cyclic in-plane bending and constant internal pressures were derived by two quadratic relationships as equations (4.5) and (4.6). For the identical pipe bends subjected to the cyclic out-of-plane bending and constant internal pressures, relations of reverse plasticity limit RP_{OP} and the bend characteristic h are derived by adopting the Quadratic Regression method as given Eq.(4.7). Due to equivalent constant loading applied to the pipe bends, the limit pressures under the out-of-plane bending is identical to Eq.(4.6).

$$RP_{OP} = -0.5032h^2 + 1.0227h + 0.3367 \quad (4.7)$$

There is another relationship to be derived between a ratio ($RT = RP_{OP}/RP_{IP}$) and the bend characteristic. Trends for the newly derived equations are illustrated in Figure 4.15, and R-squared value of the all equations from (4.5) to (4.8) are higher than 0.98.

$$RT = 1.4312h^2 - 2.3624h + 1.9154 \quad (4.8)$$

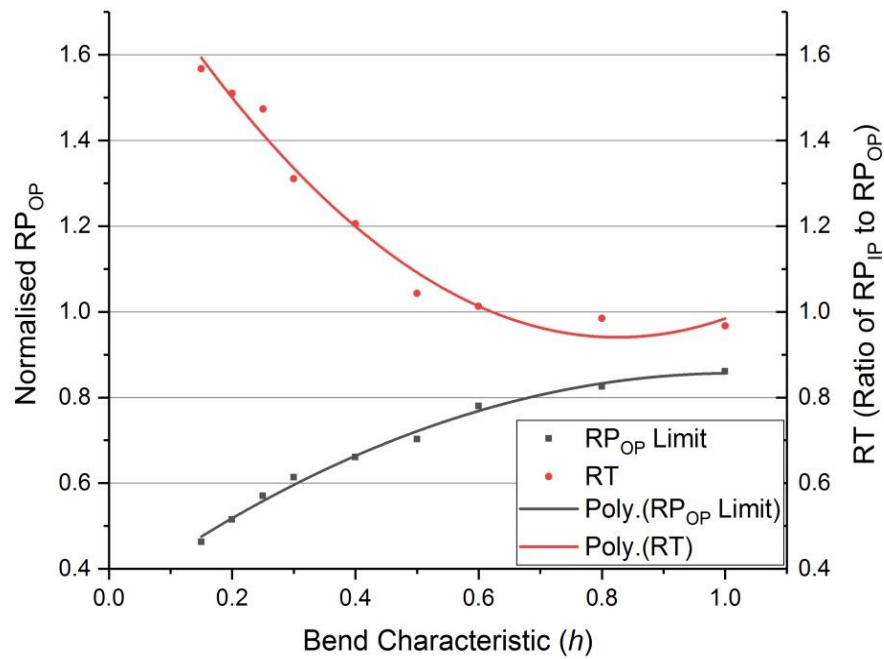


Figure 4.15 Reverse plasticity limit and trends of the ratio $RT = RP_{OP} / RP_{IP}$ against the bend characteristic in a range from $h = 0$ to $h = 1$.

4.4.3.2 Effects of the horizontal straight pipe length

Figure 4.16 illustrates shakedown and ratchet boundaries of the pipe bend structure subjected to the cyclic out-of-plane bending and constant internal pressure with changing horizontal pipe length L_m of 0, 250, 500 mm against the fixed r/t ratios of 5, 10, and 20. The other geometries such as the mean diameter D_m and vertical pipe length L are the same dimensions as Table 4.1.

The general trends for each type of geometry are that reverse plasticity limit decreases, but limit pressures increase as the length L_m decrease. However, the variation in the reverse plasticity limit is minimal. The reverse plasticity limits are very close to their corresponding limit moments at zero pressure, which means changes of the horizontal length have no effects on the size of the alternating plasticity zone which is referred to the margin. Due to small margins between shakedown and limit load boundaries, ratchet boundary should be considered as a shakedown boundary. Contrary to the effects of the horizontal pipe length under cyclic in-plane bending in Section 4.3.3.2, the horizontal pipe length under cyclic out-of-plane bending has minor effects on the reverse plasticity limit but significant impacts on the limit pressures.

For the thick-walled pipe bends ($r/t = 5$), regardless of the length of L_m , the reverse plasticity limit and the normalised limit moment at zero pressures are identical to 0.79. However, limit pressures decrease with increasing of the length L_m . The margins between the shakedown and limit load boundaries appear where $P/P_y > 0.2$, but very small. Hence corresponding ratchet boundary should be assumed as own shakedown boundary. When it comes to the endurance capability, the thick-walled pipe structure has larger normalised moment values than normalised pressure values regardless of the horizontal pipe length. Thus the thick-walled pipe bends are an appropriate solution for a high level of cyclic bending moment expected during operations.

For the thin-walled pipe bends ($r/t = 10$ and $r/t = 20$) reverse plasticity limits and normalised limit moment values at zero pressures are nearly equal. The maximum change in the reverse plasticity limit between each horizontal length is 0.1. The limit pressure decreases as the length L_m increases. The margins of $r/t = 10$ and $r/t = 20$ appears at where $P/P_y > 0.26$ and $P/P_y > 0.39$, respectively, but still too narrow to construct the ratchet limit boundaries.

Compared to the structural response under cyclic in-plane bending, the pipe structures of $r/t = 10$ and $r/t = 20$ under cyclic out-of-plane bending have a higher bending resistance of 15% and 20% respectively. It observed that changes in the horizontal straight pipe length make less impact on the reverse plasticity limit but effective on internal pressures. In particular, the pipe structure of $r/t = 5$ with $L_m = 500mm$ has over 20% pressure reduction from the pipe structure without the horizontal pipe. Therefore, the horizontal pipe length should be designed as short as possible if thick walled pipe bends subjected to high internal pressure operation.

Compared to the structural response under cyclic in-plane bending, the pipe structures of $r/t = 10$ and $r/t = 20$ under cyclic out-of-plane bending have a higher bending resistance of 15% and 20% respectively. It observed that changes in the horizontal straight pipe length make less impact on the reverse plasticity limit but effective on internal pressures. In particular, the pipe structure of $r/t = 5$ with $L_m = 500mm$ has over 20% pressure reduction from the pipe structure without the horizontal pipe. Therefore, the horizontal pipe length should be designed as short as possible if thick walled pipe bends subjected to high internal pressure operation.

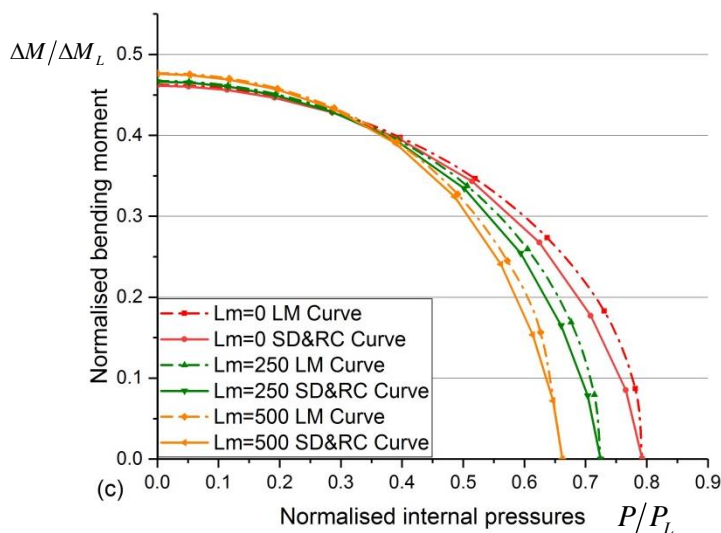
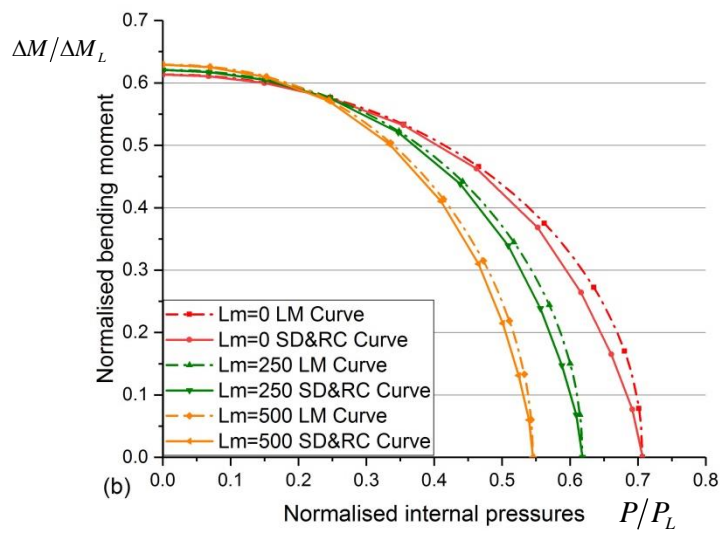
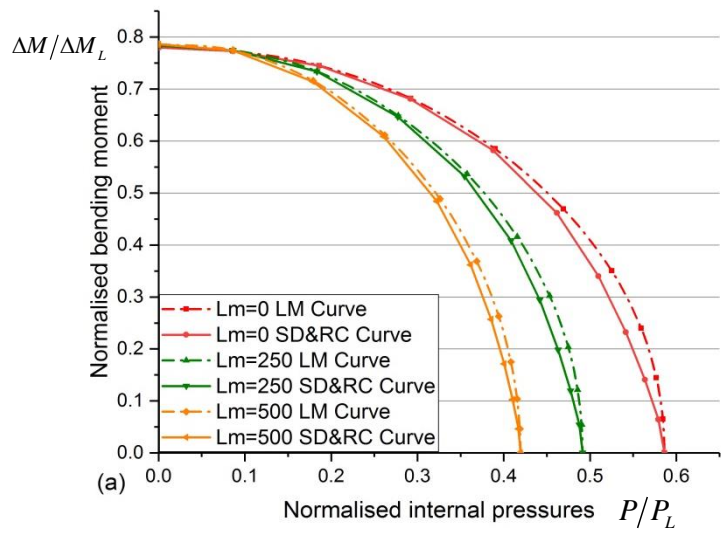


Figure 4.16 Effect of varying length L_m with (a) $r/t=5$, (b) $r/t=10$, and (c) $r/t=20$ under the cyclic out-of-plane bending and constant internal pressures.

These studies show the effects of the horizontal pipe length on the integrity of the pipe structure, which has significant impacts on the constant pressures but minor effects on the cyclic bending. Due to the small margins, plastic collapse can occur if operational loading beyond the elastic shakedown boundary.

4.5 Cyclic Thermal Loading, Cyclic Out-of-Plane Bending and Constant Internal Pressures

It is critical to consider two temperature fields that have the effects of cyclic thermal loads on the pipe structure integrity assessment: a non-isothermal condition for the start-up and shut down, and an isothermal condition for the regular operation. In order to investigate the effects of the temperature fields on the integrity of the same pipe bends, the shakedown and ratchet analyses are performed for cyclic thermo-mechanical loading consisting of cyclic thermal load, cyclic out-of-plane bending, and constant pressure. The isothermal temperature field does not create any significant thermal stress over the pipe bends. Therefore, the non-isothermal condition is only considered in this study. The temperature dependent yield stress shown in Table 4.2 is used. The same equations from (4.2) to (4.4) normalise the bending moments and the internal pressures, and a reference temperature $\Delta\theta_0 = 550^\circ C$ is employed to normalise the thermal load. The top side of the pipe bends is constrained as a plane condition so that it can achieve the long pipe effects.

Figure 4.17 depicts three linear elastic solutions of the 90° back-to-back pipe structure subjected to thermal loading, out-of-plane bending and internal pressure. The thermal load produces the maximum tensile stress at the outside of the pipe structure but the compressive stress at the inside due to the non-isothermal effects. The thermal expansion coefficient of the material is a critical factor that leads to these thermal stresses. Elastic analysis solutions of the other two loadings are presented before in Section 4.4.1.

The thermo-mechanical loading is classified into the three combined load cases; **Loading Type A**: cyclic out-of-plane bending and constant internal pressures, **Loading Type B**: cyclic thermal load and cyclic out-of-plane bending, and **Loading Type C**: cyclic thermal load and constant internal pressures. The shakedown and ratchet limit boundaries under the three load types are presented in Figure 4.18 (a). Figure 4.18 (b) illustrates a shakedown limit domain of the pipe structure in a three-dimensional loading space shown in Figure 4.3 (b).

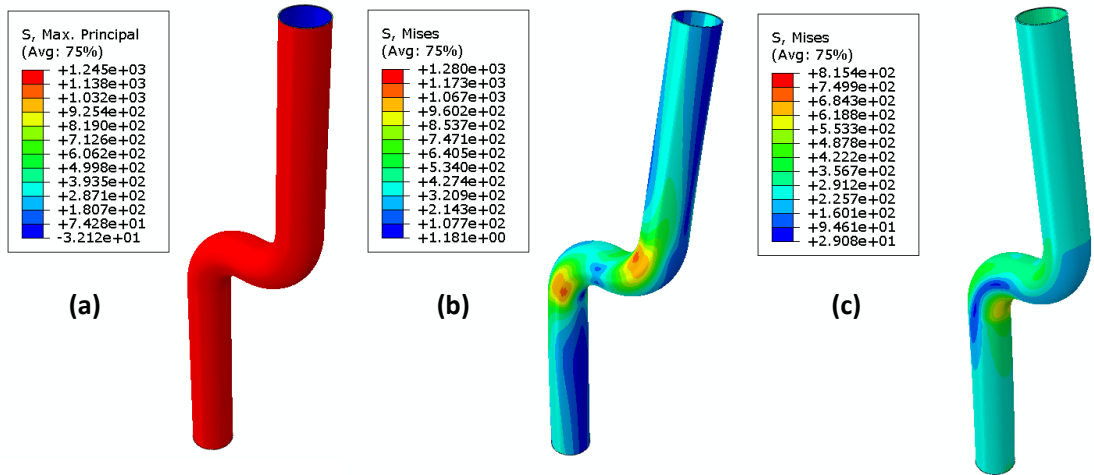


Figure 4.17 Linear elastic solutions; (a) Max. principal stress under thermal load, (b) equivalent stress under out-of-plane bending moment, and (c) equivalent stress under internal pressures.

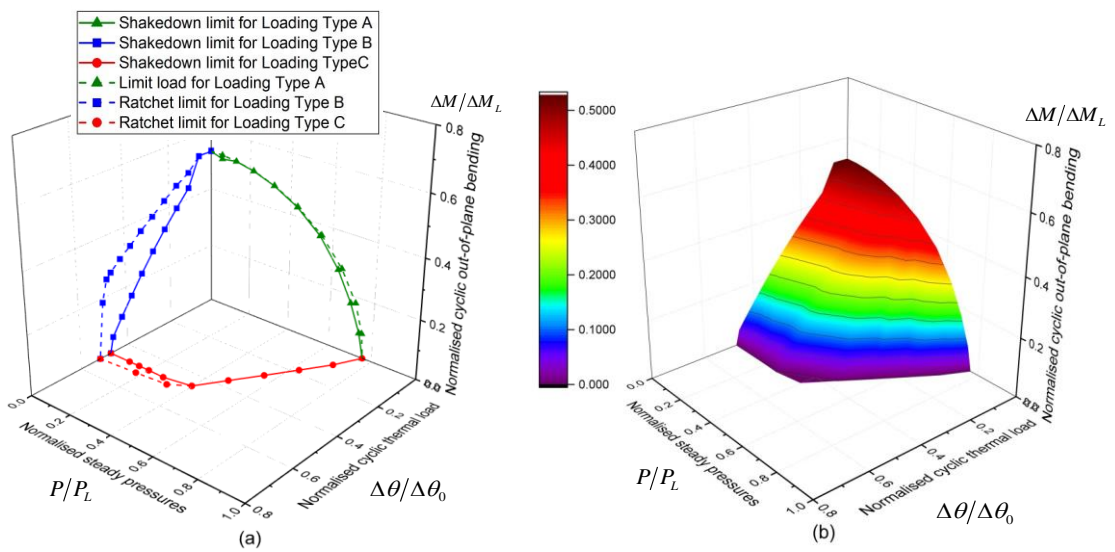


Figure 4.18 (a) Shakedown and ratchet boundaries of the 90° back-to-back pipe bends subjected to cyclic thermal load, cyclic out-of-plane bending and constant internal pressure and (b) shakedown domain in the three-dimensional loading space.

Loading Type A

Analysis results and discussions for the double pipe bends under Loading Type A are described in Section 4.3.1.

Loading Type B

When it comes to the ratchetting boundary, the pipe bend structure can withstand the loading at 53% under cyclic out-of-plane bending and 54% under cyclic thermal load, compared to their reference bending moment and temperature respectively. Regarding the reverse plasticity limit, the normalised value by the cyclic thermal load is almost the same as by the cyclic out-of-plane bending. Hence the effects of cyclic thermal load on the pipeline integrity require serious considerations.

Different from the shape of the shakedown boundary under Loading Type A, Loading Type B develops a shakedown boundary of a triangular shape which merges to the reverse plasticity limit of cyclic out-of-plane bending for $\Delta M / \Delta M_L > 0.5$. Hence, the ratchet limit under Loading Type B should be considered as the shakedown boundary where $\Delta M / \Delta M_L > 0.5$. However, the margin between the shakedown boundary and the ratchet boundary becomes larger as the cyclic thermal load increases up to the reverse plasticity limit of cyclic thermal load, $\Delta \theta / \Delta \theta_0 = 0.54$. It is noteworthy that the thermal ratchetting does not occur in the Bree problem under the pure cyclic thermal load, but it does in the double pipe bend structure where $\Delta \theta / \Delta \theta_0 > 0.54$. Therefore, the allowable load level should be selected from below the shakedown boundary.

Loading Type C

Shakedown boundary under Loading Type C shows very similar shape to the exemplary Bree diagram. Where $P / P_L < 0.3$, the shakedown boundary maintains the constant reverse plasticity limit, and afterwards slightly decreases until $P / P_L = 0.4$. The margin that shows the reverse plasticity response is small due to the thermal ratchetting limit. Therefore, the proper load level should be selected under the shakedown boundary.

4.5.1 Geometry effects of the pipe bends

Figure 4.19 shows a comparison of the shakedown and ratchet boundaries for changing R/r ratio against fixed $r/t = 5$. The shakedown boundaries have a very similar shape to the typical Bree diagram. The results analysed provide interesting observations that the value of the reverse plasticity limit is the same regardless of variations of R/r ratio. The variations of R/r ratios (3, 4 and 5) have minor effects on the thermal stress magnitude of the pipe structure. It demonstrates that the reverse plasticity limit reported in Figure 4.18 (a) is also the same as in Figure 4.19. Chen *et al.* presented the effect of cyclic thermal load on a single elbow bend with the varying R/r ratio, it confirms that reverse plasticity limits are very close to each other [73]. The limit pressures for each R/r ratio are the same as Figure 4.14 (a).

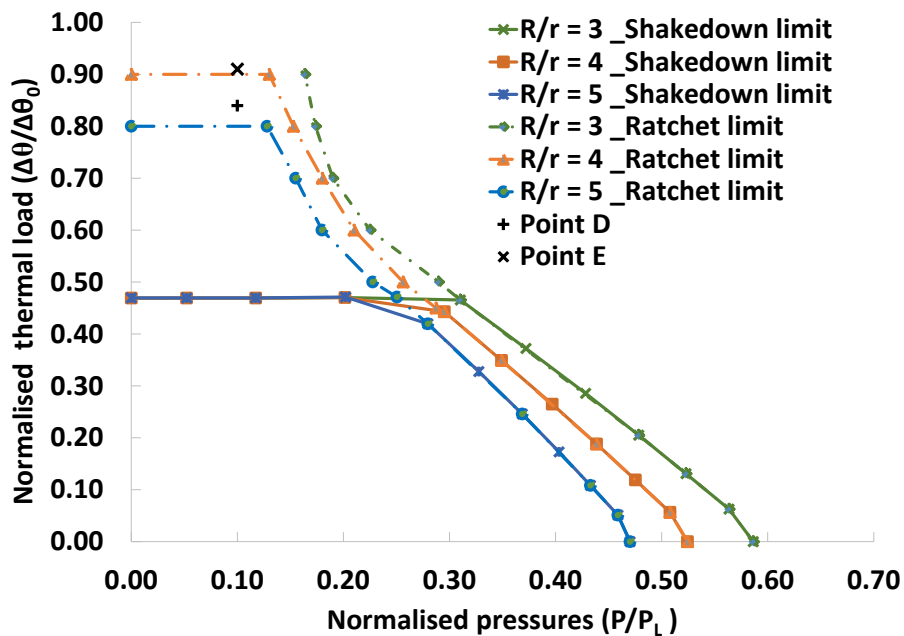


Figure 4.19 Shakedown and ratchet boundary of the pipe bends ($r/t=5$) subjected to cyclic thermal load and constant internal pressure with respect to varying R/r ratio.

Ratchet boundaries of R/r ratio of 4 and 5 have the thermal ratchet limit, thus they have a similar form with a shakedown boundary of the Bree diagram. However, no thermal ratchet limit is observed for $R/r = 3$ below the normalised thermal load of 1.0. Two cyclic loading points D and E are created to validate the ratchet interaction curves, and the full incremental analysis is performed to evaluate the plastic strain increment over a number of load instances. The clear ratchetting response appears in R/r ratio 4 and 5, whereas R/r ratio 3 shows alternating plasticity. Figure 4.19 demonstrates higher temperature field affects pipe bends

with a larger R/r ratio; consequently, plastic shakedown zone becomes smaller as the R/r ratio increases. The cyclic thermal load affects ratchet boundary but merely shakedown boundary for variations of R/r ratio.

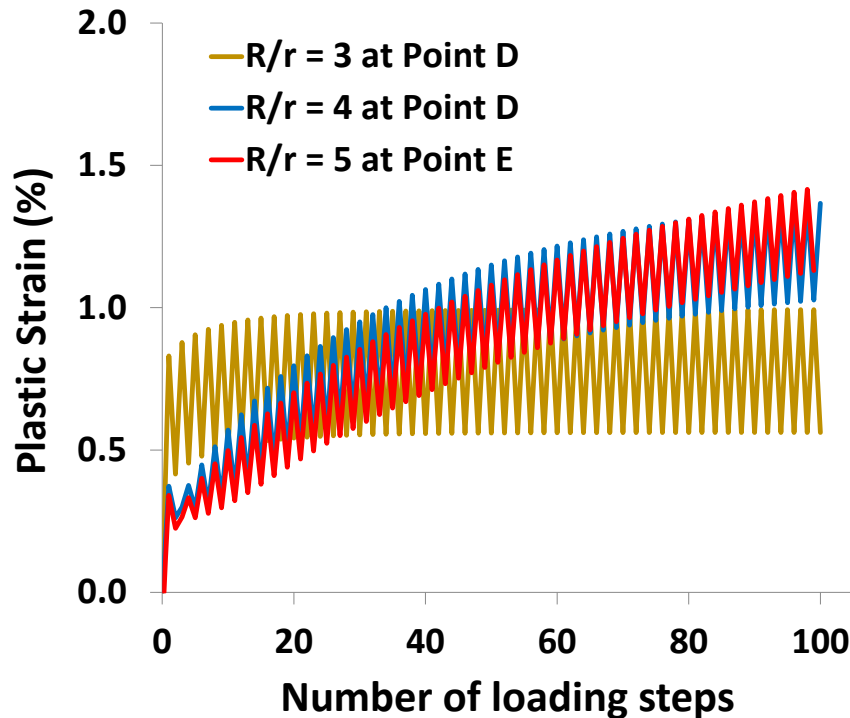


Figure 4.20 Plastic strain history (PEMAG) of R/r ratio of 3 and 4 at cyclic loading point D and of R/r ratio of 5 at cyclic loading point E.

Further study is performed for the same pipe bends subjected to a different combination of the thermo-mechanical load: the cyclic thermal load, constant internal pressure and constant out-of-plane bending. depicts the resulting shakedown boundaries with the varying R/r ratio (3, 4, and 5) against fixed $r/t = 5$.

Although the constant out-of-plane bending moment is applied together with the pressure, the shape of shakedown boundaries is similar to the Bree diagram. The reverse plasticity limits do not change for P/P_L & $M/M_L < 0.2$, regardless of the variation of R/r ratio, but the combined constant pressure and bending moment are reduced to 11%, 7%, and 5% respectively as R/r ratio increases 3, 4, and 5. Therefore, it is deduced that the geometry changes under cyclic thermal load and constant pressure (or combined with the bending moment) have minor effects on the shakedown boundaries but considerable impacts on thermal ratchet limit.

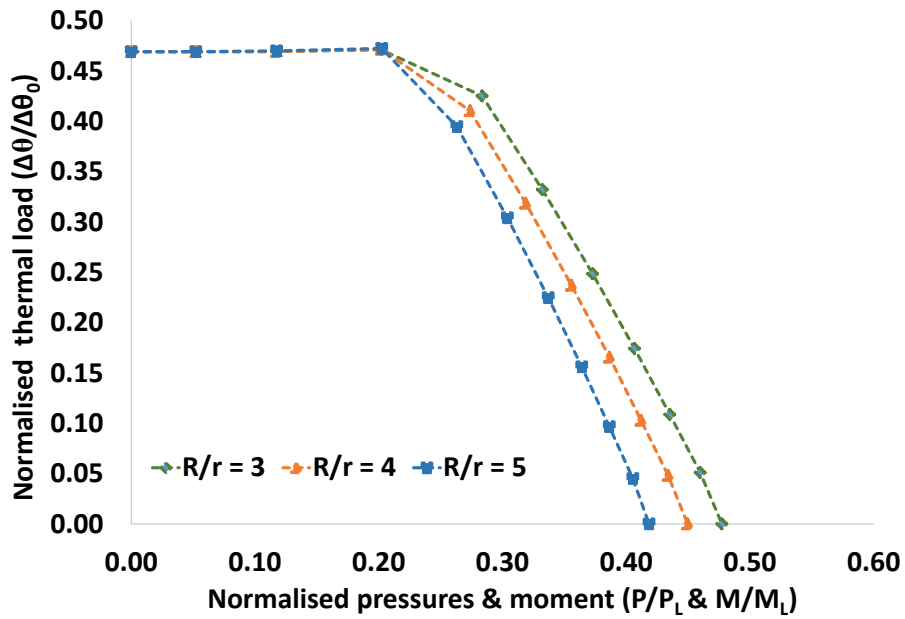


Figure 4.21 Shakedown boundary of the pipe bends ($r/t=5$) subjected to cyclic thermal load and constant internal pressure and bending moment with respect to varying R/r ratio.

4.6 Chapter Summary

The shakedown and ratchet boundaries of 90° back-to-back pipe bends subjected to cyclic thermo-mechanical loading with constant internal pressures were investigated by means of the LMM.

Without thermal load, results showed that cyclic bending makes more impacts on the integrity of the double pipe bends than internal pressures, particularly cyclic in-plane bending affects more than cyclic out-of-plane bending. The cyclic in-plane bending produces shakedown boundary which has a typical shape of Bree diagram, as well as that distinguishable ratchet boundary is constructed within the margin between shakedown and limit load boundaries. The cyclic out-of-plane bending results in shakedown boundary which is almost equal to corresponding limit load boundary, so that ratchet boundary should be considered as the shakedown boundary. The cyclic out-of-plane bending has a larger elastic shakedown boundary than cyclic in-plane bending. However, due to the ratchet boundary, a conservative approach should be taken under cyclic out-of-plane bending when designing the allowable

load level. The horizontal pipe section makes significant impacts on the limit pressures but minimal on the reverse plasticity limits.

With thermal load effects, the pipe bend structure under cyclic thermal load shows almost the same reverse plasticity limit as the structure subjected to cyclic out-of-plane bending. Therefore, the thermal stress effects require serious consideration of the integrity assessment of the pipe bends structure. Moreover, this study demonstrates that geometry changes such as variations of r/t & R/r ratios do not affect reverse plasticity limit of the pipe bends under the cyclic thermal load, whereas they have significant influences on the reverse plasticity limit under the cyclic bending moments.

The parametric studies provided understandings on cyclic plasticity behaviour of the pipe bend structure in associated with geometry effects of the pipe bends under different combinations of the loadings defined. In particular the semi-empirical equations derived in Sections 4.3 and 4.4 can be utilised to predict shakedown limit boundary without performing the complex finite element analysis.

5. Creep-Cyclic Plasticity Behaviours of Metal Matrix Composite

5.1 Introduction

Research on Metal Matrix Composites (MMCs) has been ongoing for more than 50 years to develop stronger, lighter materials, and is now widely used in next-generation aerospace and automotive industries[77]. Discontinuous MMCs (DMMCs) can combine metallic phase (including Al, Mg, Cu, Ti, and Fe) and ceramic reinforcement (including borides, carbides, nitride, oxides, and their mixture). Therefore, DMMCs tend to show higher mechanical properties, durability, and stability than corresponding monolithic matrix material. Although DMMCs have such superior advantages, there are still many things that need improvement: for instance, high temperature damage tolerance, production of a homogeneous discrete distribution of the reinforcement, and high development cost.

For the high temperature application, significant research and efforts have been put in the development of DMMCs and by using titanium alloy matrix discontinuously reinforced titanium matrix composites (DRTMCs) now possess improved high temperature durability including other enhanced mechanical properties in recent years [78]. In particular, titanium matrix composites (TMCs) reinforced with silicon carbide (SiC) continuous fibres have a high potential to exploit in the aerospace and weapon industries [79]. These composites are stronger, more creep and fatigue resistant and have a lower weight to stiffness ratio than conventional metal alloys [80].

Regarding the production of a homogeneous discrete distribution of the reinforcement, despite highlighted advantages of the DRTMCs, further challenges to their damage tolerance and high temperature strength are required [79]. The increasing volume fraction of the reinforcement may enhance the high temperature strength but deteriorate their ductility [78]. On the other hand, arrangements of the reinforcement have significant impacts on that ductility and deformability, but tailoring of the spatial distribution of the reinforcement is very difficult to control to ensure homogeneous particle arrangement in production [81]. As a promising solution, fabricating titanium matrix with powder metallurgy is highlighted to resolve to ensure both high ductility and strength at room temperature and high temperature[82].

Many types of research were carried out for investigating mechanical properties and plasticity of particle reinforced metal matrix composites [83-85]. However, there is no study on creep-

cyclic plasticity behaviour of particle reinforced titanium matrix composites (PRTMCs). As a result, the significance of neither the spatial particle distribution nor the volume fraction on inelastic behaviour of PRTMCs has been reported. Hence, this work focuses on investigating creep-cyclic plasticity behaviours of the PRTMCs against effects of spatial particle distributions, a number of particles, and volume fractions of the reinforcement, with the LMM eDSCA and three-dimensional multi-particles unit cells [86-88].

Section 5.2 shows the microstructure generation of the multi-particle unit cells along with the boundary conditions applied for the numerical investigation. Section 5.3 presents numerical results and discussions for the creep-cyclic plasticity behaviours of the PRTMCs. Effects of spatial particle distributions, variations of dwell time, and volume fractions on the material behaviour are presented using hysteresis stress-strain loops and Tables with summarised data. It discusses comprehensively the effect of critical parameters affecting the cyclic plasticity and creep-cyclic plasticity behaviour of the PRTMCs. Conclusions and remarks of this study are made in Section 5.5.

5.2 Finite Element Model

In order to carry out this numerical investigation, three-dimensional multi-particle unit cells have been employed. The FE models used come from a previous study on the optimization of the spatial particle distribution of MMCs [89] where the Young's modulus along the x-axis has been considered as objective function to derive both its upper bound and lower bound. The RVE (Representative Volume Element) algorithm presented in [89] is used to create periodic unit cells and, periodic boundary conditions are applied to them [90].

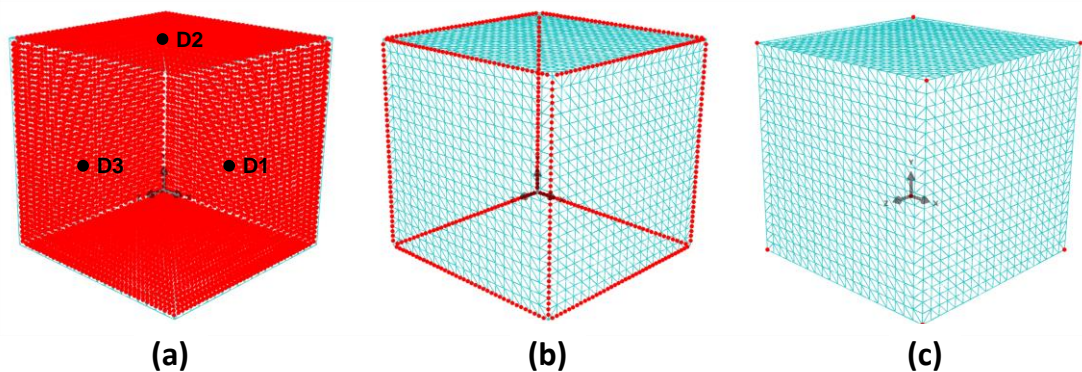


Figure 5.1 Groups of nodes on the boundary faces of the RVEs (a) inner face nodes, (b) inner edge nodes and (c) corner nodes [91].

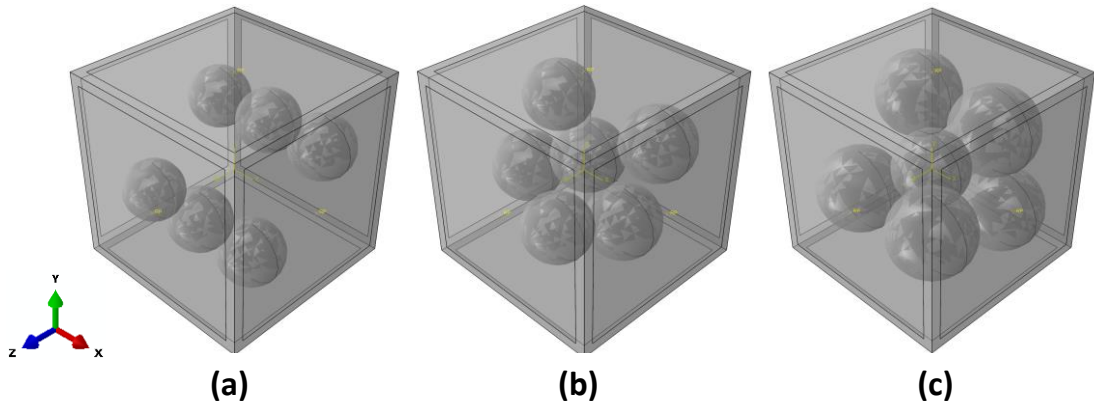


Figure 5.2 Typical FE models with six particles and (a) $V_f = 10\%$, (b) $V_f = 14\%$, (c) $V_f = 25\%$ [91].

Upon defining three node groups on the boundary faces i.e. inner face nodes, inner edge nodes and corner nodes, three systems of equations reported in (6.1), (6.2) and (6.3) are set up, which will be applied between the relative node pairs. Into the aforementioned equations, u_i is the nodal variable at a specific node within a node group related to the degree of freedom i while u_i^{D1} , u_i^{D2} , and u_i^{D3} are the perturbation carried out on the dummy nodes D_1 , D_2 and D_3 and L_{RVE} is the length of the RVE's edge. For this study, the investigation is carried out with the perturbation $u_i^{D1} \neq 0$ and $u_i^{D2} = u_i^{D3} = 0$.

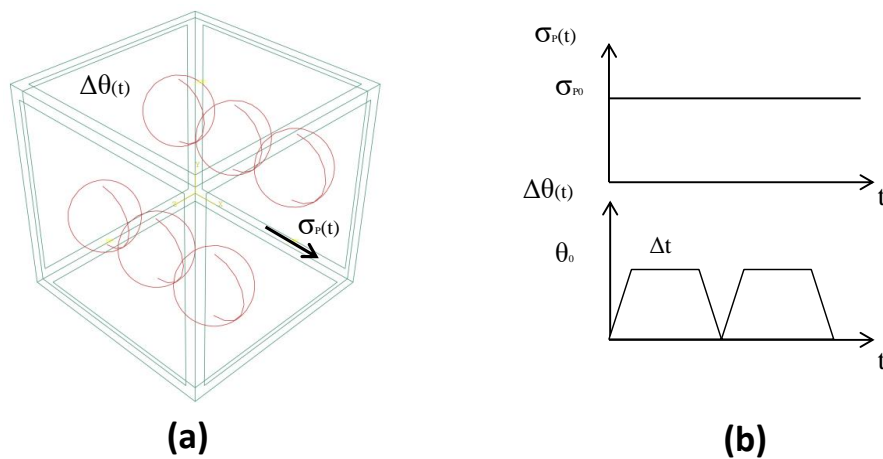


Figure 5.3 (a) RVE with tensile mechanical load $\sigma_p(t)$ and cyclic thermal load $\Delta\theta(t)$ and (b) load history applied [91, 92].

$$\text{Group 1} \left\{ \begin{array}{l} u_i(0, y, z) - u_i(L_{RVE}, y, z) + u_1^{D1} = 0 \\ u_i(x, 0, z) - u_i(x, L_{RVE}, z) + u_2^{D2} = 0 \\ u_i(x, y, 0) - u_i(x, y, L_{RVE}) + u_3^{D3} = 0 \end{array} \right\} \quad \left\{ \begin{array}{l} i = 1, 2, 3 \\ x \in R \mid 0 < x < L_{RVE} \\ y \in R \mid 0 < x < L_{RVE} \\ z \in R \mid 0 < x < L_{RVE} \end{array} \right. \quad (6.1)$$

$$\text{Group 2} \left\{ \begin{array}{l} u_i(0, y, L_{RVE}) - u_i(L_{RVE}, y, L_{RVE}) + u_1^{D1} = 0 \\ u_i(0, y, 0) - u_i(L_{RVE}, y, 0) + u_1^{D1} = 0 \\ u_i(0, L_{RVE}, z) - u_i(L_{RVE}, L_{RVE}, z) + u_1^{D1} = 0 \\ u_i(0, 0, z) - u_i(L_{RVE}, 0, z) + u_1^{D1} = 0 \\ u_i(x, 0, L_{RVE}) - u_i(x, L_{RVE}, L_{RVE}) + u_2^{D2} = 0 \\ u_i(x, 0, 0) - u_i(x, L_{RVE}, 0) + u_2^{D2} = 0 \\ u_i(0, 0, z) - u_i(0, L_{RVE}, z) + u_2^{D2} = 0 \\ u_i(0, y, 0) - u_i(0, y, L_{RVE}) + u_3^{D3} = 0 \\ u_i(x, 0, 0) - u_i(x, 0, L_{RVE}) + u_3^{D3} = 0 \end{array} \right\} \quad \left\{ \begin{array}{l} i = 1, 2, 3 \\ x \in R \mid 0 < x < L_{RVE} \\ y \in R \mid 0 < x < L_{RVE} \\ z \in R \mid 0 < x < L_{RVE} \end{array} \right. \quad (6.2)$$

$$\text{Group 3} \left\{ \begin{array}{l} u_i(0, L_{RVE}, L_{RVE}) - u_i(L_{RVE}, L_{RVE}, L_{RVE}) + u_1^{D1} = 0 \\ u_i(0, 0, L_{RVE}) - u_i(L_{RVE}, 0, L_{RVE}) + u_1^{D1} = 0 \\ u_i(0, L_{RVE}, 0) - u_i(L_{RVE}, L_{RVE}, 0) + u_1^{D1} = 0 \\ u_i(0, 0, 0) - u_i(L_{RVE}, 0, 0) + u_1^{D1} = 0 \\ u_i(0, 0, L_{RVE}) - u_i(0, L_{RVE}, L_{RVE}) + u_2^{D2} = 0 \\ u_i(0, 0, 0) - u_i(0, L_{RVE}, 0) + u_2^{D2} = 0 \\ u_i(0, 0, 0) - u_i(0, 0, L_{RVE}) + u_3^{D3} = 0 \end{array} \right\} \quad \{i = 1, 2, 3\} \quad (6.3)$$

Among the optimized arrays of the previous study related to the upper bound optimization, three volume fractions of the reinforcement have been considered, hereinafter referred to as V_f , i.e. $V_f=10\%$, $V_f=14\%$, $V_f=25\%$, and five particle distributions with 2, 4, 6, 8, and 10 number of particles hereinafter referred to as N_{part} . Three of the FE models employed are shown in Figure 5.2 and a typical RVE is meshed with Abaqus C3D10 tetrahedral and is comprised of 60000 elements.

Figure 5.3 shows a typical RVE with the mechanical load applied on the dummy node D_i and the thermal load applied by Abaqus temperature field throughout its region. The effect of spatial particle distribution, number of particles, and particle volume fractions on creep-cyclic

plasticity behaviour has been investigated by superimposing a tensile mechanical load $\sigma_p(t)$ along the x direction on a cyclic thermal load $\Delta\theta(t)$ with a dwell time $\Delta t = 1\text{hr}, 10\text{hrs},$ and 100hrs shown in Figure 5.3 (b). Constituent material properties were chosen to correspond to elastic SiC particles perfectly bonded to a Ti-6242 matrix that follow the data reported in Table 5.1.

Table 5.1 Mechanical properties at 500°C.

	SiC	Ti-6242
E (GPa)	380	95
ν	0.19	0.32
α ($^{\circ}\text{C}^{-1}$)	4.1e^{-6}	8.1e^{-6}
σ_y (MPa)	3450	350

Due to the temperature considered, it is relevant to evaluate the creep strain only for the titanium matrix. The creep constitutive equation adopted is the Norton law that represents the steady-state creep rate of the material within the secondary creep stage:

$$\dot{\varepsilon}^c = A \cdot \bar{\sigma}^n \cdot \exp\left(\frac{-Q_{eng}}{R_{gas} T}\right) \quad (6.4)$$

where $\dot{\varepsilon}^c$ denotes creep strain rate, n is the stress exponent, A is a constant, Q_{eng} is the activation energy, R_{gas} is the universal constant of gases, and T is the absolute temperature $[K]$.

Creep parameters are taken from the tensile creep test data of Ti-6Al-4V material in which test performed at 200MPa and 600°C [93]. Ti-6Al-4V material shows similar creep behaviour with Ti-6242. The creep properties are summarized in Table 5.2.

Table 5.2 Creep parameters.

Material	A [$\text{MPa}^{-n}\text{h}^{-1}$]	n	Q_{eng} [$\text{kJ} \cdot \text{mol}^{-1}$]	R_{gas} [$\text{J} \cdot \text{mol}^{-1} \cdot \text{K}^{-1}$]
Ti-6Al-4V	4432.45	4.6	267	8.314

5.3 Creep-cyclic plasticity of PRTMCs under thermo-mechanical loading

Recently, Giugliano *et al.* presented cyclic plasticity behaviours of the PRTMCs at 500°C as Figure 5.4. With the same RVE models, the creep-cyclic plasticity behaviours of the PRTMCs are investigated as an extended research work.

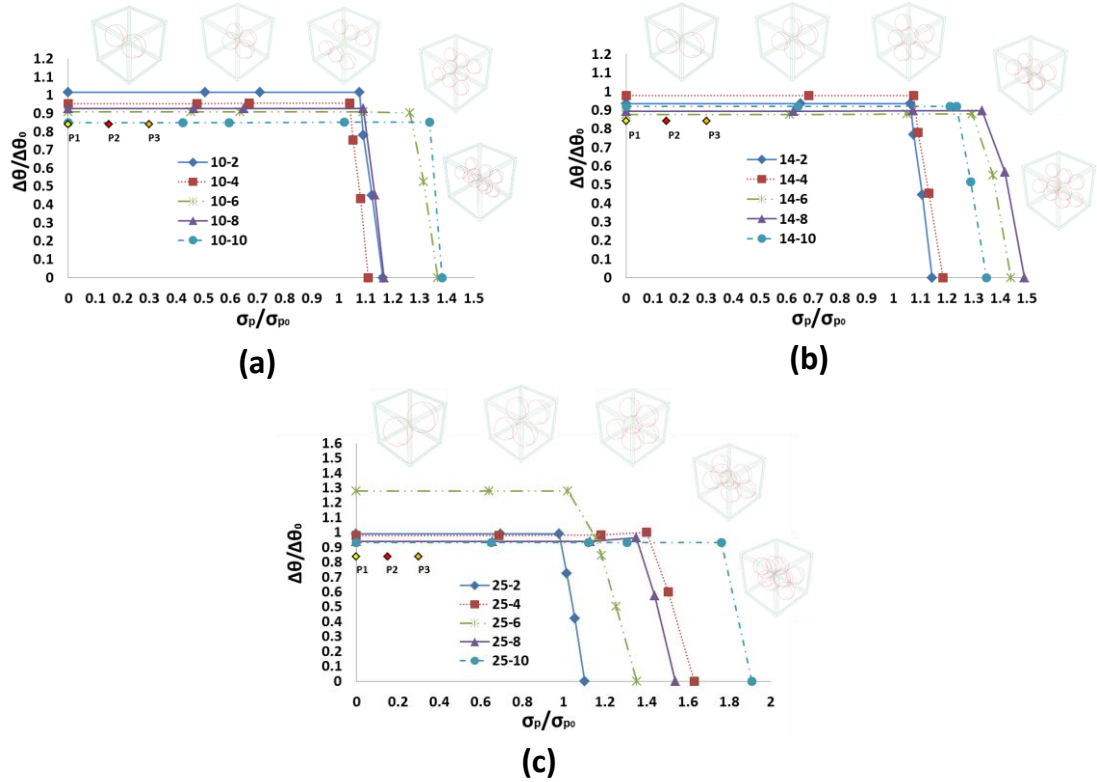


Figure 5.4 Shakedown boundaries for different particle arrangements with N_{part} 2, 4, 6, 8, and 10 and (a) $V_f=10\%$, (b) $V_f=14\%$ and (c) $V_f=25\%$ [91, 92].

Cyclic creep behaviours of the PRTMCs subjected to different cyclic load points which are P1 ($\sigma_p = 0$ and $\theta = 0.8\theta_0$), P2 ($\sigma_p = 0.15\sigma_{p0}$ and $\theta = 0.8\theta_0$), P3 ($\sigma_p = 0.3\sigma_{p0}$ and $\theta = 0.8\theta_0$) are analysed employing the LMM eDSCA method. Eq.(6.4) is used to obtain the creep parameter for the thermal loading $\theta = 0.8\theta_0$. A full incremental cyclic analysis is performed to verify the results analysed from the LMM eDSCA using Abaqus step-by-step (SBS) method for an RVE with $N_{part}=6$ and $V_f=10\%$ subjected to the load point P2.

Figure 5.5 presents resultant creep strain increment in the steady-state cycle analysed from the SBS shown in Figure 5.5(a) and the LMM eDSCA shown in Figure 5.5(b), where, the legends

in Figure 5.5, SDV6 denotes creep strain increment computed by the LMM eDSCA; CEMAG is the creep strain magnitude analysed by SBS method. The creep strain computed by the LMM eDSCA is in line with the result by the SBS. It is worth noting that the LMM eDSCA produces reliable results within a short computational time less than 10% of the SBS. Based on the efficient performance, the LMM eDSCA has been selected to analyse the creep-cyclic plasticity response of the PRTMCs rather than the conventional FEA.

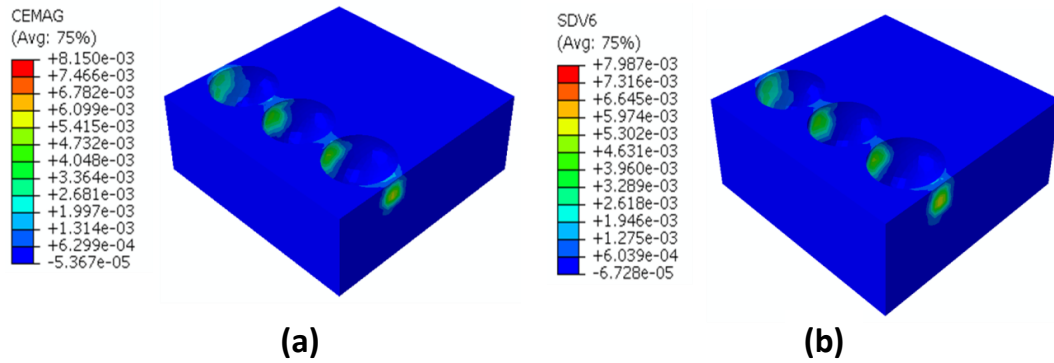


Figure 5.5 Creep strain contours for the micro-scaled SiC-Ti6242 PRTMCs subjected to a cyclic load point P2 for a dwell time of 10hrs; analysed by (a) Abaqus step-by-step method and (b) the LMM eDSCA.

5.3.1. Effect of spatial particle distribution on the creep-cyclic plasticity response

The fifteen different RVEs subjected to a cyclic load point P2, shown in Figure 5.4, are investigated for a dwell time of 10hrs. Creep strain and ratchetting strain are calculated for the most critical location where has the maximum creep strain accumulated at each RVE model. The results are summarised for a different volume fraction in Table 5.3. Stress-strain hysteresis loops for notable RVE models that have significant creep strain or ratchetting strain are presented in Figure 5.6.

Investigation results shown in Figure 2.4 demonstrate that when a structure is subjected to a cyclic loading point under shakedown boundary, structural responses in the steady state are likely to appear either no plastic strain increment or the creep enhanced plasticity. In this work, however, despite the loading level P2 located under the shakedown boundary for all RVEs, it is observed that all RVEs experience creep ratchetting by the cyclically enhanced creep. As mentioned, without creep effects, cyclic loading under both elastic and global shakedown limits do not induce any ratchetting mechanism. However, with creep, the structural response can be the creep ratchetting due to a variety of factors such as geometry, creep constant, other

material properties. Hence the creep-cyclic plasticity behaviours of a structure should not be predefined by the cyclic loading level but should be thoroughly investigated. From the results, there are no clear correlations between either creep strain or ratchetting strain and the number of particles for a fixed volume fraction. Therefore, the results demonstrate that spatial particle distributions have significant effects on high temperature damage tolerance.

Table 5.3 Creep strain and ratchetting strain from the cyclic creep and plastic analyses of all the RVE models.

No. of particles	Volume Fraction					
	10%		14%		25%	
	Creep strain (%)	Ratchetting strain (%)	Creep strain (%)	Ratchetting strain (%)	Creep strain (%)	Ratchetting strain (%)
2	0.57	0.28	0.55	0.25	1.92	2.00
4	0.52	0.30	0.46	0.23	0.38	0.16
6	0.62	0.18	0.70	0.43	0.15	0.07
8	0.51	0.24	0.69	0.22	0.38	0.10
10	1.65	0.32	0.42	0.10	0.51	0.09

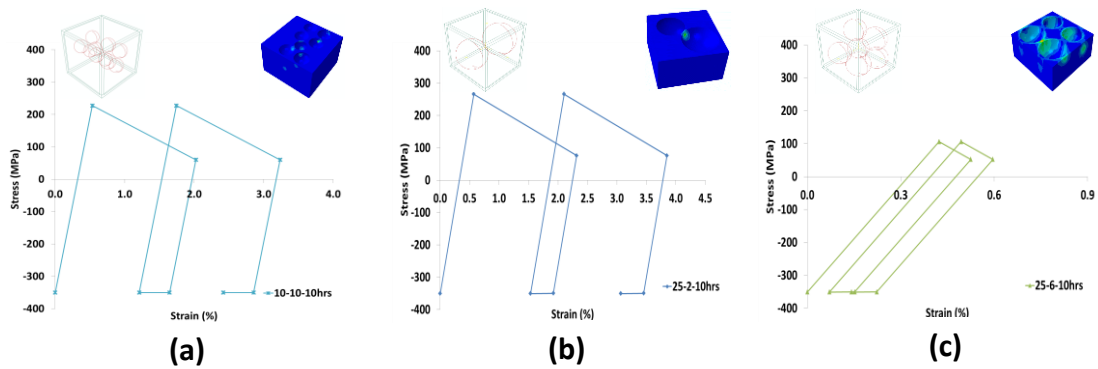


Figure 5.6 Steady state hysteresis loops of the RVE models subject to cyclic loading P2 for dwell time 10hrs; (a) $N_{part}=10$ with $V_f=10\%$, (b) $N_{part}=2$ with $V_f=25\%$ and (c) $N_{part}=6$ with $V_f=25\%$.

Some notable results are presented in Figure 5.6. The RVE for $N_{part}=10$ with $V_f=10\%$ and another RVE for $N_{part}=2$ with $V_f=25\%$ show the most considerable creep deformation. In particular, the latter RVE develops significant total strain range over 2% within a cycle. With reference to the cyclic loading P2 of the two concerning RVEs in Figure 5.4, their loading

levels are quite close to the reverse plasticity limit $\Delta\theta_{rp}$. On the contrary, the former, RVE for $N_{part}=6$ with $V_f=25\%$, shows the highest creep endurance under the same loading P2, where the cyclic load level is the furthest down from its reverse plasticity limit. Based on these observations, it can be seen that the cyclic load points closer to reverse plasticity limit may cause significant creep deformation.

5.3.2. Effect of varying dwell time and tensile load level on the creep-cyclic plasticity response

The parametric studies are carried out for an RVE model which has $N_{part}=6$ with $V_f=10\%$ in order to understand the effects of dwell time and a tensile load level on the creep-cyclic plasticity behaviour of the PRTMCs. The cyclic creep and plastic analyses are performed for the RVE models which are subjected to each cyclic load point P1, P2, and P3 using the LMM eDSCA for three independent dwell of 1hr, 10hrs, and 100hrs. Figure 5.7 presents the hysteresis loops constructed for the most critical element of each case. Creep strain and ratcheting strain analysed are summarised in Table 5.4.

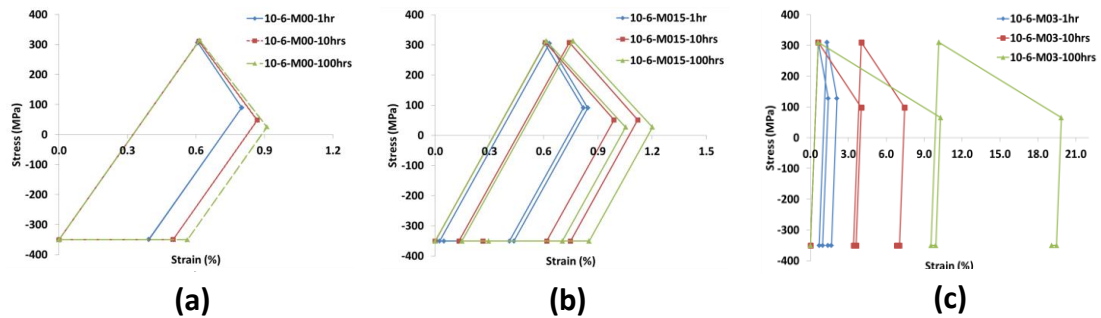


Figure 5.7 Steady-state hysteresis loops of an RVE model that has $N_{part} = 6$ with $V_f = 10\%$ for variations of dwell 1hr, 10hrs, and 100hrs at cyclic load point; (a) P1, (b) P2 and (c) P3.

For the non-tensile load shown in Figure 5.7 (a), the dwell stress relaxation affects the unloading plasticity but closed hysteresis loops appear for all the dwell times. As dwell increases, creep deformation increases, but the magnitude of the end of dwell stress decreases. Different from other thermal stress induced by non-isothermal loading over a structure, the RVE has the thermal stress caused by a difference of thermal expansion coefficients between the titanium phase and the silicon carbide in the isothermal condition. Therefore, no back stress

effects exist during the relaxation; the pure thermal stress will be close to zero over a long-term dwell.

For the tensile loads shown in Figure 5.7 (b) and Figure 5.7 (c), creep ratchetting responses occur at every dwell time due to the cyclically enhanced creep. In overall, creep deformations significantly increase as tensile load level increases despite the same dwell. Interesting points to be noted from Figure 5.7 are that the RVE models subjected to the larger tensile load level P3 have the dwell relaxation started and ended at higher stress level than the others P1 and P2. When the tensile load and the thermal load are applied to the RVE models, primary tensile stresses and secondary compressive stresses develop respectively. Critical stresses combined between the primary and secondary stresses in the RVE models are likely to occur at locations where the metal matrix encloses the particles as shown in Figure 5.6.

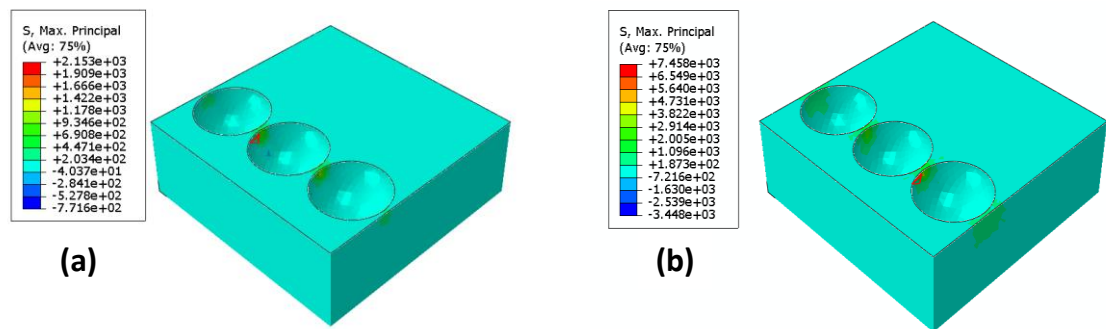


Figure 5.8 Maximum principal stress distributions of a RVE model $N_{\text{part}} = 6$ with $V_f = 10\%$ for dwell time 10hrs: (a) $\sigma_p = 0$ and (b) $\sigma_p = 0.15\sigma_{p0}$.

Table 5.4 Creep and ratchetting strain from the creep behaviour analyses of $N_{\text{part}} = 6$ with $V_f = 10\%$.

Cyclic load point	Dwell time	Creep strain (%)	Ratchetting strain (%)
<i>P1</i>	1hr	0.39	0.00
	10hrs	0.50	0.00
	100hrs	0.56	0.00
<i>P2</i>	1hr	0.41	0.04
	10hrs	0.62	0.18
	100hrs	0.70	0.22
<i>P3</i>	1hr	0.93	0.80
	10hrs	3.55	3.50
	100hrs	9.84	9.25

The maximum principal stress of the RVE models subjected to the three different loadings P1, P2, and P3 is investigated in order to find a dominant stress component of the von-Mises stress shown in Figure 5.7. Figure 5.8 exhibits contours of the maximum principal stress distributions for P1 and P2. The locations where the critical stress imposed have the tensile maximum principal stress component, whereas the rest of the metallic phase in the RVE model has the compressive stress component.

Hence, as the tensile load increases, the start and the end dwell stress level increase, while the thermal stress being in relaxations for the same dwell. From Table 5.4, it can be presumed that creep strain may be accumulated over 1% for a dwell of an hour within a cycle if the tensile load level exceeds P3. Therefore, the creep damages should be carefully assessed when the PRTMCs is subjected to tensile loading condition along with the cyclic thermal load.

5.3.3. Effect of volume fractions on the creep-cyclic plasticity response for a fixed particle arrangement

As demonstrated in Section 6.3.2, the optimised particle distributions in the RVE models do not directly benefits to creep endurance. However, it is worth investigating what influences of the variations of the particle arrangement giving to the creep-cyclic plasticity behaviour of the PRTMCs. For the investigations, cyclic creep and plastic analysis are performed for RVE models that have a fixed particle distribution concerning a number of particles.

Two RVE models which have $N_{\text{part}}=6$ and $N_{\text{part}}=10$ with $V_f=25\%$ each are selected as a reference particle arrangement. For each number of particles, four RVE models are created for different volume fractions of 10%, 14%, 18%, and 22% with a fixed arrangement. The cyclic creep and plastic analysis is performed for the eight RVE models subjected to the cyclic load point P2 for a dwell time of 10hrs. Figure 5.9 presents stress-strain hysteresis loops for the most critical element of each RVE model in the steady-state. Table 5.5 reports creep and ratchetting strain accumulated for each RVE model.

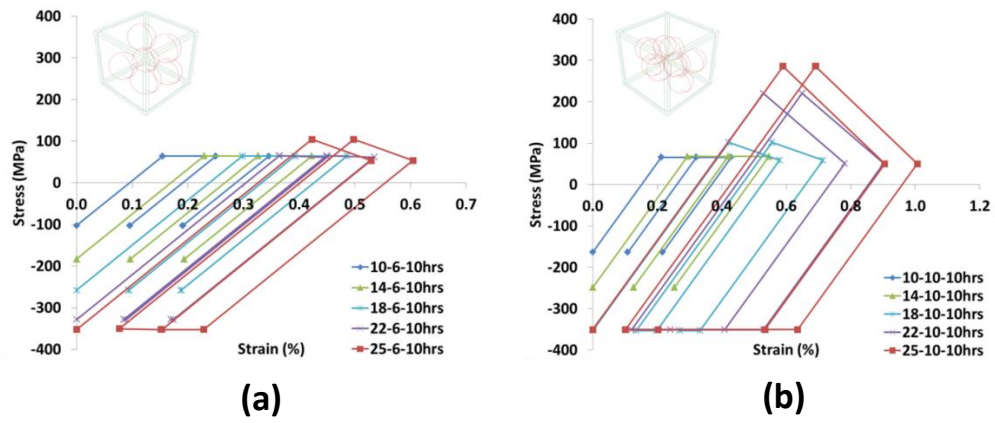


Figure 5.9 Steady-state hysteresis loops of RVE models that have a fixed particle arrangement subjected to cyclic loading P2 and dwell time of 10hrs with variations of volume fractions: (a) $N_{part}=6$ and (b) $N_{part}=10$.

Overall results from both numbers of particles present that the cyclically enhanced creep leads to creep ratchetting response without loading plasticity. As a common trend in Figure 5.9, both $N_{part}=6$ and $N_{part}=10$ models have an increase in the stress range as volume fraction increases. An interesting point to be noted is that RVE models with volume fractions that do not induce unloading plasticity have approximately the same creep strain of 0.1%.

Table 5.5 Creep and ratchetting strains for $N_{part}=6$ and $N_{part}=10$ of RVE models that have a fixed particle arrangement subjected to cyclic loading P2 and dwell time of 10hrs with variations of volume fractions.

Number of Particles	Volume fractions (%)	Creep strain (%)	Ratchetting strain (%)
6	10	0.10	0.10
	14	0.10	0.10
	18	0.09	0.10
	22	0.09	0.09
	25	0.15	0.08
10	10	0.11	0.11
	14	0.13	0.13
	18	0.20	0.13
	22	0.41	0.12
	25	0.53	0.12

Conversely, the creep strain increases once unloading plasticity appeared, and it keeps on increasing as the unloading plastic strain increases. By increasing the volume fraction within a fixed particle arrangement, a stress concentration occurs around the reinforcement due to the

reduced amount of the titanium matrix. In additions, when the RVE model has the unloading plasticity accumulated, the residual stress from the unloading instance affects the start dwell stress to increase; eventually, it leads to an increase in creep strain accumulation. In the sense of the above investigations, $N_{\text{part}}=10$ models may have less stress concentration around the reinforcement than $N_{\text{part}}=6$ models, which results in the unloading plasticity taking place early. In the meantime, the ratchetting strains accumulated for both numbers of particles do not have any influences from the variation of volume fraction.

5.4 Chapter Summary

The creep-cyclic plasticity behaviours of the PRTMCs was investigated through the LMM eDSCA. Key observations from the results are summarised as follows:

All the RVE models analysed show creep ratchetting responses due to cyclically enhanced creep, despite a cyclic load applied is under the strict shakedown boundary. Despite the same number of particles, variations of volume fractions have no direct influences on creep or ratchetting endurances due to non-uniform spatial particle distribution. Therefore, the numerical results demonstrate again that tailoring of the reinforcement arrangement affects the high temperature damage tolerance substantially. Nevertheless, the non-uniform spatial particle distribution, a cyclic loading closer to the reverse plasticity limit causes significant creep deformation. Moreover, tensile load level has significant effects on both creep strain and ratchetting strain increment as a dwell increases.

For RVE models with a fixed particle arrangement, variations of volume fractions have effects on a magnitude of a stress range within a cycle, which enhance unloading plasticity as volume fractions increase. On the other hand, a large number of particles augments the total strain range for the same volume fraction. Therefore, an RVE model that has a smaller volume fraction exhibits outstanding creep endurance.

6. Creep-fatigue endurance of a superheater outlet tube plate under non-isothermal loading and multi-dwell condition

6.1 Introduction

With decades of development, the steam power plants have become the primary source of electricity throughout the world. They typically use steam as the working fluid and operate on the Rankine Cycle [94]. As a crucial part of a steam power plant, a traditional and standard shell-and-tube heat exchanging equipment, the superheater has been broadly employed in oil and energy industries [95]. The superheaters often work together with reheaters to increase the saturated steam temperature and make the electricity generation process more efficient. As typical single-phase heat exchangers, they operate the steam inside inner pipes and allow the flue gas outside to heat the steam, in the form of cross-flow [96]. They are relatively inexpensive and straightforward to produce and maintain, also being adaptive and reliable to withstand working conditions of high temperature and pressure. Among the numerous components of a superheater, tube plates are one of the most critical parts which are attached to the tubes and shell simultaneously. Extremely sophisticated loading conditions can often be detected in a tube plate comprising both complex thermal and mechanical loadings, which may additionally induce creep and fatigue damage.

There are two ways to conduct a creep-fatigue assessment in the field of industry: rule-based and analysis-based. Rule-based methods widely adopted by UK's R5 procedures and ASME NH are usually considered to be over-conservative and inaccurate. Meanwhile, the finite element (FE) analysis-based method has been developed for the structural integrity assessment at high temperature and improved dramatically in the past decade, especially for Direct Methods that can balance between time-efficiency and accuracy compared to the time-consuming step by step analysis. The LMM eDSCA is one of the representative Direct Methods for evaluating creep-cyclic plasticity behaviour of structures at elevated temperature and capacity of the LMM eDSCA can predict creep-fatigue damage life by performing implemented in-house post-processing codes [15, 97].

However, since the LMM eDSCA subroutine can only consider isothermal creep parameters and one dwell period in a load cycle, there is some limitation for the LMM eDSCA to solve more complex engineering problems such as structures in non-isothermal condition or multi-dwell creep behaviour within a loading cycle. Besides, numerical procedures implemented in

the LMM eDSCA are not able to predict creep stress relaxation history over dwell time. Therefore, the LMM eDSCA was only able to compute the creep damage with an average creep stress value, providing slightly conservative life prediction. Hence the LMM eDSCA is further modified to overcome these limitations, and the detailed update is described in Section 3.4.2.

In this Chapter, with the modified LMM Framework, effects of the non-isothermal loading on the cyclic creep behaviour and the creep-fatigue life of tube plate under multi-dwell periods are thoroughly investigated. The real geometry data of the forged superheater outlet tube plate and a practical loading condition with six months of operation period are considered. By applying the temperature dependent material parameters taken from experimental data, it obtains the trustworthy structural response under cyclic creep effects and creep-fatigue life of the tube plate. Various methods are used for creep-fatigue damage evaluation of the tube plate. For creep damage evaluation, Time Fraction rule (TF), Ductility Exhaustion method (DE), and Strain Energy Ductility Exhaustion method (SEDE) are employed. For fatigue damage evaluation, the Modified Universal Slope Method (MUSM) and Designed Fatigue Curve provided in ASME NH are considered. For total damage evaluation, the Linear Damage Summation (LDS) method and the Unified Creep-Fatigue equation are used. In consideration of the multiaxial stress state, two types of multiaxial ductility factor (MDF) are employed for the damage evaluation.

Section 6.2 introduces the overall investigation procedures. Section 6.3 provides problem descriptions and relevant modelling parameters, where Section 6.3.1 describes the finite element model, boundary conditions and loading waveforms of the tube plate structures, where Section 6.3.2 presents material properties and relevant parameters employed for predicting creep-cyclic plasticity behaviour and creep-fatigue damage models. Section 6.4 demonstrates the performance of the extended LMM eDSCA with numerical results and provides comprehensive discussions on the creep-fatigue interaction of the tube plate. In detail, Section 6.4.1 focuses on cyclic creep-plasticity behaviour of the tube plate and presents the complex structural response clearly with hysteresis stress-strain loops. Section 6.4.2 deals with the creep-fatigue damage life of the tube plate based on the damage models mentioned earlier. Finally, Section 6.5 concludes with critical remarks and findings.

6.2 Investigation Procedures

A flowchart is firstly proposed to exhibit the logic of the numerical investigation in this work in Figure 6.1.

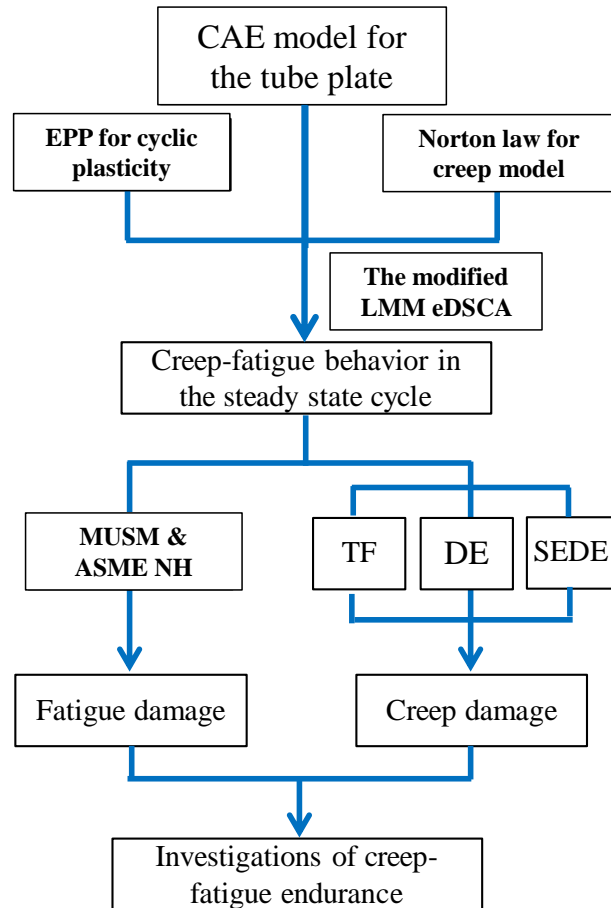


Figure 6.1 A proposed flow chart for the study of the tube plate through the modified LMM eDSCA method.

The numerical procedures of the modified LMMF with the combinations of a CAE model, the elastic perfectly plastic (EPP) model with temperature dependent yield stresses as well as a temperature dependent creep constitutive equation (Norton law) are used to analyse the cyclic creep and plasticity behaviours of the tube plate in the steady-state cycle. After that, the Modified Universal Slope Method (MUSM) and the Design Fatigue Curve provided in ASME NH are used to evaluate fatigue damage and the Time fraction (TF), the Ductility Exhaustion model (DE) and the Strain Energy Density Exhaustion model (SEDE) are employed to assess creep damage evaluation. Finally, the Linear Damage Summation (LDS) method and the unified creep-fatigue equation are used to evaluate the total damage evaluation. The damage

endurance evaluated demonstrates a trend of conservativeness of each evaluation method comparing to experimental data.

6.3 Problem Description

6.3.1. Finite element model and boundary conditions

An FE model of the simplified superheater tube plate with the 14 tailpipe configurations is created as shown in Figure 6.2. Some features on the actual industrial tube plate are not modelled including the steam pipes (thin pipes that penetrate through the bores), pintles (connection components between steam pipes and tube plate on external surface in Figure 6.2 (b)), internal tailpipes (connection components between steam pipes and tube plate on internal surface in Figure 6.2 (a)), and sheath tube (a case being welded to tube plate on surface in Figure 6.2 (d)). The reason is that the stress concentration occurs around the bore surface of the tube plate perforation regardless of the presence of these features. The corners inside the tube plate have been modelled with round fillets albeit that the gouge outside the tube plate for gimbal attachment has been neglected. It is worth mentioning that only nominal dimensions are adopted during the modelling process as no corrosion or erosion is considered. The detailed dimensions are shown in Table 6.1 and Figure 6.3 (a) and (b).

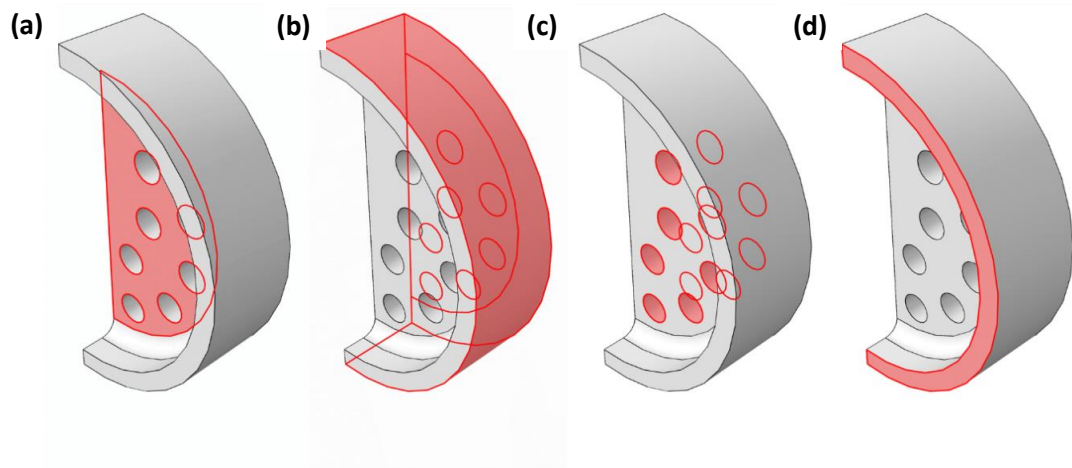


Figure 6.2 Simplified 3-dimensional tube plate model with certain surfaces selected: (a) internal surface, (b) external surface, (c) tube holes, and (d) sheath tube weld surface.

Half of the whole tube plate is modelled since the structure is symmetric about the y-z plane. The FE model is constructed and meshed using commercial finite element software ABAQUS as shown in Figure 6.3 (c). The model consists of 15832 quadratic brick elements. For heat

transfer analysis and stress analysis, the identical geometry and mesh configurations are used excepting the element type, where DC3D20 for heat transfer analysis and C3D20R for stress analysis respectively.

Table 6.1 Geometry dimensions of the tube plate (all dimensions in mm)

T	t	D	d	a
110	60	421	38.3	24

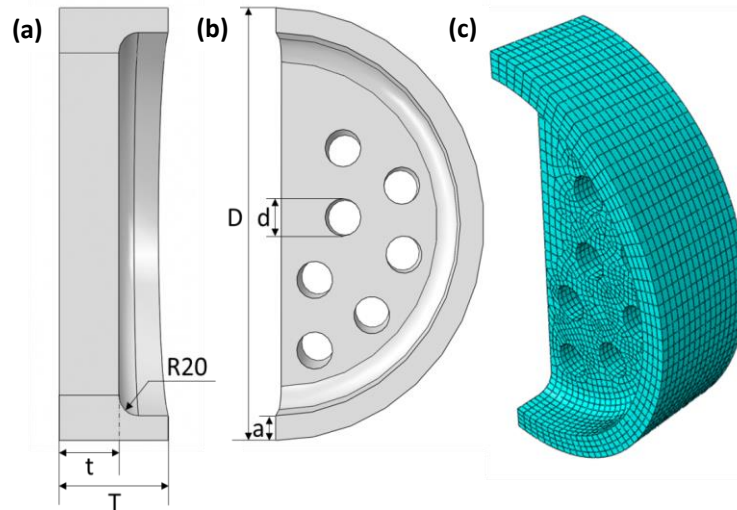


Figure 6.3 (a) Side view of the tubeplate model, (b) Front view of the tubeplate model, and (c) meshed tube plate.

The loading waveform and boundary condition are assumed based on the actual working condition of a six months' super-heater operation. For normal full power reactor transient, the gas inlet temperature is $680\text{ }^{\circ}\text{C}$ and the gas pressure is 4.1 MPa , which are applied to the external surfaces in Figure 6.2 (b) of the tube plate. The steam temperature is $530\text{ }^{\circ}\text{C}$ and the steam pressure is 16.9 MPa , which are applied to the inside surfaces in Figure 6.2 (c) of the bores of tube plate. With multi-dwell stages in the loading waveform, it considers the thermal and mechanical loads cycle between 100% of full power loading and 105% of full power loading, as shown in Figure 6.4.

No pressures are applied on the internal surfaces in Figure 6.2 (a) of the tube plate, which operates at atmospheric pressure. The thermal load is simplified such that it applies the temperature directly to the surfaces without considering heat transfer coefficients between the working fluid and solid structure. The reason is not only for simplicity but also for conservatism as the simplified thermal condition has been proved to yield larger thermal stress

than the actual working condition. In addition, only the pressure and temperature loading are considered, but the self-weight of the tube plate is neglected since it has an insignificant effect on simulation results.

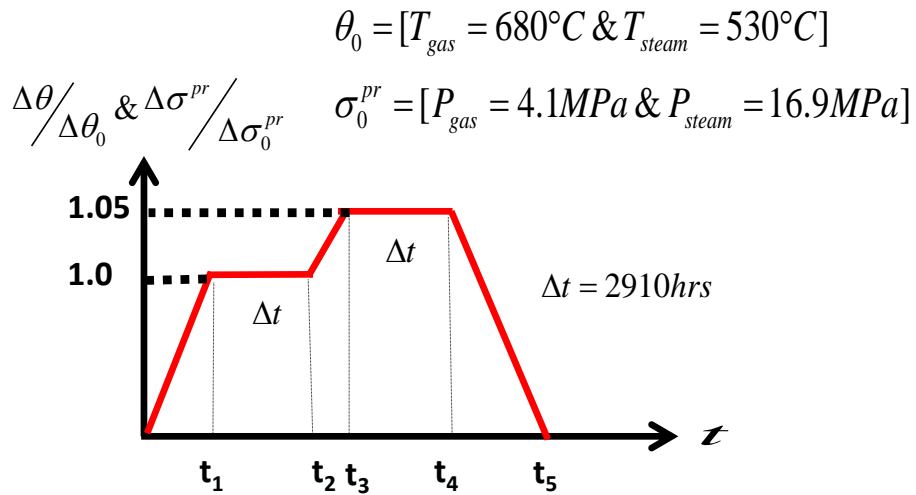


Figure 6.4 Loading waveform under multi-dwell for six months operations.

A reference point is created with six degrees of freedom fixed at the centre of tube plate, which is also connected to the tube plate - sheath tube weld surface (surface in Figure 6.2 (d)) by means of kinematic coupling constraint. This constraint has been configured to allow the weld surface to expand only in radial direction. In addition, a symmetry boundary condition about x-direction has been applied to simulate the whole structure with the half model. According to the trial heat transfer assessment, the circumferential distribution of temperature alongside the sheath tube may cause the deformation of the weld surface in both axial and circumferential directions. Thus the existing boundary condition may over-constrain the surface in the circumferential direction. But this over-constraint is acceptable because the stiffness of the tube plate is judged to be much larger than the sheath tube in the case of this deformation mode.

Regarding the deformation in the axial direction, it has confirmed that stress concentration happens within the tube plate body, away from the area affected by the axial temperature variation. Therefore, regarding rationality and simplicity, these influences have been disregarded. Incidentally, in accordance with actual working conditions, there are some constraints and end-pipe loadings generated from tailpipes and steam tubes being also neglected herein because they are quite flexible and are remote from regions of stress concentration.

6.3.2. Material properties and modelling parameters

- **Cyclic plasticity**

Type 316 stainless steel is often used as a material for the superheater outlet tube plate. To obtain conservative results, cyclic plasticity of the tube plate was analysed using the elastic-perfectly plastic model (EPP) with temperature dependent yield stresses. Table 6.2 shows the temperature-dependent yield stresses for the temperature ranges between 20°C and 750°C. The yield stresses unspecified in Table 6.2 are calculated by extrapolation method implemented in the modified LMM eDSCA.

Table 6.2 Temperature dependent yield stresses of Type316 stainless steel

Temp. [°C]	20	500	550	600	650	700	750
σ_y [MPa]	205	110	105	100	95	90	85

- **Creep constitutive model**

Considering that each dwell period is three months, the inelastic deformation of the tube plate due to creep is assumed to follow Norton law which shows the secondary creep regime and the temperature dependent creep parameter $A^* \exp\left(\frac{-Q_{eng}}{R_{gas} T}\right)$ is applied by using Arrhenius law,

$$\dot{\varepsilon}^c = A^* \cdot \exp\left(\frac{-Q_{eng}}{R_{gas} T}\right) \bar{\sigma}^n \quad (6.1)$$

where $\dot{\varepsilon}^c$ is the equivalent creep strain rate; A^* is the frequency factor; Q_{eng} is the activation energy [$KJ \cdot mol^{-1}$]; R_{gas} is the gas constant [$J \cdot mol^{-1} \cdot K^{-1}$]; T represents temperature in Kelvin [K]; n is the stress component. The detailed creep parameters are listed in Table 6.3.

Table 6.3 Creep parameters for calculating creep strain.

A^*	Q	R	n
46333.8	330	8.314	6.1

- **Creep-fatigue damage models**

The framework of Linear Damage Summation (LDS) divides the creep-fatigue estimation into two parts, namely the fatigue damage and creep damage in the steady-state cycle. The equation of the general creep-fatigue life prediction based on LDS can be expressed as

$$N_{cf} = \frac{1}{D_f + D_c} \quad (6.2)$$

where N_{cf} is the number of cycles to creep-fatigue failure, D_f and D_c respectively denote fatigue and creep damage in the steady-state cycle.

As mentioned in Section 2.2.1.2, the Modified Universal Slope Method (MUSM) is used to calculate fatigue damage d_f^{MUSM} of Type 316 stainless steel. Eq.(2.4) is converted to half cycle $\frac{\Delta\varepsilon}{2} - 2N_f$ design fatigue curve. With consideration of the high temperature operating condition, tensile strength σ_B of Type 316 stainless steel is replaced with creep rupture stress of 68 MPa at 700 °C for 10,000 hours and fatigue ductility ε_f is assumed to be 0.4 which is found to be 0.077 at room temperature. If tensile strength decreases and fatigue ductility increases, the number of cycle to fatigue failure N_f shorten, leading to predict more conservative fatigue lifetime than one at room temperature.

$$\frac{\Delta\varepsilon}{2} = 0.623 \left(\frac{\sigma_B}{E} \right)^{0.832} 2N_f^{-0.09} + 0.0196 \varepsilon_f^{0.155} \left(\frac{\sigma_B}{E} \right)^{-0.53} 2N_f^{-0.56} \quad (6.3)$$

TF, DE, and SEDE methods are employed to predict creep damage life and compare the prediction capacities. It is known that TF and DE have been widely used in engineering structures and incorporated into ASME NH, RCC-MRx, and R5 procedure respectively. However, some limitations remain in predictions of increased creep damage of Type 316 stainless steel for longer dwell periods.

The multiaxial rupture stress, σ_{RUP} , and creep rupture time, t_f , are considered to be the two dominated parameters that have a great impact on creep damage in the steady-state cycle in TF model, which is given by

$$d_c^{TF \cdot \sigma_{RUP}} = \int_0^{\Delta t} \frac{dt}{t_f(\sigma_{RUP}, T)} \quad (6.4)$$

where $d_c^{TF \cdot \sigma_{RUP}}$ is the creep damage in the steady-state cycle by using the TF model. The function of $t_f(\sigma_{RUP}, T)$ can be expressed as the following two equations:

$$\log t_f(\sigma_{RUP}, T) = k \cdot \sigma_{RUP}^{-\alpha} \quad (6.5a)$$

$$\sigma_{RUP} = 0.133 \times 3\sigma_m + 0.867\bar{\sigma} \quad (6.5b)$$

where k and α are two material constants in the power-law relationship, and $\bar{\sigma}$ is the instant equivalent stress. The magnitudes of k and α at various temperatures between 500 °C to 750 °C for the TF model are based on reference [98], as listed in Table 6.4. The parameters k and α for non-specified temperatures between 500 °C and 750 °C are calculated using the interpolation technique implemented in the modified LMM eDSCA.

Table 6.4 Material constants for TF model of type 316 stainless steel

Temperature °C	k	α
500	1557.2	1.02
550	290	0.777
600	86.305	0.598
650	38.861	0.483
700	22.276	0.406
750	15.526	0.363

The multiaxial creep damage is calculated on the basis of R5 ductility exhaustion model (DE), where the creep ductility, ε_f^c , has a function of the creep strain rate $\dot{\varepsilon}^c$ and temperature. The creep damage in the steady-state cycle with the combinations of DE model and multiaxial ductility factor (MDF), $d_c^{DE \cdot MDF}$, can be written as

$$d_c^{DE \cdot MDF} = \int_0^{\Delta t} \frac{\dot{\varepsilon}^c}{\bar{\varepsilon}_f^c(\dot{\varepsilon}^c, T) \cdot MDF} dt \quad (6.6)$$

In the uniaxial form, the creep ductility ε_f^c can be expressed by:

$$\varepsilon_f^c = \min. \left[\varepsilon_U, \text{Max.} \left(\varepsilon_L, B^* \dot{\varepsilon}_c^{m^*} \right) \right] \quad (6.7)$$

where ε_U is the upper shelf at high strain rates; ε_L is the lower shelf at low strain rates; B^* and m^* are the material parameters. Creep ductility $\bar{\varepsilon}_f^c$ that considers effects of MDF can be represented as Eq. (6.8):

$$\bar{\varepsilon}_f^c = \varepsilon_f^c(\dot{\varepsilon}^c, T) \cdot \text{MDF} = \varepsilon_f^c(\dot{\varepsilon}^c, T) \exp \left[p \left(1 - \frac{\sigma_1}{\bar{\sigma}} \right) + q \left(\frac{1}{2} - \frac{3\sigma_m}{2\bar{\sigma}} \right) \right] \quad (6.8)$$

where σ_1 and σ_m are the maximum principal stress, mean or hydrostatic stress respectively; $p = 2.38$ and $q = 1.04$ are the empirically derived constants for austenitic steels[99]. Parameters for Eq.(6.7) should consider non-isothermal temperature effects, but limited data published. Thus parameters of uniaxial creep ductility of ex-service Type 316 H at 570 °C and 600 °C are employed for creep damage evaluation based on DE method. The detailed parameters are listed in Table 6.5. According to Section 6.4 analysis results, maximum creep deformation occurs near the tube holes, and this region has a temperature range from 530 °C to 560 °C .

Table 6.5 Material constants for creep ductility of type 316H stainless steel [100].

ε_U (%)	B^*	m^*	ε_L (%)
50	1.0496	0.3258	6.04

Wen *et al.* [63] proposed the MDF_{WEN} as an alternative way of the MDF provided in R5, which can be expressed as:

$$\text{MDF}_{\text{Wen}} = \exp \left[\frac{2}{3} \left(\frac{n-0.5}{n+0.5} \right) \right] / \exp \left[2 \left(\frac{n-0.5}{n+0.5} \right) \frac{\sigma_m}{\bar{\sigma}} \right] \quad (6.9)$$

The SEDE model containing MDF_{Wen} is firstly introduced by this research, where the inelastic strain energy density rate, \dot{w}_{in} , and the failure strain energy density, w_f , are used to evaluate the creep damage:

$$d_c^{SEDE \cdot MDF_{Wen}} = \int_0^{\Delta t} \frac{\dot{w}_{in}}{w_f(\dot{w}_{in}, T) \cdot MDF_{Wen}} dt \quad (6.10)$$

where $d_c^{SEDE \cdot MDF_{Wen}}$ is the creep damage in the steady-state cycle by considering SEDE and MDF_{WEN} . Similarly, the function of $w_f(\dot{w}_{in}, T)$ by considering the Arrhenius law:

$$w_f = B_1 \exp\left(\frac{\Delta G_{SEDE}}{RT}\right) \cdot \dot{w}_{in}^{B_2} \quad (6.11)$$

where B_1 and B_2 are two material constants for the expression of failure strain energy density, and ΔG_{SEDE} is the activation energy range in the SEDE model. The parameters of SEDE model are fitted to SMDE data of Type 316H stainless steel [100] and listed in Table 6.6.

Table 6.6 Material constants for SEDE model of Type 316H stainless steel.

B_1	B_2	ΔG_{SEDE}
1.795	0.16	25843

Different from the previous work for pure strain-controlled tests, the complicated structures are always subjected to mixed strain-stress controlled situations for each integration point. In such a case, it is worth to mention two different cases that describe the elastic follow-up factor during dwell periods, as seen in Figure 6.5.

Based on that, the calculations of inelastic strain energy density rate, w_{in} , can be presented as shaded areas defined by:

$$w_{in} = \Delta \bar{\epsilon}^c \cdot \bar{\sigma}_c + \frac{1}{2} \left\{ \Delta \bar{\epsilon}^c \cdot (\bar{\sigma}_s - \bar{\sigma}_c) \right\}, (\bar{\sigma}_s > \bar{\sigma}_c) \quad (6.12a)$$

$$w_{in} = \Delta \bar{\varepsilon}^c \cdot \bar{\sigma}_s + \frac{1}{2} \{ \Delta \bar{\varepsilon}^c \cdot (\bar{\sigma}_c - \bar{\sigma}_s) \}, (\bar{\sigma}_c > \bar{\sigma}_s) \quad (6.12b)$$

where $\Delta \bar{\varepsilon}^c$ is the equivalent creep strain range during one dwell period, and $\bar{\sigma}_s$ and $\bar{\sigma}_c$ respectively denote the equivalent von-Mises stress at the beginning and end of one dwell period.

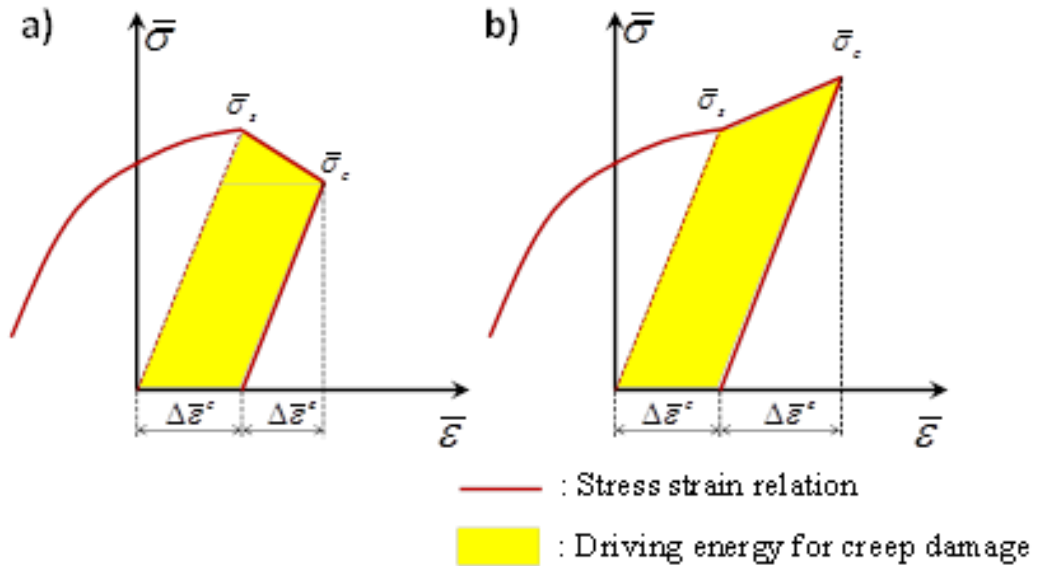


Figure 6.5 Inelastic strain energy which leads to the creep damage: (a) $\bar{\sigma}_s > \bar{\sigma}_c$ and (b) $\bar{\sigma}_c > \bar{\sigma}_s$.

After the estimations of fatigue and creep damages, the creep-fatigue interaction diagram provided in ASME NH for type 316 stainless steel can be shown in Figure 6.6, where the vertical axial is defined as total creep damage, D_c , and horizontal axial is defined as total fatigue damage, D_f .

As mentioned in Section 2.2.2.1, the unified creep-fatigue equation in power-law form is used to predict the total damage life $d_{total}^{unified}$ in the steady-state cycle, which can be defined as

$$\varepsilon_p = C_0 \left[1 - c_1 (T - T_{ref}) \right] N_{f-temp}^{-\beta_0 [1 - b_1 (T - T_{ref})]} \quad (6.13)$$

where ε_p is the plastic strain; C_0, c_1, β_0 , and b_1 are the coefficients; T_{ref} is the reference temperature of 873 K. It should be mentioned that total strain range $\Delta\bar{\varepsilon}_{total}$ is used to predict conservative creep-fatigue damage life instead of using ε_p .

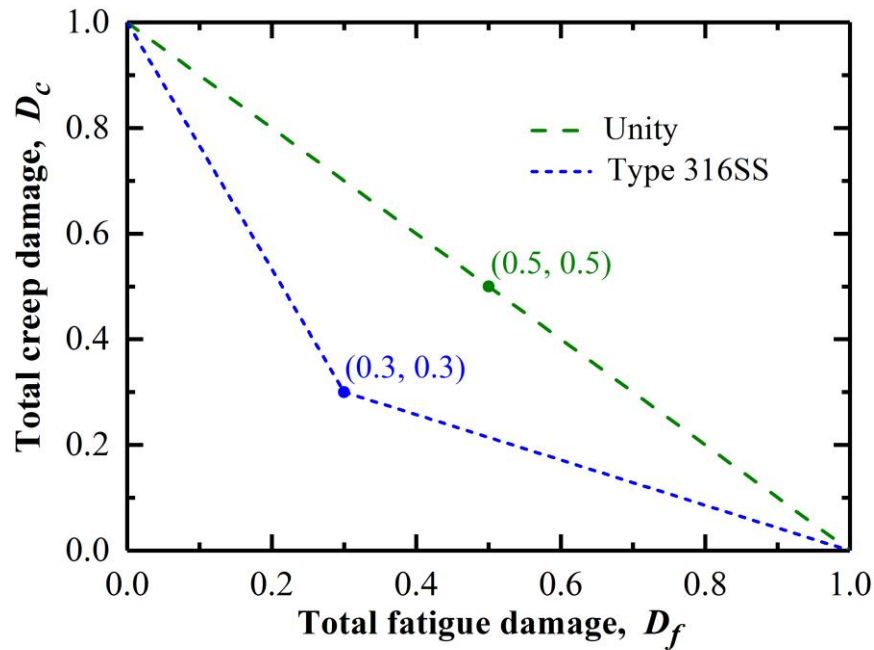


Figure 6.6 Creep-fatigue damage envelope for Type 316 stainless steel in ASME NH design codes.

Table 6.7 shows the coefficients of Eq.(6.3) for fatigue damage evaluation of type 316 stainless steel.

Table 6.7 Coefficient of Eq.(6.13).

Temp. range	C_0	c_1	β_0	b_1
723K – 873K	1.997	0.002955	0.62375	-0.000309
873K – 923K	2.452	0.002668	0.80713	0.00088

6.4 Numerical Results and Discussions

6.4.1. Creep-cyclic plasticity behaviour

The linear elastic analysis is performed for the superheater tube plate subjected to the mechanical load, the thermal load, and the thermo-mechanical load respectively, so that

individual loading effects on the tube plate can be understood. The resultant elastic von-Mises stress contours for each loading are illustrated in Figure 6.7.

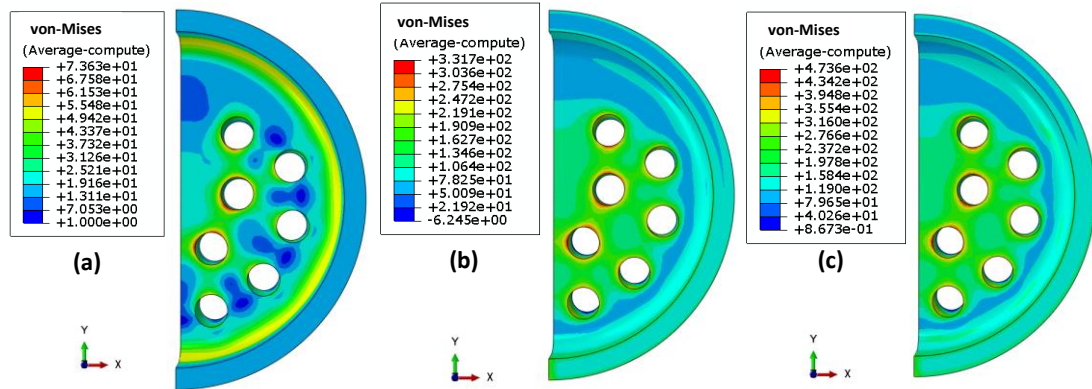


Figure 6.7 Elastic stress solutions: (a) mechanical load only, (b) thermal load only, and (c) both mechanical and thermal loads.

Figure 6.7 shows that maximum equivalent stress occurs at holed areas of tube under all three loads. The magnitude of equivalent stress under the thermal load is over four times larger than that under the mechanical load. Figure 6.7 (c) shows similar equivalent stress distribution contour with the stress distribution under the thermal load only but shows the larger magnitude of the equivalent stress. Hence it can be presumed that the thermal load is the dominant stress component in the thermo-mechanical loading condition, and both the mechanical load and the thermal load produce tensile stresses. It is noteworthy that the maximum magnitude of equivalent stress under the thermo-mechanical loads is more substantial than elastic stress range at tube holed area, hence it is predicted that the tube plate may have significant plastic deformation during loading and unloading load instances.

The cyclic creep and plastic analysis is performed for the tube plate subjected to the thermo-mechanical load and the multiple dwell periods using the modified LMM eDSCA. Figure 6.8 exhibits temperature distribution and temperature dependent creep parameters $A^* \exp\left(\frac{-Q_{eng}}{R_{gas} T}\right)$ over the tube plate at each dwell period. As one of the improvements of the modified LMM eDSCA, the temperature dependent creep parameter effects shown in Figure 6.8 have been considered in creep-cyclic plasticity behaviour analysed.

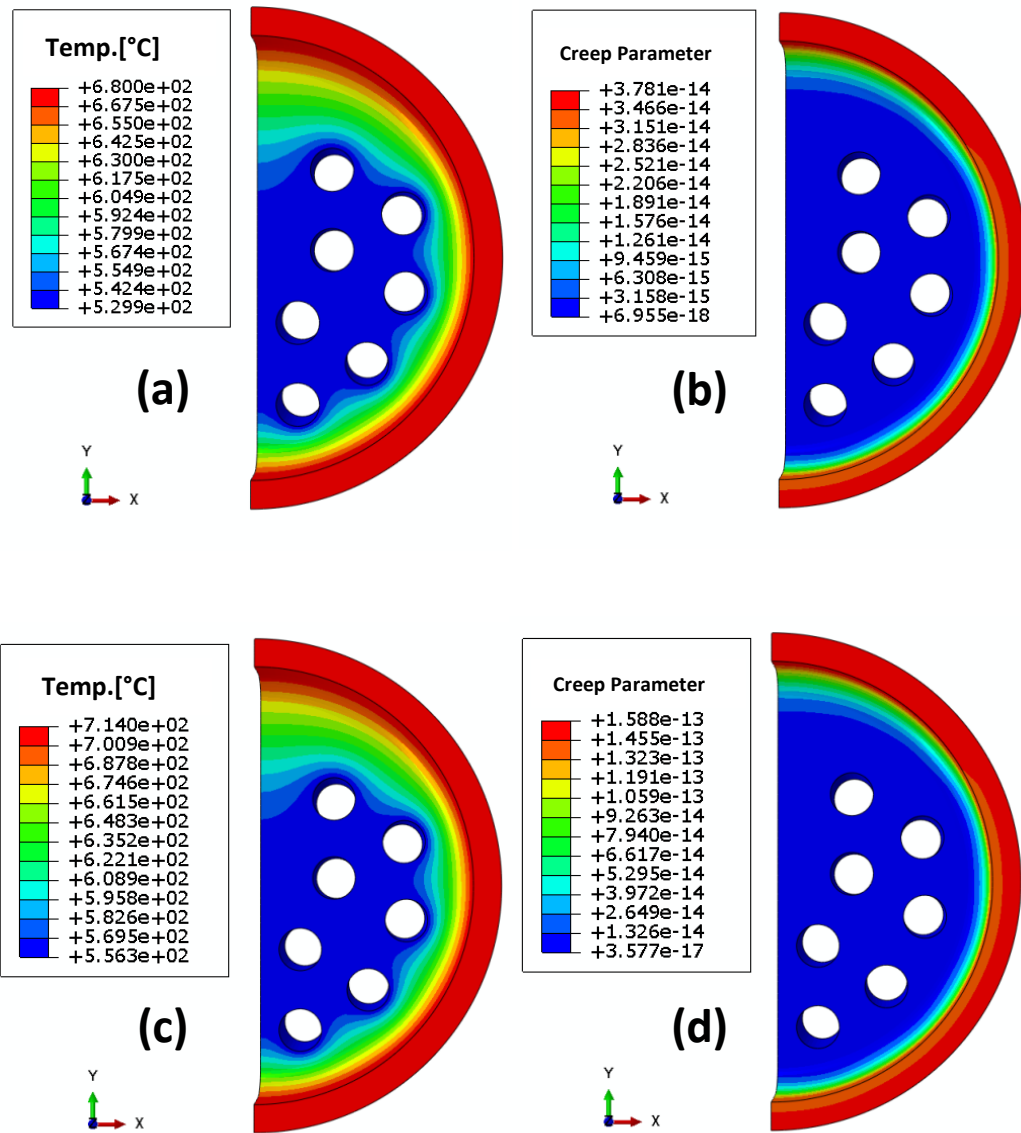


Figure 6.8 (a) Temperature distribution at the 1st dwell, (b) non-isothermal creep parameters at the 1st dwell, (c) temperature distribution at the 2nd dwell, and (d) non-isothermal creep parameters at the 2nd dwell.

Figure 6.9 shows equivalent stress contours at steady cyclic state for each load instance. For the 1st loading instance, the maximum equivalent stress with yielding occurs at the holed area of tube. In the 1st dwell, the loaded stresses relax to approximately half, and the maximum equivalent stresses occur at the inside fillet edges of the tube plate. Due to the 5% increased loading condition at the 2nd loading, the magnitude of the maximum equivalent stress increases slightly at the inside fillet edges. In the 2nd dwell, the imposed stress from the 2nd loading relaxes to around half, but the maximum equivalent stresses occur at the different location, the

tube holed area, from the 1st dwell. Finally, Figure 6.9 (e) shows the residual stress fields of the tube plate at the unloading instance.

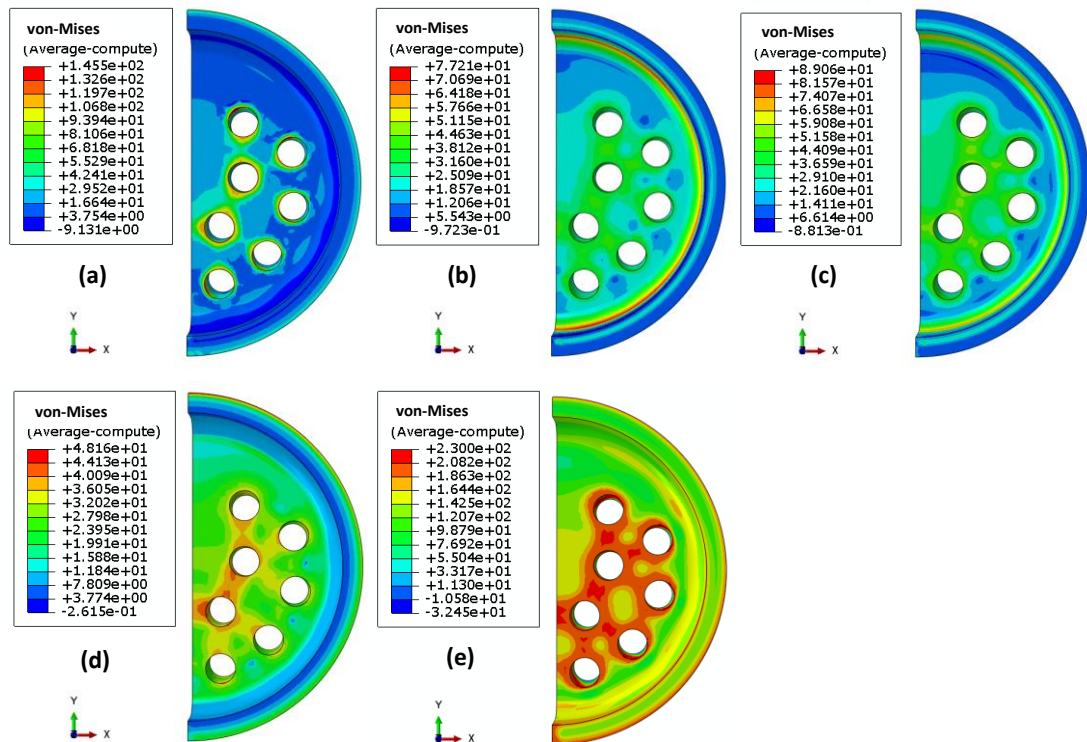


Figure 6.9 Equivalent stress distribution contours: (a) the 1st loading, (b) the 1st dwell, (c) the 2nd loading, (d) the 2nd dwell, and (e) unloading.

Figure 6.10 shows maximum effective creep strain increment at each dwell and Figure 6.11 presents stress-strain hysteresis loops for the concerning locations shown in Figure 6.10. In the 1st dwell, the maximum creep deformation occurs at the tube holed area in which the element number is 15107, and in the 2nd dwell, maximum creep deformation occurs at the top of the inside fillet edges in which element number is 2. As interesting findings, maximum creep deformation at each dwell does not occur at locations where maximum equivalent stress occurs. In the monotonic creep test under the isothermal condition, it cannot happen, but it does in the structure level. With shown hysteresis loops in Figure 6.11, the reasons will be explained.

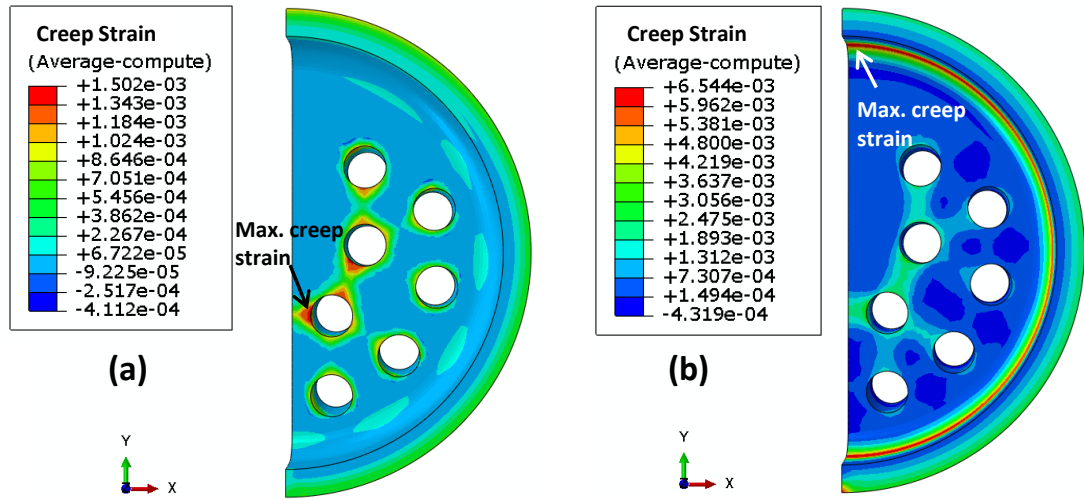


Figure 6.10 Effective creep strain increment contours at: (a) the 1st dwell (element number: 15107) and (b) the 2nd dwell (element number: 2).

For the 1st loading instance, the inside fillet edges produce quite smaller equivalent stress level than tube holed areas; thus an increase of creep stress appears during the 1st dwell. The inside fillet edges have larger creep constants than the tube holed areas due to high temperature, but the small creep stress level at the fillet edges cannot develop significant creep deformation. On the contrary, in the 2nd dwell, since the start of creep stress level at tube holed areas is similar to the fillet edges, the larger creep constant of the fillet edges develops larger creep deformation than tube holed areas.

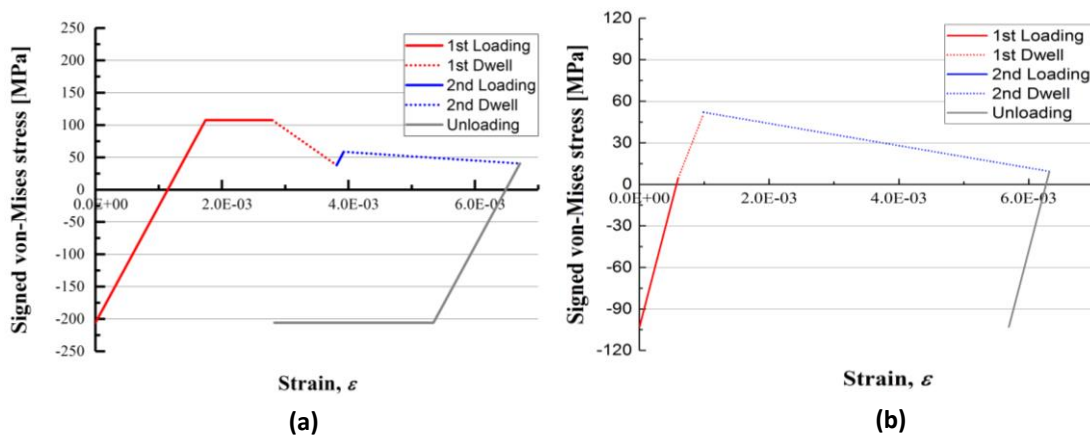


Figure 6.11 Saturated stress-strain hysteresis loops for the critical locations: (a) element 15107 and (b) element 2.

For the element 15107, significant creep stress relaxation occurs through both dwell periods, leading to considerable unloading plasticity taking place that reduces ratchetting strain increment. However, owing to no yielding over a cycle occurs at the element 2, the inside fillet edges causes larger ratchetting strain increment than tube holed areas. Both elements 15107 and 2 show creep ratchetting responses in the steady state due to cyclically enhanced creep mechanism.

As one of the improvements in the numerical technique, the modified LMM eDSCA can present stresses and creep strain histories over a dwell period. Table 6.8 shows the stresses and the creep strain histories for the element 15107 at the 2nd dwell. These relaxation histories in the stresses and the creep strain are essential data to calculate creep-fatigue damage life. In the following section, creep-fatigue damage lives based on commonly used approaches will be evaluated using those relaxation histories.

Table 6.8 Stresses and creep strain histories for the element 15107 at the 2nd dwell: creep stress $\bar{\sigma}_c$, effective creep strain $\bar{\varepsilon}^c$, principal stresses $\sigma_1, \sigma_2, \sigma_3$ and mean stress σ_m .

Dwell Time [h]	$\bar{\sigma}_c$	$\bar{\varepsilon}^c$	σ_1	σ_2	σ_3	σ_m
291	53.7	7.73E-04	23.7	-0.124	-16.41	2.4
582	50.6	1.27E-03	25.1	-0.128	-16.36	2.9
873	48.3	1.63E-03	26.2	-0.131	-16.33	3.2
1164	46.6	1.91E-03	27.0	-0.134	-16.31	3.5
1455	45.2	2.14E-03	27.7	-0.136	-16.29	3.8
1746	44.0	2.34E-03	28.3	-0.137	-16.27	4.0
2037	42.9	2.50E-03	28.8	-0.139	-16.26	4.1
2328	42.0	2.64E-03	29.2	-0.14	-16.24	4.3
2619	41.2	2.77E-03	29.5	-0.141	-16.23	4.4
2910	40.5	2.88E-03	29.9	-0.142	-16.22	4.5

6.4.2. Creep-fatigue damage endurance

The aim of this Section 6.4.2 is not to provide a solid conclusion with respect to the selection of damage model. It instead discusses damage lives based on different damage models and utilises the modified LMM eDSCA code for the evaluation of creep-fatigue damages. In this section, TF, DE, and SEDE methods are employed involving multi-axial ductility factors for creep damage calculations. ASME NH and RCC-MRx codes adopt TF method, and instead R5 procedures employ DE method for creep damage evaluation. The fatigue damage is evaluated by using MUSM shown in Eq.(6.3) and the Design Fatigue Curve of 316 stainless steel provided in ASME NH.

Figure 6.12 and Figure 6.13 present creep damage per cycle in the steady state for each dwell respectively. Calculated creep damage lives based on the three methods are summarised in . TF method causes maximum creep damage to the inside fillet edge and the outside of the tube plate, where is exposed to the higher temperature, at each dwell respectively, but the concerning areas with considerable creep damage are in compressive stresses. As shown maximum principal stress σ_1 contours in Figure 6.14, compressive stresses are dominant at high temperature areas for both dwell periods. It should be highlighted that the modified LMM eDSCA can produce maximum principal stress history over the dwell period, which can calculate more accurate creep damage under multiaxial stress state.

According to ASME NH [11], creep damage under compressive and multiaxial states of stresses is calculated using Eq.(6.4). Creep damage life for TF method is calculated with regard to a critical element 5670 which shows the maximum creep damage per cycle within a cycle. TF method is designed to calculate the creep damage from dwell time over creep rupture time at temperature. It is reasonable to see that the maximum creep damage occurs at the higher temperature side in which it has the shorter creep rupture time. Consequently, the tube holed area which has lower temperature than the outside of the tube plate shows smaller creep damage.

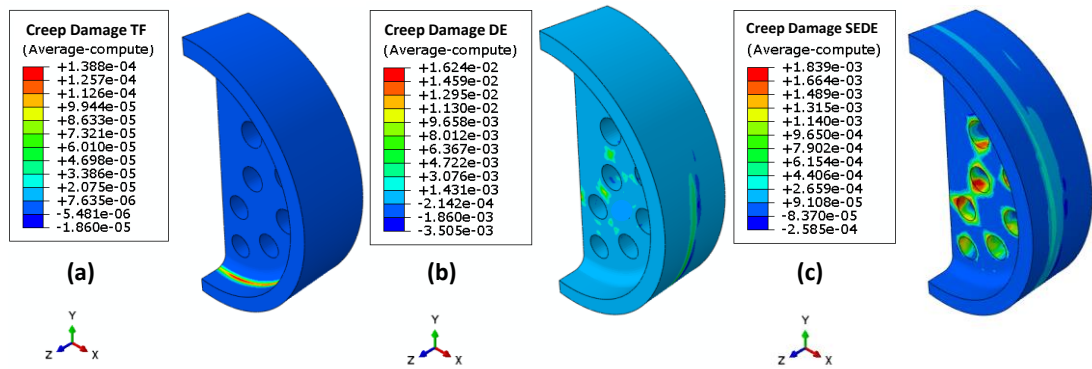


Figure 6.12 Creep damage contours at the 1st dwell: (a) TF model with σ_{RUP} , (b) DE model with MDF, and (c) SEDE model with MDF_{WEN}.

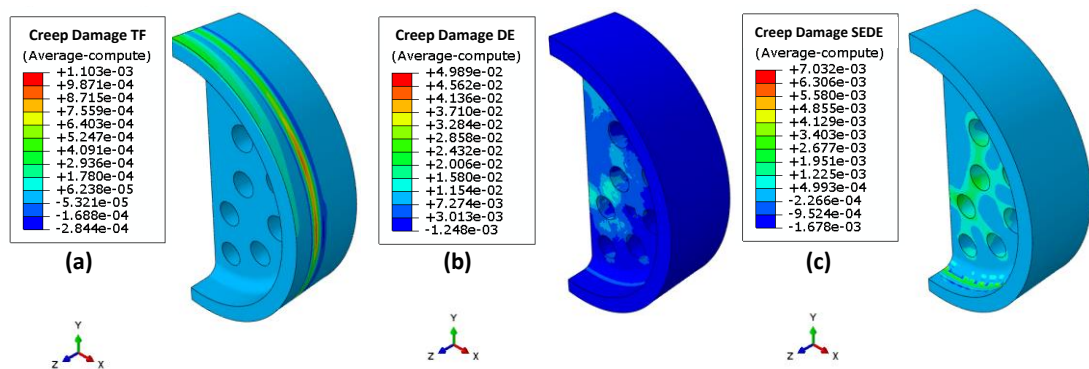


Figure 6.13 Creep damage contours at the 2nd dwell: (a) TF model with σ_{RUP} , (b) DE model with MDF, and (c) SEDE model with MDF_{WEN}.

It is observed that the maximum creep damage occurs at the element of 15107 for both DE and SEDE models. In reference to Figure 6.14, the element 15107 is imposed maximum tensile principal stresses during both dwell periods. With regard to compressive dwell, the R5 states that the upper shelf uniaxial creep ductility is used to estimate creep damage[12]. Spindler suggested the Stress Modified Ductility Exhaustion method from that creep damage under compressive dwell should be negligible based on creep cavitation mechanism where creep cavities neither nucleates nor grows under compressive stresses[40]. For compressive dwell in both DE and SEDE methods, it is assumed that the creep damage is negligible and the assumption has been implemented into the modified LMM eDSCA. Although the inside fillet edges show the maximum equivalent creep deformation in the 2nd dwell, they are in compressive stress; thus the element 2 is considered as zero damage as shown in .

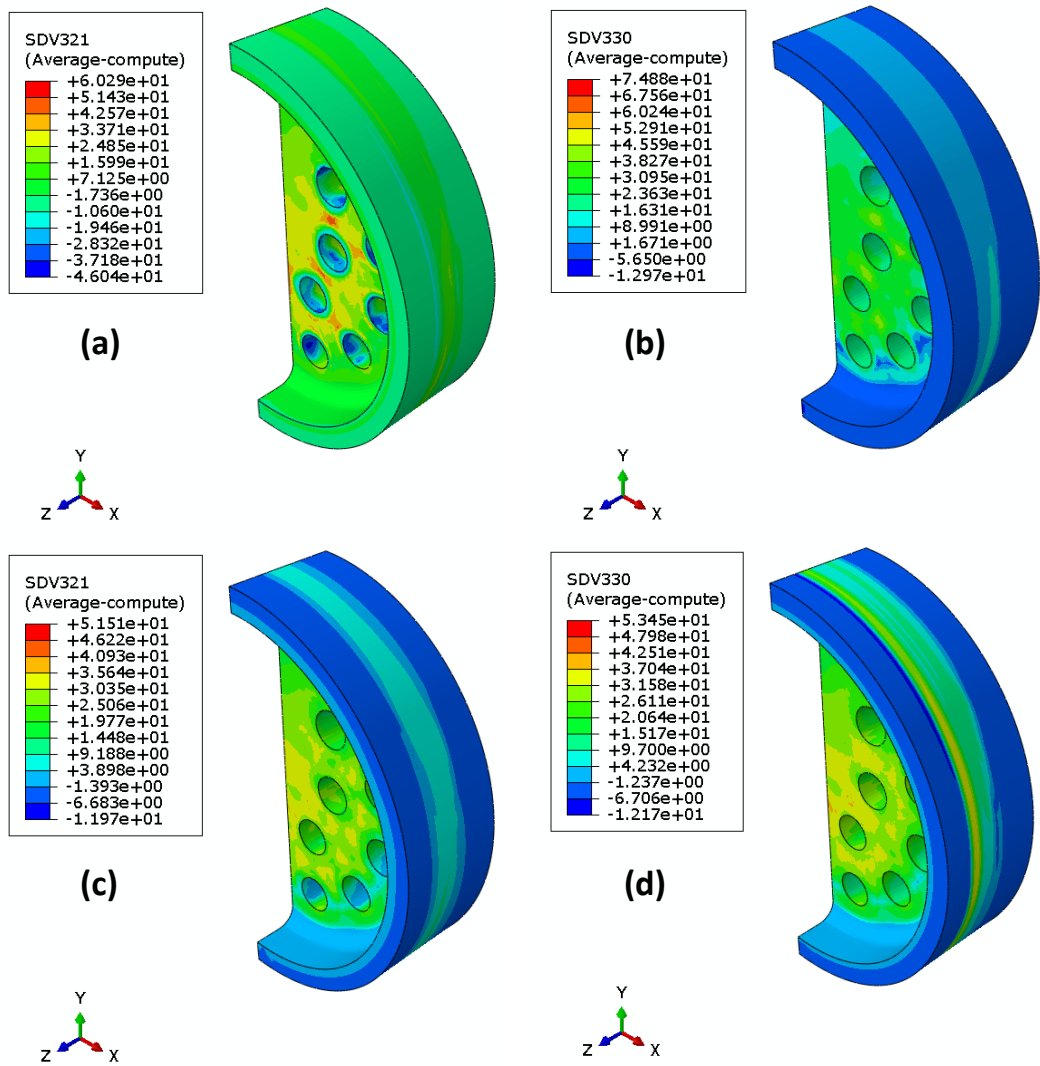


Figure 6.14 Maximum principal stress contours at dwell periods: (a) start of the 1st dwell, (b) end of the 1st dwell, (c) start of the 2nd dwell, and (d) end of the 2nd dwell.

It is worth to know that both DE and SEDE methods have an arithmetically identical form, which can convert between SEDE and DE by merely multiplying by or dividing by stress. Thus both DE and SEDE methods show that substantial creep damages occur at the holed areas of tube in which it exhibits large creep deformation as shown in Figure 6.10. Among the three methods, creep damage per cycle is getting smaller in the order of DE, SEDE, and TF.

Figure 6.15 shows contours of total strain range and fatigue damage per cycle calculated by Eq.(6.3). The equivalent total strain range and the fatigue damages for the critical locations are listed in . In the consideration of the sign of the maximum principal stresses, the fillet edges are associated with the compressive deformation, but the tube holed areas induce tensile

deformation. Both critical locations have different effects of mean stress on the fatigue life. It is known that the negative stress ratio affects less fatigue damage than the positive stress ratio according to the high-cycle fatigue test of TYPE 316L stainless steel [101]. However, ASME NH gives guidance to evaluate the low cycle fatigue damage using equivalent strain range and provides design fatigue curves for several materials.

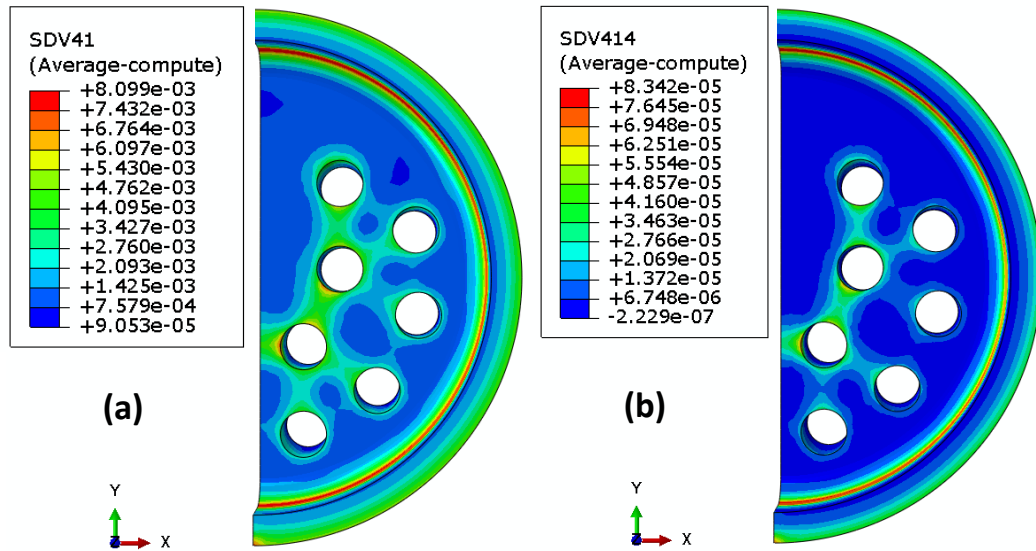


Figure 6.15 (a) Total strain range and (b) fatigue damage per cycle.

Figure 6.16 is the Design Fatigue Curve for 316 stainless steel provided in ASME NH which allows to evaluate a number of cycles to fatigue failure d_f^{ASME} against the total strain range ϵ_t concerning the specific temperature. The total strain range ϵ_t in Figure 6.16 is replaced with $\Delta\bar{\epsilon}_{Total}$, which is the maximum equivalent strain range including equivalent plastic strain and creep strain increments. The evaluated fatigue damage per cycle based on MUSM is not significant, whereas the fatigue damage on the Design Fatigue Curve is considerable for both the critical elements 15107 and 2.

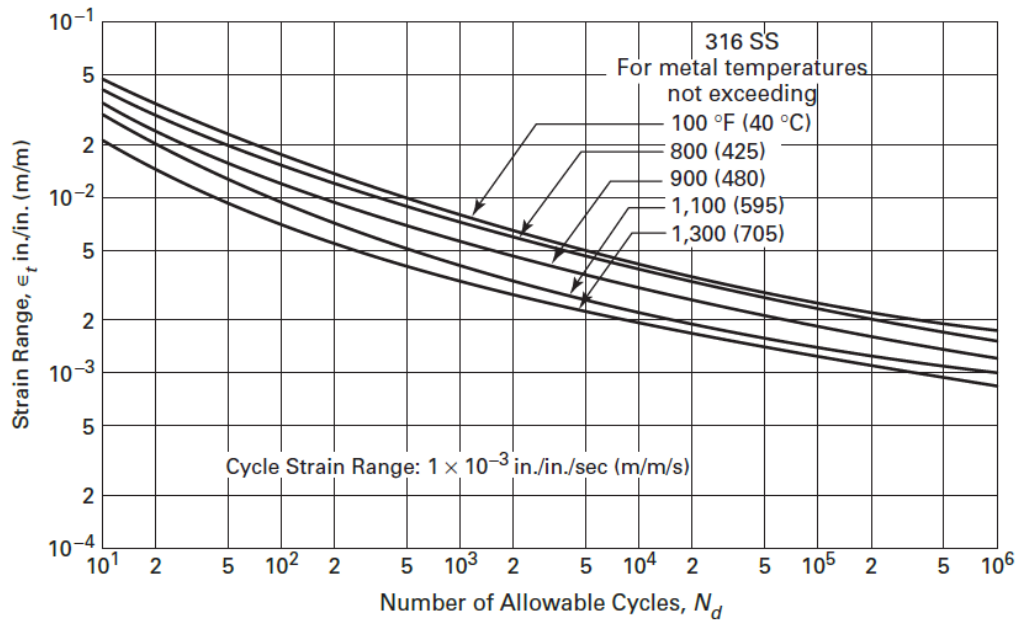


Figure 6.16 Design fatigue curve $\Delta\varepsilon - N_d$ for 316 stainless steel in ASME NH[11].

Figure 6.17 shows total damage contours for TF, DE, and SEDE methods. Calculated total damages for the dwell period of six months operation are listed in . Total damage per cycle d_{Total} is calculated from the summation of both creep damages (d_c^{1st} and d_c^{2nd}) and fatigue damage d_f .

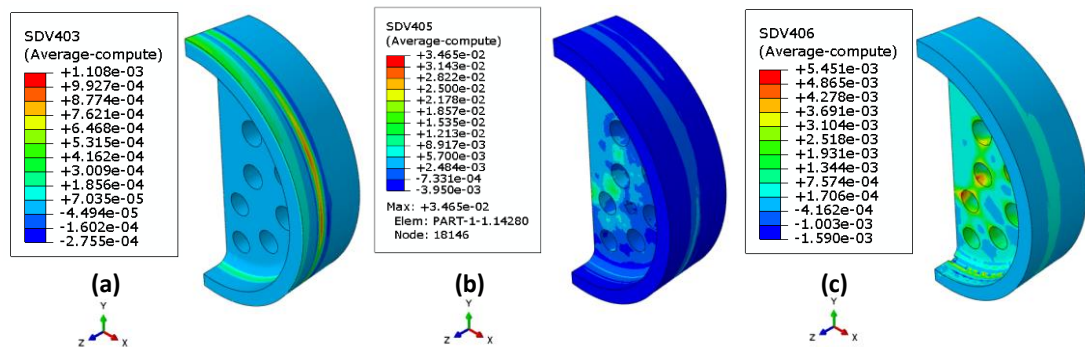


Figure 6.17 Total damage per cycle: (a) TF model with σ_{RUP} , (b) DE model with MDF, and (c) SEDE model with MDF_{WEN} .

Where fatigue damage is evaluated for elements 5670 and 15107 based on MUSM, total damage per cycle d_{Total}^{MUSM} for all three methods are similar with the creep damage contours shown in Figure 6.13, due to dominant creep damage accumulation over a cycle. It means that creep damage is the dominant failure mechanism, particularly creep deformation at the 2nd

dwelling makes considerable impact on the integrity of the tube plate. When the fatigue damage is calculated based on the ASME NH for the same elements, total damage per cycle d_{Total}^{ASME} gets more influences from the fatigue damage than the creep damage using the SEDE method. However, for the element 2, fatigue damage is the dominant failure mechanism due to the compressive dwell that causes no creep damage. The total damage is significant in the same order of the creep damages.

Table 6.9 Comparisons of creep-fatigue damage lives for six months operation.

Creep Damage per Cycle						
Element No.	5670	15107			2	
Model	TF σ_{RUP}	DE MDF	DE MDF _{WEN}	SEDE MDF _{WEN}	DE MDF	SEDE MDF _{WEN}
d_c^{1st}	6.11E-09	8.8E-04	3.8E-03	1.7E-03	0	0
d_c^{2nd}	5.1E-04	9.2E-03	2.3E-02	2.5E-03	0	0

Fatigue Damage per Cycle						
Element No.	5670	15107		2		
$\Delta\bar{\epsilon}_{Total}$	1.48E-03	6.8E-03		6.3E-03		
Model	MUSM	ASME	MUSM	ASME	MUSM	ASME
d_f	6.33E-06	<5E-05	6.5E-05	8.4E-03	6.1E-05	6.6E-03

Total Damage per Cycle						
Element No.	5670	15107			2	
Model	TF σ_{RUP}	DE MDF	DE MDF _{WEN}	SEDE MDF _{WEN}	DE MDF	SEDE MDF _{WEN}
d_{Total}^{MUSM}	5.2E-04	0.01	0.026	0.0043	6.1E-05	6.1E-05
d_{Total}^{ASME}	5.6E-04	0.018	0.035	0.0126	6.6E-03	6.6E-03
$d_{Total}^{unified}$	9.44E-06	1.0E-4			9.67E-05	

Takahashi *et al.* reported creep-fatigue damage lives for various alloys using the three creep damage evaluation methods [41]. According to the experimental results of Type 316 stainless steel, TF model is likely to predict non-conservative total damage at small strain ranges $\Delta\bar{\epsilon}_{Total} < 0.7\%$, but DE model predicts overly conservative total damage for the small total strain ranges. SEDE method shows the best predictability over tested strain range between 0.4% and 2%, among these three methods.

The two multiaxial ductility factors, MDF and MDF_{WEN} , are adopted for DE method in creep damage evaluations; DE with MDF_{WEN} predicts more considerable creep damage than DE with MDF. The results do not conclude which MDF model predicts more accurate creep damage, but it can provide a tendency that affects the creep damage. Although many factors may influence the total damage evaluations, the predicted total damages shown in present the same tendency as the experimental results. The unified creep-fatigue equation predicts total damage per cycle $d_{Total}^{unified}$ the smallest for elements 5670 and 15107, among the three methods. For the element 2, although $d_{Total}^{unified}$ is more abundant than d_{Total}^{MUSM} , the damage level is small to be negligible. Moreover, the unified creep-fatigue equation was derived based on uniaxial tensile creep rupture data, which might not be suitable to predict total damage life involving either compressive dwell or multiaxial stress state.

With the most conservative approach, the allowable operation cycle of the tube plate evaluated by DE with MDF_{WEN} and the Design Fatigue Curve is 20 cycles which is ten years operation according to the creep-fatigue damage envelope for Type 316 stainless steel in ASME NH design codes as shown in Figure 6.6. It should be mentioned that the service life is only referenced lifetime estimated for this research purpose, but it could be longer if it uses more accurate experimental data.

6.5 Chapter Summary

Creep-cyclic plasticity of a superheater outlet tube plate subjected to thermo-mechanical load is analysed through the modified LMM eDSCA which is capable of considering non-isothermal creep effects, multiple dwell periods, and dwell relaxation history in stress and strain. Temperature-dependent material properties are employed to calculate more practicable structural behaviour and lifetime prediction. The main results obtained from this work are summarised as below:

In the steady cyclic state, the tube plate has thermal stresses dominated under the thermo-mechanical load, resulting in compressive stresses dominated at the outside of the tube plate in which is the high temperature side and tensile stresses dominated at tube holed areas in which is the low-temperature side.

In the 1st dwell, maximum creep deformation occurs at the holed area of tube plate due to the larger magnitude of stress, whereas, in the 2nd dwell, maximum creep deformation occurs at the inside fillet edges close to the outside of the tube plate due to larger creep parameter induced by high temperature. Both the locations where the maximum creep deformation occurs show creep ratchetting response by cyclically enhanced creep. The numerical results also demonstrate that the modified LMM eDSCA can produce the effective creep stress history, principal stress history, creep strain increment history over a dwell period.

The modified LMM eDSCA is aimed to show the capability of evaluating the creep-fatigue damage with the various methods, rather than to conclude which damage model has the best predictability. For creep damage evaluation, Time Fraction (TF), Ductility Exhaustion (DE), Strain Energy Ductility Exhaustion (SEDE) methods were employed with Multiaxial Ductility Factors (MDF). Results show that the outside of the tube plate and the tube holed areas have creep dominated damage mechanism in the steady-state cycle. For fatigue damage assessment, the modified universal slope method (MUSM) and the design fatigue curve provided in ASME NH were considered. Fatigue damage per cycle is considerable when the design fatigue curve is applied, whereas negligible with MUSM. According to the linear damage summation method, the calculated total damage per cycle is decreasing in order of DE, SEDE, and TF which is the same order as creep damage per cycle. The severeness of the total damage is the same as the experimental results reported by Takahashi et al. Multiaxial ductility factor MDFWEN tends to predict more substantial creep damage than MDF provided in R5. The unified creep-fatigue equation evaluates considerably smaller total damage per cycle compared to the linear damage summation method.

Finally, this work shows that the LMM Framework has the vast potential to be applied for the practical creep-fatigue interaction assessment. From the viewpoint of numerical technique, the LMM Framework can be further expanded to other high-temperature problems by implementing other creep constitutive models or hardening models, so that it can aid in solving many complex engineering problems.

7. Advanced Numerical Investigations of a Critical Failure Mechanism at Elevated Temperature

7.1 Introduction

Failure mechanisms of high temperature have been observed from many components in industries such as power generation, aircraft gas-turbine engines, petrochemical process, and so on. The nuclear power plant industry requires a significantly high level of safety to avoid potential catastrophic disasters during operation. Moreover, a new development of future nuclear power station has started to reduce capital costs and meet increasing demands of world energy. These future nuclear power plants will have higher operational temperatures with increased efficiency, while also expected to have more material challenges [3, 6, 102].

When components such as the reactors or turbine blades are subjected to the complex cyclic loading at the high temperatures, it is difficult to understand its effect on creep stress behaviours in association with the variation of creep strains during a creep dwell. Moreover, if the cyclic loading is in non-isothermal condition, it can result in more complicated behaviours of the stress relaxation due to the fact that the components are imposed by internal stresses either tensile stress or compressive stress [103]. This complicated stress relaxation has critical effects on the creep-fatigue damage [104, 105]. Therefore assessment of the stress relaxation and creep strain evolution within a dwell is essential in order to prevent high temperature failures [106-108].

In a monotonic loading test with creep, creep strain tends to increase with an increase of dwell time, stress level, and temperature. However, in a cyclic loading test, a phenomenon of creep strain recovery can be identified after unloading due to its viscoelasticity. Effects of the creep strain recovery are generally negligible in the design analysis of steel structures [109]. Boyle and Spence [33] also have stated that the recovery effects may not be appropriate in the design of a comprehensive creep model using the simplified time and strain hardening equations. A new structural creep recovery mechanism, which is entirely different from the conventional creep recovery mechanism, will be introduced in this chapter. This structural creep recovery mechanism can occur by creep enhanced plasticity due to stress redistribution across the structure. The redistribution can take place when a point of the structure has lower stress than elsewhere on the same structure owing to creep. Thus the high stress tends to decrease, and the low stress tends to increase. This redistribution can lead to significant stress relaxation in

secondary stress until it reaches the primary stress level. If the primary stress is imposed on the structure in the opposite sign domain to the secondary stress, compressive and tensile creep strains can be developed in a sequence within a dwell, resulting in the structural creep recovery to occur. If a structure experiences this structural creep recovery mechanism, it requires additional consideration of the assessment of structural integrity. The compensated creep strain seems to reduce the risk of creep damage, whereas the creep enhanced plasticity may cause an augmentation in fatigue damage.

This study demonstrates the structural creep recovery mechanism through numerical investigations with a practical hardening model such as Chaboche model [110-112] and temperature dependent material properties. Stress-strain interaction under such cyclic thermo-mechanical loading is usually difficult to demonstrate. Therefore, for Sections 7.3.1 and 7.3.2, the critical structural behaviour is investigated based on simplified material properties such as temperature independent material parameters for a standard grade 316 stainless steel (SS316) and a creep property for Norton law. In Section 7.3.3, temperature dependent parameters for both mechanical and creep properties are used to present the structural behaviour. As a final validation, for Section 7.3.4, real elastoplastic hardening parameters are employed for loading and unloading and Norton-Bailey law used as constitutive creep equation.

The aims of considering different material models and properties in different sections are to have a better and easier understanding and discussion of obtained numerical results, and also to verify the robustness of identified mechanisms under different material models. In the present thesis, the influence of the structural creep recovery mechanism on structural integrity is discussed, through a benchmark example of a holed plate. This research also proposes few suggestions to improve current procedures which have been used for prediction of creep strain increment and assessment of creep-fatigue damage, if the structural creep recovery mechanism occurs.

7.2 Problem Description and the Finite Element Model

7.2.1 Geometry and Loadings for the Analysis

A benchmarked problem of a holed plate is used to show the structural creep recovery mechanism. The geometry of the structure and a quarter FE meshed model are depicted in Figure 7.1. The plate has a ratio of 0.2 between diameter (D) of the hole and length (L). The thickness of the plate has a ratio of 0.05 to the length (L). The mechanical tensile load (σ_p) acts along the horizontal axis, and the thermal load applies to the plate as a temperature difference between the inner surface of the hole θ and the outside surface of the plate θ_0 . Figure 7.2 depicts the two different loading scenarios acting on the plate at the same time. The temperature at the inner surface of the hole $\theta(t)$ varies over time from θ_0 (ambient temperature assumed as 0°C) to $\theta_0 + \Delta\theta$ as a time function, and three load instances follow in order by loading (t_1), creep (Δt), and unloading (t_2).

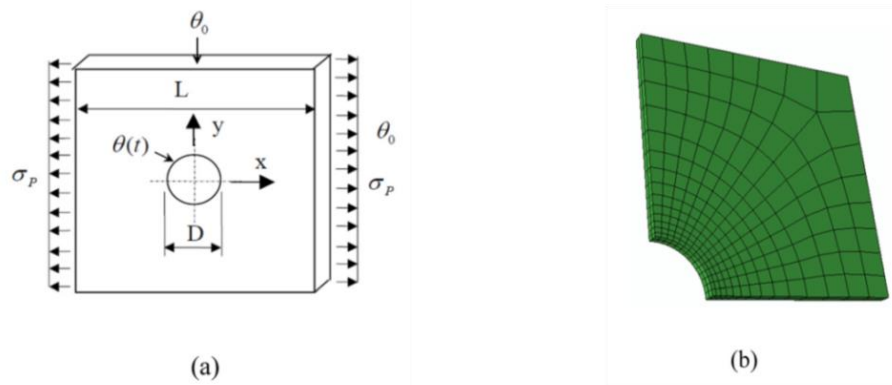


Figure 7.1 (a) Geometry of the holed plate and loading conditions and (b) FE meshed model.

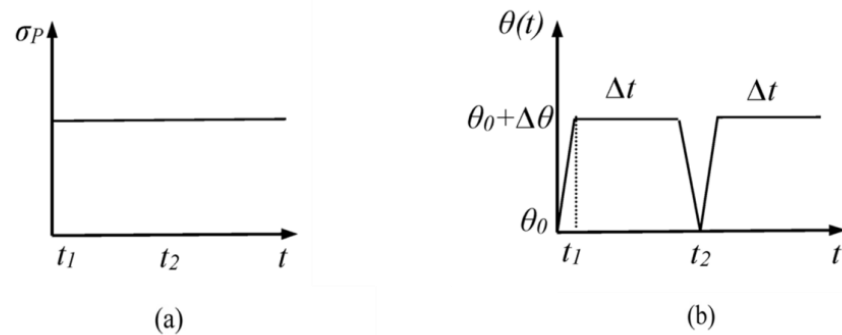


Figure 7.2 Loading instances: (a) mechanical loading and (b) thermal loading.

Figure 7.3 presents the shakedown and ratchet boundaries of the holed plate without the effect of creep by using the LMM. The mechanical and thermal loads are normalised by a reference uniaxial load $\sigma_{p0} = 100MPa$ and a reference temperature $\Delta\theta_0 = 500^\circ C$ respectively. In order to investigate the structural creep recovery mechanism, six load cases in Figure 7.3 are selected to perform incremental cyclic analyses considering full creep-cyclic plasticity interaction. It is worth noting that without the creep effect, any load cases within the reverse plasticity zone will show an alternating plasticity mechanism.

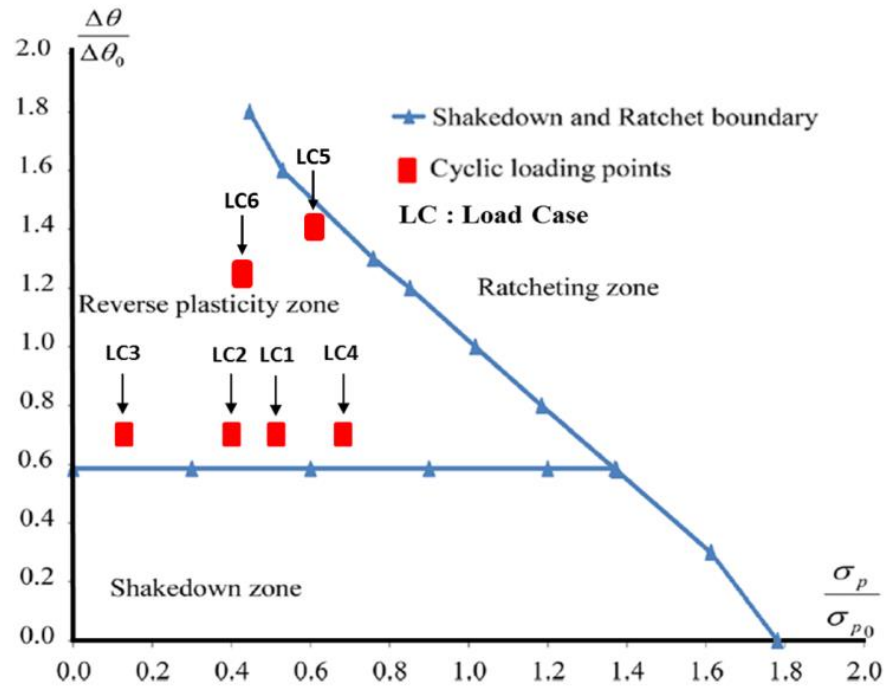


Figure 7.3 Shakedown and ratchet limit boundaries for the holed plate subjected to the thermo-mechanical loads and six load cases for investigations of the structural creep recovery mechanism.

7.2.1 Material properties and FE model

It is assumed that the plate is made of a standard grade 316(annealed condition) stainless steel (ASTM A240M) with the following mechanical properties: Young's modulus (E) = $193GPa$, temperature independent yield stress $\sigma_y = 205MPa$, and Poisson's ratio (ν) = 0.3 . An elastic-perfectly plastic material model considers for plasticity as a conservative approach to evaluating strains accumulated by the combined cyclic load. The yield surface of the elastic-perfectly plastic model can be expressed as:

$$f = J(\hat{\sigma}) - \sigma_y = 0 \quad (7.1)$$

where f denotes the function of yield surface, $J(\hat{\sigma})$ and σ_y are invariant equivalent stress tensor and yield stress respectively. The Norton-Bailey law is widely used for predicting of creep strain deformation in the tensile creep test, but some studies are reporting compressive dwell with the same power law [113, 114]. Therefore, creep deformation in the present work is assumed to follow the Norton-Bailey equation within either tensile or compressive dwells:

$$\dot{\bar{\epsilon}}^c = A\bar{\sigma}^n t^m \quad (7.2)$$

where $\dot{\bar{\epsilon}}^c$ denotes the equivalent creep strain rate; $\bar{\sigma}$ is the effective von-Mises stress; t is the dwell time; and A , n , and m are temperature dependent material constants of creep. To simplify the analyses, following creep material constants are assumed: $A = 5.86 \times 10^{-15} [MPa^{-1}h^{-1}]$ at the temperature of $500^\circ C$, $n = 5$ as a typical value for austenitic steel $m = 0$ so that the Norton-Bailey law is transformed to simple Norton's law.

For a quarter model of the plate, twenty-node quadratic hexahedral elements are used with reduced integrations (C3D20R). The mesh size and its quality are assessed, which confirms less than 1% resultant stress and strain deviations as the number of mesh increase up to 50%. Symmetry boundary conditions are applied, and outer surfaces of the plate are constrained to maintain a plane condition. In order to implement the thermal gradient, the adiabatic condition applies to the outer surfaces of the plate. Figure 7.2(a) shows that the temperature difference $\Delta\theta_0 = 500^\circ C$ between the centre hole and the outer surfaces, and the mechanical load $\sigma_p = 100MPa$ imposed. The thermal conductivity of $25.2 [W \cdot m^{-1}K^{-1}]$ and the expansion coefficient of $1.75 \times 10^{-5} [^\circ C^{-1}]$ are applied. In order to evaluate structural response at the steady cyclic state, step-by-step (SBS) analysis is performed using commercial software Abaqus. For the SBS analysis, sixty individual load steps are created, which is in total twenty cycles of three load steps corresponding to loading, creep, unloading respectively.

7.3 Results and Parametric Studies

7.3.1 Investigation of the Structural Creep Recovery Mechanism

An SBS analysis is performed to account for the structural creep recovery mechanism with load case 1 ($\Delta\theta = 0.7\Delta\theta_0$ and $\sigma_p = 0.5\sigma_{p0}$) for a dwell time of 200hrs. Figure 7.4 depicts von-Mises stress distributions for each load instance, and effective creep strain increment at creep dwell. Figure 7.4 (a) shows the equivalent stress distribution during the loading instance. Within creep instance, the equivalent stresses relax significantly as shown in Figure 7.4 (b) due to the creep stress redistribution. Figure 7.4 (c) shows the stresses re-distributed across the holed plate after unloading, and critical locations where are the holed area become yield due to reverse plasticity taking place during unloading. The maximum stress is imposed on the centre holed area at the loading instance, and then it shifts to the top of the hole at the creep instance. Consequently, in Figure 7.4 (d), maximum creep strain occurs at the critical location, where the maximum stresses take place.

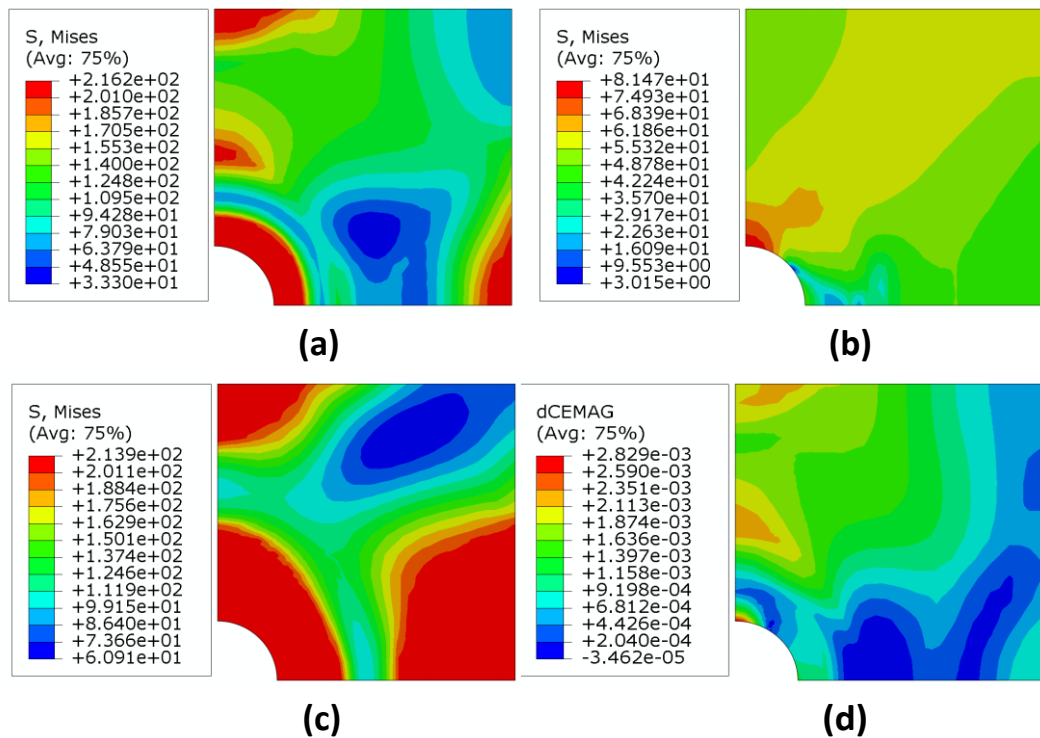


Figure 7.4 von-Mises stress distribution at load case 1 for dwell time of 200hrs at the last loading cycle: (a) loading, (b) creep, (c) unloading, and (d) corresponding creep strain increment.

An element at the top of the holed area where shows both the maximum equivalent stress and creep strain increment is selected as a point of interest to understand the structural response of the plate, and further investigations are carried out. Figure 7.5 illustrates curves of the creep stress relaxation and the creep strain increment against the dwell time with respect to the point of interest.

Figure 7.5 presents the significant creep stress relaxation with the signed von-Mises stress. The stress relaxes from -205MPa to 80MPa during the dwell period. Mason et al. introduced the Rule of Sign for the *Dominant Principal Direction*. This rule suggests that the sign of the equivalent stress and strain is determined based on the dominant principal direction [115]. An investigation is carried out to select which principal stress component ($\sigma_1, \sigma_2, \sigma_3$) dominates each load instance; And in this section for the holed plate the maximum principal stress shows the most considerable stress magnitude among the three principal components within a cycle. Hence, the algebraic sign of the von-Mises stress is determined by the sign of the maximum principal stress.

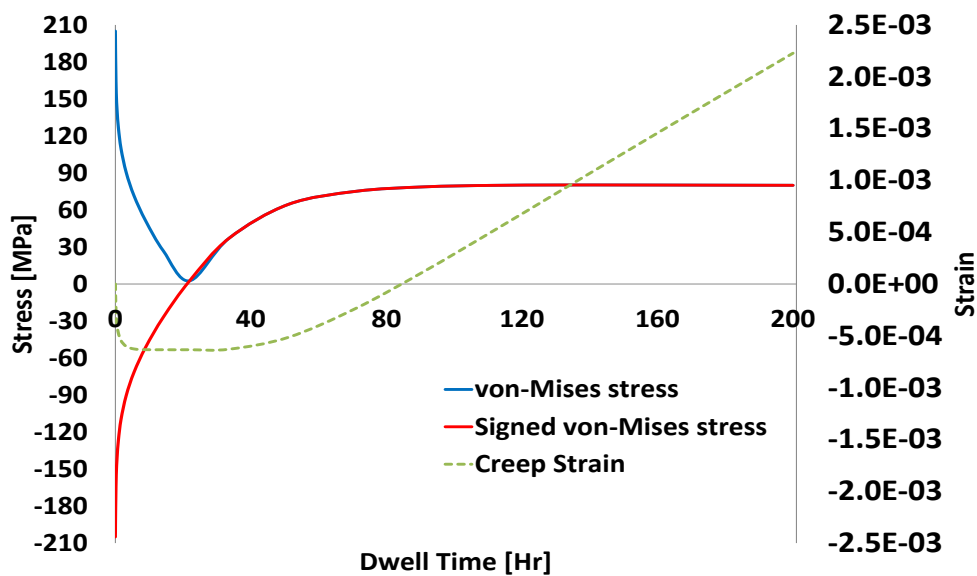


Figure 7.5 Creep stress relaxation curves and creep strain increment with load case 1 for a dwell time of 200hrs at the point of interest.

Further investigation shows that the stress component σ_{11} dominates the maximum principal stress σ_1 . Figure 7.6 demonstrates that the σ_{11} has similar stress values and the same algebraic sign with the signed von-Mises stress history which are summarised in Table 7.1. Based on

the observation, it can be deduced that σ_{11} may have a critical effect on the structural creep recovery mechanism as a dominant stress component.

Table 7.1 Stress history between signed von-Mises stress and stress component

	σ_{11}		
Stress	Loading	Creep	Unloading
Signed von-Mises	-205	79.7	205
σ_{11}	-206.2	79.3	202.1

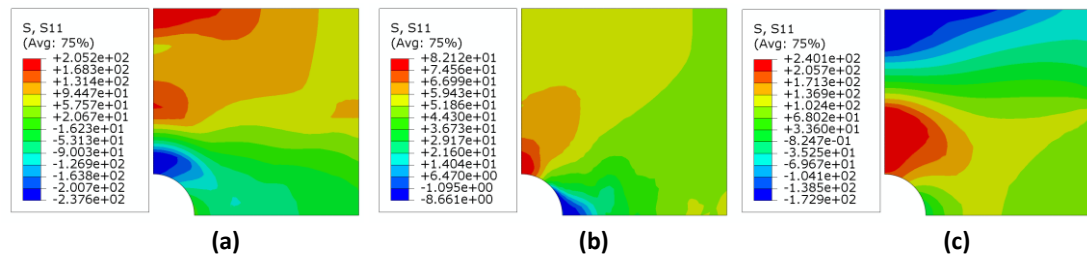


Figure 7.6 Stress component σ_{11} distributions for each load instance with load case 1 for dwell time of 200hrs: (a) loading, (b) creep, (c) unloading.

The structural creep recovery mechanism is identified with the creep strain curve shown in Figure 7.5. The creep strain increases rapidly with compressive creep stress during very early dwell stage. The creep strain increases rapidly with compressive creep stress during very early dwell stage. However, no more compressive creep strain increases as the creep stress relax up to 40MPa, afterwards, tensile creep strain begins to grow until the end of dwell time. While the tensile creep strain increases, the previous compressive creep strains fully recover during the dwell time of approximately 80hrs.

As shown the signed von-Mises stress history, the relaxation keeps the creep stress increased until it reaches the steady state in the tensile stress domain during the creep dwell. This phenomenon does not usually occur in the case of pure thermal creep stress relaxation. However, it could occur when the assessment point has a lower stress level than the primary stress level, known as the rupture reference stress, as a process of the creep stress redistribution. R5 volume 2/3 Appendix A3 [104] also reports these cases. Due to the primary tensile stress, the compressive dwell changes to tensile, otherwise the magnitude of the creep strain rate would remain nearly zero if insufficient primary tensile stress applied. Therefore, it demonstrates that the structural creep recovery phenomenon within a single dwell is due to the

creep stress redistribution, and it is named here as the *Structural Creep Recovery Mechanism* in this thesis.

During a dwell, the stress redistribution causes the significant stress relaxation of the point of interest. Figure 7.7 shows the linear elastic solution of each thermal stress and mechanical stress for load case 1. The point of interest at the top of the hole has imposed internal stresses consisting of thermally induced compressive stress and tensile mechanical stress at loading. Both internal stresses apply in the opposite direction, and their magnitudes of thermal stresses are more than five times the mechanical stresses. The secondary compressive stress dominates the primary tensile stress at loading. The secondary stress relaxes significantly during the creep dwell, which results in the primary stress becoming dominant internal stress, acting in the opposite direction to the secondary stress.

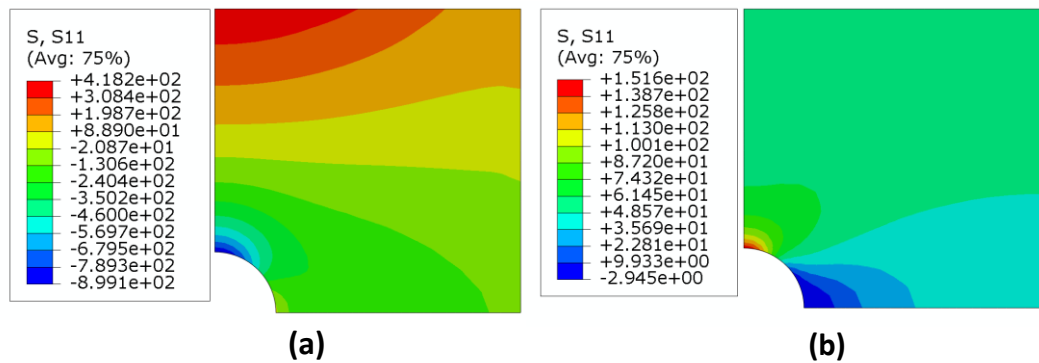


Figure 7.7 Elastic stress solutions: (a) stress component σ_{11} from monotonic thermal gradient only with $\Delta\theta=0.7$ and (b) stress component σ_{11} from monotonic mechanical load only with $\sigma_p=0.5 \sigma_{p0}$.

Simultaneously, the creep strain grows with the dominant internal stresses, resulting in the creep strain recovery occurring within the dwell. Figure 7.8 illustrates the creep-cyclic plasticity response of the plate as a saturated-state of the stress-strain cycles, where ϵ is strain increment; subscription of L, BR, R, U denotes loading, before recovery, recovery, and unloading respectively, and superscription of e, c, p denotes elastic, creep, and plastic respectively.

The structural creep recovery mechanism is also clearly distinguished in the hysteresis loop within the creep dwell. As noted earlier, the growth rate of the creep strain in the relaxation from $-50MPa$ to $40MPa$ becomes a steady-state. In the steady-state, it does not evolve any

significant creep strain increment, because it is attributed to a tiny creep strain increment due to the small magnitude of creep stresses with the corresponding dwell time increment.

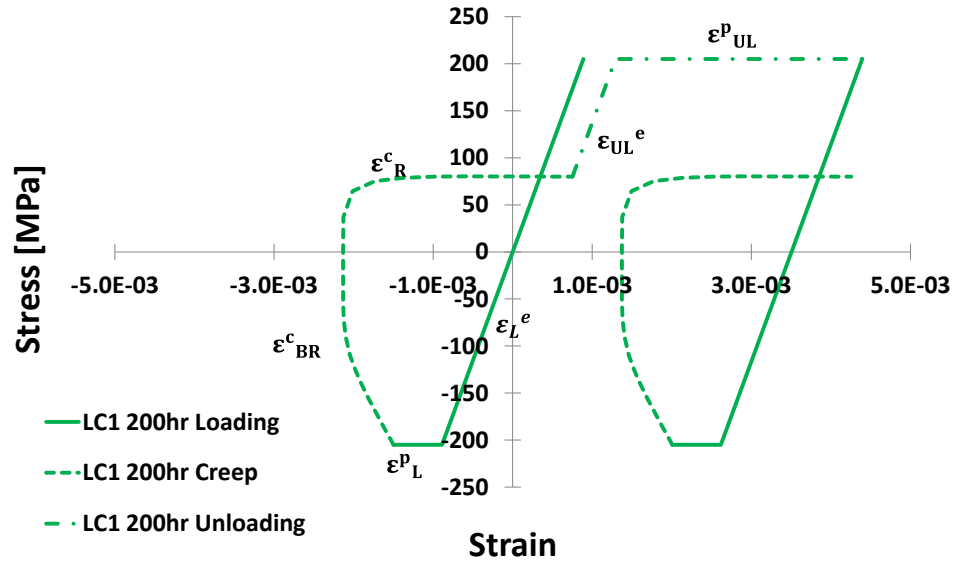


Figure 7.8 Response of steady state stress-strain hysteresis loop corresponding to load case 1 for a dwell time of 200hrs.

From these results, it is confirmed that the structural creep recovery mechanism can be induced by the creep stress redistribution which causes the change of the dominant internal stresses within a creep dwell. Besides, it should be noted that the substantial creep stress relaxation accelerates the creep enhanced plasticity, which increases unloading plasticity, eventually leading to creep-ratchetting with every cycle. In order to fully understand the structural creep recovery mechanism, the effects of varying dwell time and mechanical load level on the structural creep recovery mechanism will be analysed in the following parametric studies.

7.3.2 Effect of Dwell Time and Load Level on the Structural Creep Recovery Mechanism

The SBS analyses are performed to understand the effects of dwell time on the structural creep recovery mechanism with load case 1 for a different dwell time of 10hrs, 50hrs, 100hrs, and 200hrs each. Although the maximum creep strain occurs in different elements for different dwell time, the identical element to the point of interest is investigated since the concerning element shows the maximum inelastic strain increment from all the simulations. Concerning the point of interest, the analysis results are summarised in Table 7.2, where $\bar{\sigma}_s [MPa]$ and $\bar{\sigma}_c [MPa]$ are the start of creep stress and the end of creep stress respectively; t and t_s are dwell time [hr] and dwell time for the structural creep recovery to occur respectively. C.S.R is

an abbreviation for the Creep Strain Recovery, and negative signs of values in Table 7.2 represent the compressive stress or strain. Figure 7.9 depicts the hysteresis loops at steady-state for the dwell time of 100hrs and 200hrs each.

Table 7.2 Comparison of critical values and features with load case 1 for different dwell time.

t	$\bar{\sigma}_s$	$\bar{\sigma}_c$	ε_{BR}^c	ε_R^c	ε_L^P	ε_U^P	t_s	C.S.R
10	-205	-42.86	-6.56E-04	-	-6.10E-04	2.23E-03	-	N
50	-205	68.33	-6.34E-04	8.78E-05	-6.11E-04	3.51E-03	20 ~ 25	Y
100	-205	80.56	-6.35E-04	9.26E-04	-6.11E-04	3.48E-03	20 ~ 21	Y
200	-205	79.94	-6.34E-04	2.88E-03	-6.10E-04	3.10E-03	20 ~ 21	Y

Table 7.2 shows that the structural creep recovery starts at the approximate time of 20hrs. Hence, the structural creep recovery mechanism does not occur within the dwell time of 10hrs. For a dwell time of 50hrs, the compressive creep strain is still more substantial than the tensile creep strain. However, for a dwell time of 100hrs, the tensile creep strain exceeds the compressive creep strain, resulting in the creep damage to be taken into account. For a dwell time of 200hrs, more tensile creep strain develops than 100 hrs. From this investigation, it can be deduced that the dwell time may have effects on creep damage, provided that total dwell time t is longer than t_s . However, plastic strain increment at unloading remains a more or less same if the end of creep stress reaches to the steady-state regardless dwell period.

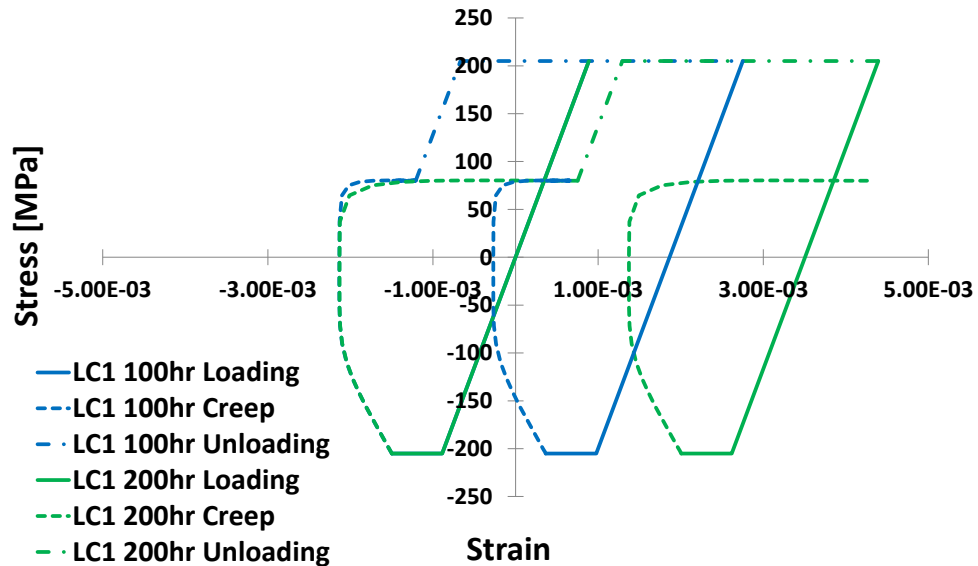


Figure 7.9 Response of steady state stress-strain loop corresponding to load case 1 for a dwell time of 100hrs and 200hrs each.

As explained in Section 7.3.1, the stress component σ_{11} affects the significant stress relaxation. In order to evaluate the effects of the dominant stress component σ_{11} on the structural creep recovery mechanism, another parametric study is carried out with varying uniaxial mechanical load level. The identical SBS analyses are performed for a dwell time of 200hrs with three individual load cases which consist of the same cyclic thermal load but the different magnitude of the constant mechanical load; LC2 ($\Delta\theta = 0.7$ and $\sigma_p = 0.4\sigma_{p0}$), LC3 ($\Delta\theta = 0.7$ and $\sigma_p = 0.1\sigma_{p0}$), and LC4 ($\Delta\theta = 0.7$ and $\sigma_p = 0.7\sigma_{p0}$) as shown in Figure 7.3.

Table 7.3 Comparison key values and feature for dwell time of 200hrs with different mechanical load cases.

LC	$\bar{\sigma}_s$	$\bar{\sigma}_c$	ε_{BR}^c	ε_R^c	ε_L^p	ε_U^p	t_s	C.S.R
1	-205	79.94	-6.34E-04	2.88E-03	-6.10E-04	3.10E-03	14 ~ 21	Y
2	-205	63.38	-7.65E-04	4.88E-04	-6.11E-04	2.98E-03	43 ~ 63	Y
3	-205	-36.86	-1.22E-03	-	-6.23E-04	1.83E-03	-	N
4	-205	112.19	-4.19E-04	1.89E-02	-6.10E-04	3.69E-03	4 ~ 7	Y

From the analysis results, the maximum creep strain occurs at the identical element to the point of interest on the three load cases. Critical values and features are listed in Table 7.3, and Figure 7.10 shows the saturated hysteresis loops for the three load cases (LC1, LC2, and LC3). Due to too large tensile creep strain, Figure 7.10 does not plot a hysteresis loop of LC4.

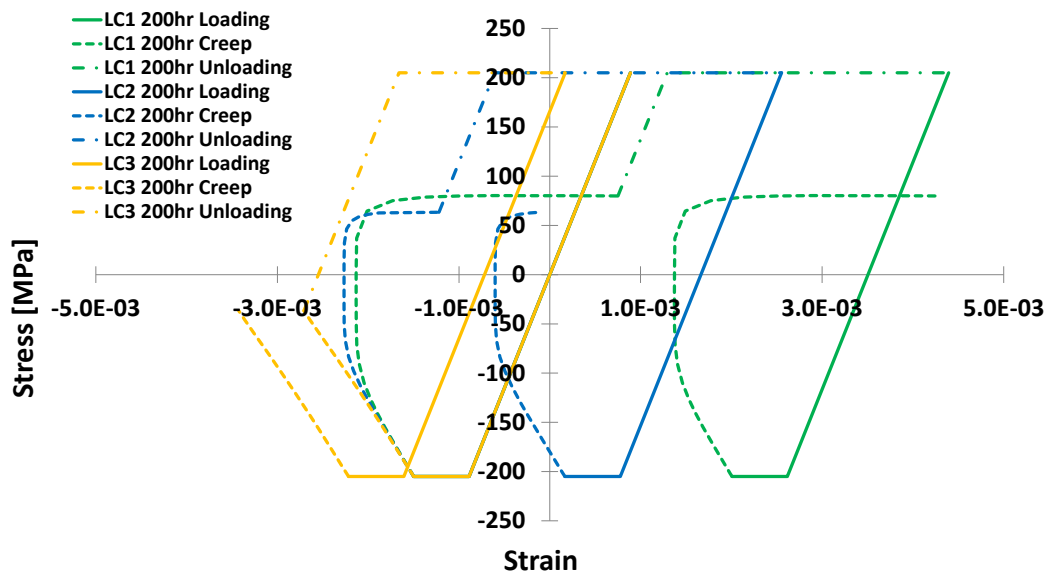


Figure 7.10 Response of steady state stress-strain loop corresponding to load cases 1, 2, and 3 for a dwell time of 200hrs.

Table 7.3 shows that the end of creep stress is likely to reduce with a decrease of the mechanical load level. In other words, a degree of stress relaxation within a creep dwell is affected by the mechanical load level. As results, compressive creep strain developed in both load cases 2 and 3 is more significant than load case 1 within dwell time t_s . The time t_s also tends to increase as the level of the mechanical load decreases. On the contrary, due to reduced tensile dwell period $(t-t_s)$ and lower level of the end of creep stress, both tensile creep strain and unloading plasticity decrease, leading to a reduction of the total strain.

Figure 7.11 illustrates the stress relaxation curves for each load case with signed von-Mises stress. It shows that a degree of stress relaxation increases with an increase of the mechanical load. The sign change of internal stresses takes place early with the larger mechanical load. Interestingly, the structural creep recovery mechanism does not appear at load case 3 for a dwell time of 200hrs. This is because the secondary stress does not relax enough in order for the primary stress to become the dominant internal stress within the dwell time of 200hrs. In the mathematical viewpoint, the secondary stresses can completely relax to zero stress in the case of the dwell time going to infinity. In other words, the structural creep recovery mechanism should appear when the primary stresses applied to the opposite direction of the secondary stresses.

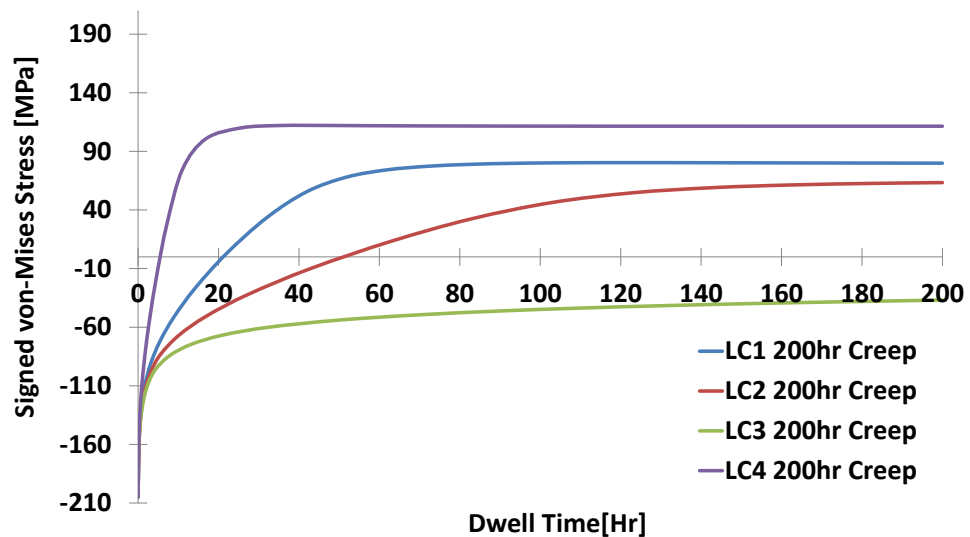


Figure 7.11 Creep stress relaxation curves for a dwell time of 200hrs per load case.

An SBS analysis is performed to verify this hypothesis with an identical load case to LC3 and extended dwell time of 60,000hrs. The analysis result confirms that the structural creep recovery mechanism occurs at a dwell time of approximately 36,000hrs as shown in Figure 7.12. From these parametric studies, it has verified that a structure can experience the structural creep recovery mechanism under the specific loading condition and dwell period. Also, variations of the tensile mechanical load have critical effects on the time t_s and magnitude of the end of creep stress, which cause an increase of a total strain range.

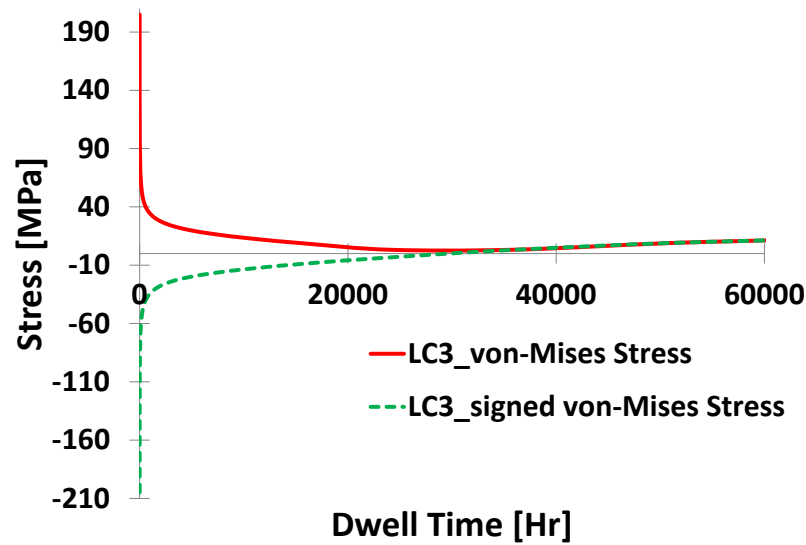


Figure 7.12 Creep stress relaxation curves in load case 3 for a dwell time of 60,000hrs.

This study has identified the structural creep recovery mechanism with the temperature independent material properties in the present section. However, the strength of materials tends to decrease in the elevated temperature, whereas nonlinear creep behaviour is enhanced. In order to verify the structural creep recovery mechanism in practice, an additional parametric study will be performed with temperature dependent material parameters in the following section.

7.3.3 Effect of Temperature Dependent Parameters on the Structural Creep Recovery Mechanism

The temperature dependent material parameters of type 316 stainless steel are listed in Table 7.4. The Norton law is transformed to implement temperature dependent creep properties as Eq.(7.3) by adopting the Arrhenius law, where A^* is a frequency factor, Q_{eng} is activation

energy [$KJ \cdot mol^{-1}$] , R_{gas} is the gas constant [$J \cdot mol^{-1} \cdot K^{-1}$] , and T represents temperature [K] in Kelvin.

$$\dot{\varepsilon}^c = A^* \cdot \exp\left(\frac{-Q_{eng}}{R_{gas} T}\right) \bar{\sigma}^n \quad (7.3)$$

The temperature dependent creep property, $A^* \cdot \exp\left(\frac{-Q_{eng}}{R_{gas} T}\right)$, in Eq.(7.3) is defined as the creep coefficient, A , in Table 7.4. In order to implement significant high temperature creep behaviour, load case 5 consisting of cyclic thermal load ($\Delta\theta = 1.4\Delta\theta_0$ and $\theta_0 = 400^\circ C$) and constant mechanical load ($\sigma_p = 0.7\sigma_{p0}$) is created. A user subroutine is created to apply the temperature dependent material properties and to calculate corresponding equivalent creep strains. An SBS analysis is performed with load case 5 for a dwell time of 200hrs.

Table 7.4 Temperature dependent material parameters and creep material constants of the SS316.

Temperature [$^\circ C$]	Yield stress [MPa]	Creep coefficient, A		
40	205	9.10E-43		
100	170	2.95E-35		
150	154	1.26E-30		
200	144	5.67E-27		
250	135	5.10E-24		
300	129	1.40E-21		
350	123	1.56E-19		
400	118	8.67E-18		
450	114	2.76E-16		
500	110	5.60E-15		
550	105	7.89E-14		
600	100	8.22E-13		
650	95	6.64E-12		
700	90	4.33E-11		
B	Q	R	n	m
46333.8	280	8.314	5	0

From the analysis results, the maximum creep strain occurs at a different element, but maximum total strain develops at the same point of interest within a steady-state cycle. Hence the same point is selected as a critical element in order to investigate structural response. The

key values and features are summarised in Table 7.5, and Figure 7.13 depicts a saturated hysteresis loop for load case 5.

Table 7.5 Key values and feature with load case 5 for dwell time of 200hr.

<i>LC</i>	$\bar{\sigma}_s$	$\bar{\sigma}_c$	ϵ_{BR}^c	ϵ_R^c	ϵ_L^P	ϵ_U^P	t_s	<i>C.S.R</i>
5	-90	17.6	-4.84E-04	1.24E-02	-1.20E-04	1.64E-03	2~3	Y

The structural creep recovery mechanism is identified as both compressive and tensile dwells develop within a dwell period. Unlike the analysis results of the temperature independent model with load case 1, the stress relaxation range reduces but the recovery occurs at an early dwell time of t_s , approximately 2.5hrs, due to stress relaxation starting from the lower magnitude of the creep stress with the larger creep coefficient. Therefore, load case 5 develops smaller compressive creep strain than load case 1. Moreover, the end of creep stress becomes a steady-state at the stress level of 17.6MPa far lower than load case 1, despite higher tensile mechanical load to be applied than load case 1. As explained in Section 7.3.1, during creep stress redistribution, compressive creep stress increases up to the primary stress which is the rupture reference stress. Hence it can be presumed that the temperature dependent model has a lower reference rupture stress value. Tensile creep strain of load case 5 is more significant than four times of load case 1 due to higher creep coefficient and longer tensile dwell within the recovery.

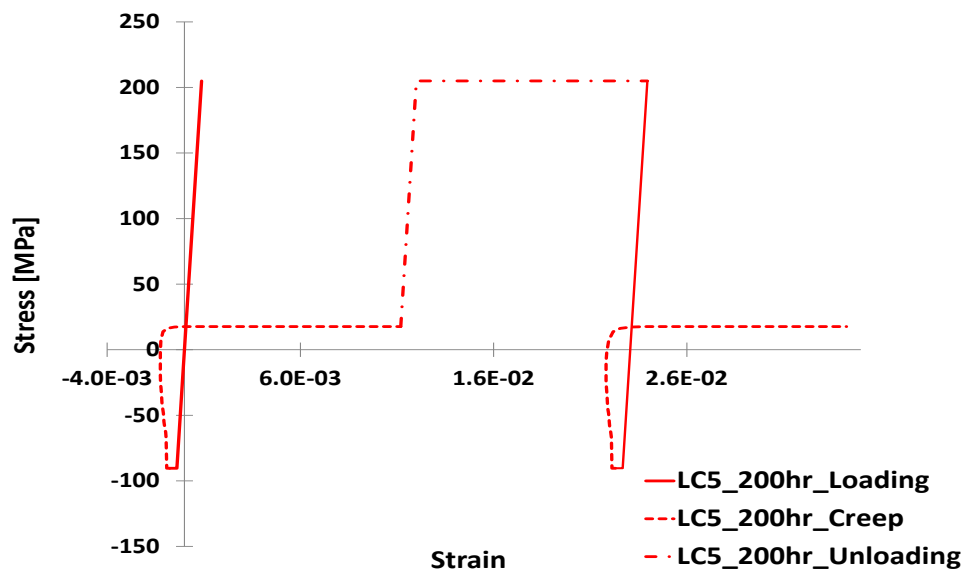


Figure 7.13 Response of steady state stress-strain loop corresponding to load case 5 for dwell time of 200hrs.

From this study, it is confirmed that the structural creep recovery mechanism requires consideration for the temperature dependent cases under the specific loading condition in the elevated temperature.

7.3.4 Effect of Practical Hardening Parameters on the Structural Creep Recovery Mechanism

In this section, the creep-cyclic plasticity of the holed plate is analysed with mechanical properties of a low carbon grade 316 stainless steel with Chaboche hardening model at 600°C. The isothermal cyclic testing data is used to validate the structural creep recovery mechanism. The test data is taken from literature [116].

For isotropic hardening, the yield surface size σ^0 is defined as the initial size of yield surface σ_y approaches to saturated constant value R which can be expressed as the maximum change in the size of the yield surface Q_∞ with an increase of equivalent plastic strain $\bar{\epsilon}^p$, and b determines a change rate of the yield surface.

$$\sigma^0 = \sigma_y + R \quad (7.4)$$

$$R = Q_\infty (1 - \exp^{-b\bar{\epsilon}^p}) \quad (7.5)$$

$$b = \frac{\ln\left(1 - \frac{R}{Q_\infty}\right)}{\bar{\epsilon}^p} \quad (7.6)$$

For kinematic hardening, the hardening law has several kinematic hardening components which are back stresses X_k ; the overall back stress X can be calculated from the summation of each back stress; where n is the number of back stress. C_k and α_k denote material constants calibrated from experimental data. Two back stresses are calibrated to implement Chaboche model and corresponding material characteristics by fitting the stabilised hysteresis loop from experiments [116]. The employed material properties are listed in Table 7.6.

$$\dot{X}_k = C_k \frac{1}{\sigma^0} (\sigma - X) \dot{\bar{\epsilon}}^p - \alpha_k X_k \dot{\bar{\epsilon}}^p \quad (7.7)$$

$$X = \sum_{k=1}^n X_k \quad (7.8)$$

Table 7.6 Material properties for the simulation.

T	E	σ_y	Q	b	C ₁	C ₂	α_1	α_2
600	149.69	205	62.26	42.45	30211.65	4677.23	589.56	80.53

The stress-strain hysteresis loops are generated to verify the Chaboche model by FE simulations under the strain-controlled symmetric cyclic loading with a strain amplitude of 0.6%. The numerical simulation results are compared to an experiment result for the isothermal cyclic test results at 600°C, which agree with the experiment result as shown in Figure 7.14.

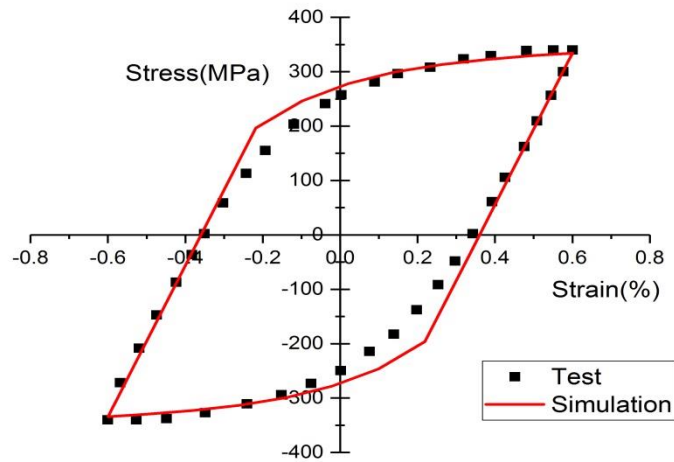


Figure 7.14 Cyclic test result at 600°C [116] and simulation result, $\Delta\varepsilon = \pm 0.6\%$.

For creep behaviour, the Norton-Bailey time hardening law is employed with the following material constants: $A = 5.604 \times 10^{-15} h^{-1}$ at 600°C, $n = 5.769$, and $m = -0.55$. A cyclic thermal load ($\Delta\theta = 1.2\Delta\theta_0$ and $\theta_0 = 300^\circ\text{C}$) and a constant mechanical load ($\sigma_p = 0.5\sigma_{p0}$) are created as a load case 6. The thermal conductivity and expansion coefficient used for the simulation are $21.5 [W/mK]$ and $1.75 \times 10^{-5} [^\circ\text{C}^{-1}]$ respectively. An SBS analysis with the combined hardening parameters is performed under load case 6 for a dwell time of 10hrs.

Table 7.7 Key values and feature at the initial cycle and saturated cycle with load case 6 for a dwell time of 10hr.

LC	$\bar{\sigma}_s$	$\bar{\sigma}_c$	ε_{BR}^c	ε_R^c	ε_L^p	ε_U^p	t_s	Cycle
6	-239	79	-7.43E-04	2.71E-03	-7.84E-04	2.04E-03	0.01	1 st
	-180	78	-6.45E-04	1.19E-03	-2.13E-04	2.79E-03	0.5	10 th

Table 7.7 presents critical values from the simulation results. The analysed data shows that the structural creep recovery mechanism occurs with the Chaboche hardening parameters. Unlike the previous case studies, the peak creep strain does not occur at the concerning location, but the maximum inelastic strain still takes place. It means that the structural creep recovery mechanism affects structural integrity with fatigue damage rather than creep damage.

Figure 7.15 exhibits stress-strain hysteresis loops in a transition from the first cycle to the stabilised cycle. As shown the cyclic hardening in Figure 7.14, the saturated hysteresis loop at 10th cycle has higher maximum stress than the first cycle. Due to asymmetric cyclic loading applied to the structure, the hysteresis loops show a ratchetting response in transition to tensile direction as the cycle goes. Consequently, smaller loading plasticity occurs at the saturated cycle but its unloading plasticity is larger than the first cycle. The short time of t_s has effects on creep strain increment as both the first and the last cycle accumulates small compressive creep strain before structural creep recovery occurs, in particular, the saturated cycle develops smaller than the first cycle due to the relaxation starting from lower stress in magnitude. The first cycle develops more considerable creep strain than the saturated cycle at the similar level of the end of the creep stress within the recovery. This is because the dwell time of the first cycle at the recovery is longer than the saturated cycle.

From this investigation, it is confirmed that the structural creep recovery mechanism can occur with the real hardening model. The cyclic hardening results in the saturated loop move up with Q_∞ in tension from the first cycle. In the assumption of the same transition of the cyclic response, it is expected that cyclic hardening may prevent the structural creep recovery mechanism if the saturated cycle is formed in the tensile domain by increasing of Q_∞ . However, despite the structural creep recovery mechanism could disappear, creep ratchetting remains due to either creep strain or unloading plasticity.

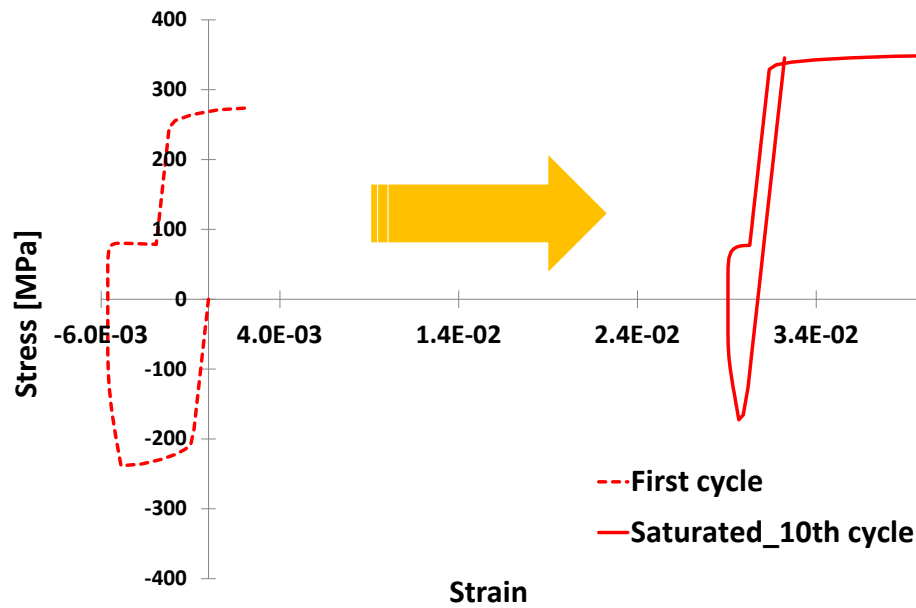


Figure 7.15 Structural responses in a transition from the first cycle to the saturated cycle at the 10th cycle for load case 6.

7.4 Discussions

7.4.1 *Practical Problems Involving the Structural Creep Recovery Mechanism*

As demonstrated in Section 7.3.1, when a structure is subjected to a specific loading condition, the mechanical load that produces the primary stress acting in the opposite direction to the secondary stress can lead to the creep stress redistribution in the structure within a creep dwell. The creep stress redistribution can result in the conversion of the dominant internal stresses which induces the structural creep recovery mechanism. If a high temperature structure meets those conditions, the structural creep recovery mechanism will appear in every operating cycle, which results in negatively affecting the lifetime of the structure with an increase of the total strain range as shown in the previous studies. Hence, it is worthwhile examining practical problems which may have additional potential risks regarding this mechanism.

Components in non-isothermal conditions can be found in forced cooling systems using either air flow or coolant equipment. For example, internal combustion chambers equip with forced cooling systems due to the exposure to high temperature and pressure in operation. Mechanical components comprising the combustion chamber are cylinder liner, piston crown, and valves. It has reported that cracking or fractures with excessive plastic deformation including the creep

are known issues in these components [117, 118]. High temperature heat exchangers can be another practical problem exposing to potential risk, with the thermal gradient between inlet and outlet lines. Thus, steel casings or structures holding tubes or fins are likely vulnerable parts to thermal fatigue damage considering the structural creep recovery mechanism.

Moreover, a metal matrix composite (MMC) material in the elevated temperature may experience a similar problem. Due to the different coefficients of thermal expansion of the two materials, thermally induced internal stresses are imposed on the edges of the metal matrix phase even at the isothermal condition. To avoid the hidden risk, material selection and life assessment of the components are very important.

7.4.2 Limitations of the Elastic Follow-up Factor in the Structural Creep Recovery Mechanism

Elastic follow-up is a term to describe the creep strain accumulation in a local region where resulting in the evolution of the total strain, but majority regions remain elastic behaviours [104]. The relationship between creep stress relaxation and creep strain accumulation shows non-linear behaviours which can be simplified as the elastic follow-up as shown in Eq. (7.9), where Z is the elastic follow up-factor.

$$\frac{d\bar{\varepsilon}^c}{dt} + \frac{Z}{\bar{E}} \cdot \frac{d\bar{\sigma}}{dt} = 0 \quad (7.9)$$

The Z can be defined as a ratio of creep strain increment to elastic strain increment during a creep dwell as Eq.(7.10), and it would be depicted as Figure 7.16, where $\Delta\bar{\varepsilon}_{Tot}$ denotes total strain increment, $\Delta\bar{\sigma}$ is von-Mises equivalent stress drop within a dwell, $\Delta\bar{\varepsilon}^c$ is creep strain increment, and $\Delta\bar{\varepsilon}^e$ is elastic strain increment.

$$Z = -\frac{\Delta\bar{\varepsilon}^c}{\Delta\bar{\varepsilon}^e} = \frac{\Delta\bar{\varepsilon}_{Tot} - \frac{\Delta\bar{\sigma}}{\bar{E}}}{\frac{\Delta\bar{\sigma}}{\bar{E}}} \quad (7.10)$$

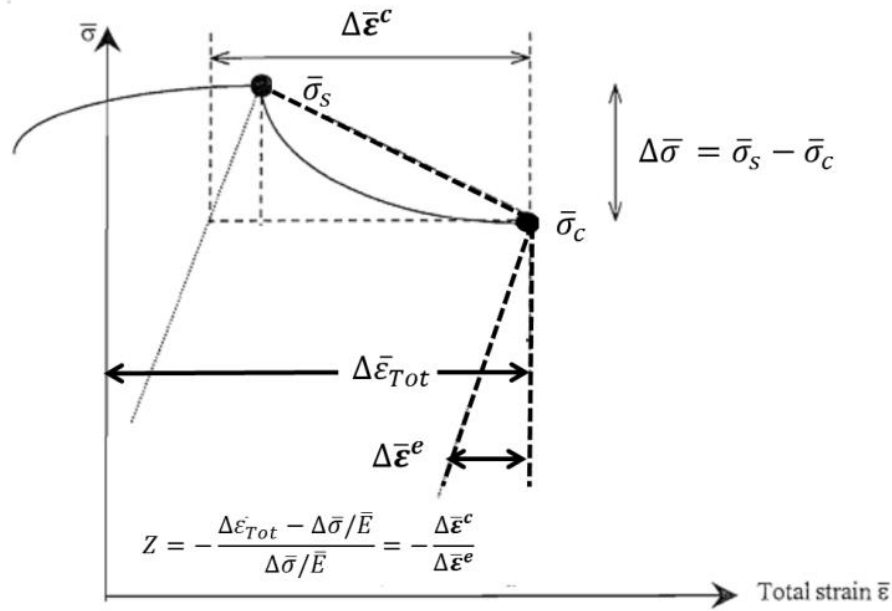


Figure 7.16 Definition of general elastic follow-up factor **Z**.

As a conservative approximation, it can take into account the creep strain increment by multiplying a scalar value of the Z to the elastic strain increment in a range of the creep stress drop instead of solving the non-linear relationship. However, the elastic follow-up factor cannot apply to the structural creep recovery mechanism. As shown the hysteresis loops in Section 7.3, the stress relaxations take place in both compressive and tensile domains within a dwell. Thus, creep strain should not be predicted by using an elastic follow-up factor. Moreover, a formula for a forward creep law to estimate creep stress relaxation against dwell time for an arbitrary value of the elastic follow-up factor will not work either. The formula can be presented as Eq. (7.11), where $\bar{E} = 3E / 2(1 + \nu)$ which is an effective elastic modulus.

$$\bar{\sigma}_c = \left\{ \bar{\sigma}_s^{-n+1} + \frac{1}{Z} \left(\frac{n-1}{m+1} \right) A \bar{E} \Delta t^{m+1} \right\}^{-\frac{1}{n-1}} \quad (7.11)$$

Hence, it is recommended to predict neither creep strain with a value of Z nor the end of creep stress with the formula, if a structure experiences the structural creep recovery mechanism.

7.4.3 *Structural Integrity Assessment in the Presence of the Structural Creep Recovery Mechanism*

Ratchetting is the cyclic accumulation of the inelastic strain with non-zero mean stress amplitude. In the creep regime, the ratchetting should take into account cyclic accumulation of both plastic strain and creep strain. The design codes and assessment procedures propose to assess the plastic ratchetting and creep ratchetting separately [104].

The numerical results show that creep ratchetting may appear in the most case when the holed plate experiences the structural creep recovery mechanism. However, although creep ratchetting response occurs, it should be evaluated which damage has the most critical impact on structural integrity among creep damage, fatigue damage, and ratchetting damage. In this regards, this section suggests appropriate evaluation manners for creep-fatigue damage, provided that if a structure does not fail due to ratchetting in the presence of the structural creep recovery mechanism.

For the damage evaluation, it refers to evaluation methods provided in R5. Notably, for a creep damage evaluation, Stress Modified Ductility Exhaustion (SMDE) method proposed by Spindler[105] is considered due to a high level of predictability of creep damage for stainless steel, rather than TF and DE method. This section aims to deliver a technical suggestion based on R5 procedures for creep-fatigue damage evaluation under the structural creep recovery mechanism, but it does not perform any damage calculations for an example problem.

In R5, a linear damage summation method is used to calculate creep and fatigue damage, which can be defined by Eq. (7.12), where D_c and D_f are creep damage and fatigue damage respectively. If the sum of the damages is more magnificent and equal than 1, failure will occur.

$$D_c + D_f \leq 1 \quad (7.12)$$

The fatigue damage per cycle, d_f , in R5 can be expressed as Eq. (7.13), where N_0 is a number of cycles to create a crack of depth a_0 at the total strain range $\Delta\varepsilon$ and temperature T .

$$d_f = 1/N_0(\Delta\varepsilon, T) \quad (7.13)$$

The creep damage per cycle, d_c , can be estimated using the stress modified ductility exhaustion (SMDE) approach in R5, defined by:

$$d_c^{SMDE} = \int_0^t \frac{\dot{\varepsilon}^c}{\varepsilon_f^c(\dot{\varepsilon}^c, \bar{\sigma}, T)} dt \quad (7.14)$$

where t is the dwell time; t_f is the creep rupture time which is a function of stress and temperature; ε_f^c is creep ductility of a material which is a function of the instantaneous creep strain rate at a given temperature. If the function of ε_f^c includes both stress and the creep strain rate, it implies the SMDE approach.

It requires to consider the healing effect of compressive dwell in order to evaluate creep-fatigue damage of the structural creep recovery mechanism for austenitic stainless steel [119]. The effect demonstrates that the sintering of creep cavities under compressive creep stress may be able to compensate the creep damage cumulated under tensile creep stress. Three critical dwell time increments need to be distinguished in order to apply the healing effect to the structural creep recovery mechanism, which is: time for the stress relaxation being reversed in sign (t_s), time for creep strains to be fully recovered (t_r), and end of dwell time (t).

For dwell time of t_s , creep damage in a tensile sign domain needs to be taken into account, whereas it could be negligible in a compressive sign domain because creep cavity cannot nucleate. Also, fatigue damage will increase within a cycle due to the end of creep stress becoming zero. For dwell time of t_r , the same tensile creep strain is accumulated to compressive creep strain within the dwell, accumulating physically zero creep strain. Hence, the fatigue damage should be enhanced without consideration of any creep damage. For dwell time beyond t_r and up to the end of dwell time t , creep damage in a tensile domain after the time of t_r requires consideration along with fatigue damage corresponding to total strain range, otherwise only the fatigue damage to be considered without any creep damage in a compressive domain.

When it comes to the holed plate problem, with the creep dwell starting from a compressive stress, it is suggested that creep damage within the time increment from t_r to t only requires consideration, and Eq.(7.13) can be used for fatigue damage calculation affiliated with total strain range in view of the healing effect and a direction of creep-ratcheting heading to tensile. On the contrary, if it is starting from tensile stress, creep damage needs to be considered only within dwell time of t_s , otherwise creep damage within a cycle can be negligible if the dwell time beyond t_s . Within dwell time of t_r , Eq.(7.13) is still applicable to fatigue damage calculation. However, for a dwell time of t , the fatigue damage should be enhanced by replacing N_0 to N_g in Eq.(7.13) considering a direction of the creep-ratcheting moving to compressive, where N_g is the number of cycles to grow a fatigue crack from 0.02mm to a_0 [104]. It is reasonable for the nucleation phases to be removed under compressive stress.

7.2 Chapter Summary

The structural creep recovery mechanism (SCRM) was identified by the full incremental cyclic analysis for a benchmark problem of 3D holed plate subjected to cyclic thermal load and constant mechanical load. From the analysis results, the combined thermo-mechanical load imposes the secondary compressive stress and primary tensile stress on the plate at loading. Due to the primary stress acting in the opposite direction to the secondary stress, the assessed point of the holed plate experiences significant stress relaxation as it reverses the sign of the creep stress within a dwell due to creep stress redistribution. As a result, compressive and tensile creep strains are developed sequentially during creep dwell, leading to structural creep strain recovery.

Parametric studies demonstrated that structural creep recovery is a possible mechanism within a creep dwell, provided that the secondary stress dominates the primary stress at the assessment point when loading. It showed that the constant mechanical load level has effects on time for recovery to occur and the magnitude of the end of creep stress. The numerical investigations validated the structural creep recovery mechanism using the effective material properties such as temperature dependent mechanical properties, Chaboche hardening model, and Norton-Bailey creep parameters.

The potential risks that can induce SCRM were discussed, which are the high temperature components equipped with a forced cooling system and MMC materials that have different

thermal coefficients of expansion. If a structure experiences SCRM, the classical elastic follow-up factor and the formula Eq.(7.11) are not applicable to predicting the creep strain accumulation and the end of creep stress respectively. In the presence of SCRM, it suggested that creep damage should be reduced or neglected for a dwell in which either physically zero creep strains develop or compressive creep strains are larger than tensile creep strain, considering the healing effect of austenitic stainless steel. On the other hand, fatigue damage tends to increase due to significant creep enhanced plasticity. In particular, when the compressive creep dwell is dominant within a cycle, the fatigue damage should be further enhanced by replacing N_0 to N_g . Consequently, the structural creep recovery mechanism causes significant unloading plasticity which affects the structural integrity with enhanced fatigue damage.

8. Conclusions

The key deliverables of this thesis are the investigation of cyclic plasticity and creep-cyclic plasticity of high temperature engineering components that have not been studied before, the development of the LMM Framework to expand its applicability, and the introduction to new high temperature failure mechanism. **Major Conclusions** of this work are presented below:

Shakedown and ratchet boundaries of 90° back-to-back pipe bends (10inches NPS Schedule 40 STD) subjected to cyclic thermo-mechanical loading with constant internal pressures were investigated in Chapter 4 using the LMM. Numerical results present the effects of load combinations on shakedown and ratchet boundaries. Results showed that cyclic bending makes more impacts on the integrity of the double pipe bends than constant internal pressures; particularly cyclic in-plane bending affects the integrity more than cyclic out-of-plane bending. The horizontal pipe section makes significant impacts on the limit pressures but minimal on the reverse plasticity limits. Cyclic thermal load makes equivalent impacts to the cyclic bending on the pipe bends integrity. Therefore, the effects of the thermal stress require serious consideration on the integrity assessment of the pipe bends structure. The parametric studies in associated with geometry effects of the pipe bends showed that variations of r/t & R/r ratios have a negligible influence to reverse plasticity limit under cyclic thermal load, whereas significantly influences under cyclic bending moments. In particular, four semi-empirical equations were derived from numerical results of the parametric studies, which can be utilised to predict shakedown boundary without performing the complex finite element analysis.

Creep-cyclic plasticity behaviours of Particle Reinforced Titanium Matrix Composites (PRTMCs) material subjected to cyclic thermo-mechanical load were investigated utilising the LMM eDSCA in Chapter 5. Numerical results clarified the effects of spatial particle distribution, the number of particles N_{part} and particle volume fraction V_f on the material response. Results showed that all RVE models analysed show creep ratchetting responses due to cyclically enhanced creep, despite a cyclic load point applied is under the strict shakedown limit. In additions, the numerical results demonstrate that tailoring of the reinforcement arrangement affects the high temperature damage tolerance substantially. As results, variations of V_f and N_{part} have no direct influences on creep or ratchetting endurance, but tensile load level has significant impacts on both creep strain and ratchetting strain increment due to cyclic creep effects. In the case of RVE with a fixed particle arrangement, variations of V_f have influences on a magnitude of a stress range in the steady-state cycle, notably the larger N_{part}

augments the total strain range for the same volume fraction. Based on the numerical results, it is expected that an RVE model that has a smaller V_f may have outstanding creep endurance.

Creep-cyclic plasticity behaviour and creep-fatigue damages of a superheater outlet tube plate subjected to thermo-mechanical load were investigated employing the modified LMM eDSCA in Chapter 6. The modified LMM eDSCA produced reliable results in creep stress and principal stress relaxation histories, temperature dependent creep parameters within the multiple dwell periods. Under the given loading condition and dwell time, maximum tensile creep deformation occurs at the tube holed area for the 1st dwell and maximum compressive creep deformation occurs at the inside fillet edges of the tube plate for the 2nd dwell. For creep damage evaluation, Time Fraction (TF), Ductility Exhaustion (DE), and Strain Energy Ductility Exhaustion (SEDE) methods were employed with Multiaxial Ductility Factors (MDF). For fatigue damage assessment, Modified Universal Slope Method (MUSM), and Design Fatigue Curve provided in ASME NH were considered. According to the linear damage summation (LDS) method, total damage per cycle is extensive in order of DE, SEDE, and TF which is the same order as creep damage per cycle. The criticality of the total damage is the same as the experimental results reported by Takahashi *et al.*. Multiaxial ductility factor MDF_{WEN} tends to predict more substantial creep damage than MDF provided in R5. The unified creep-fatigue equation evaluates considerably smaller total damage per cycle compared to the linear damage summation method.

The critical failure mechanism, the structural creep recovery phenomenon, were identified by the full incremental cyclic analysis for a benchmark problem of a three-dimensional holed plate model subjected to cyclic thermal load and constant mechanical load in Chapter 7. The structural creep recovery mechanism (SCRM) can occur by creep enhanced plasticity due to stress redistribution across a high temperature component. Parametric studies with the combined hardening model and temperature dependent material parameters have demonstrated that structural creep recovery is a possible mechanism within a creep dwell. It can be found the potential risks associated with this failure mechanism from high temperature components equipped with a forced cooling system, and MMCs materials exposed to a high temperature which has different thermal coefficients of expansion. In the presence of the structural creep recovery mechanism, the existent elastic follow-up factor for creep strain estimation is not applicable, and the fatigue damage for stainless steel material should be enhanced due to dominant compressive stress over a loading cycle.

Finally, this thesis offers valuable insights into structural behaviours of the high temperature component and the futuristic engineering material and demonstrates that the LMM Framework can be a powerful analysis tool for practical problems in high temperature industry.

8.1 Future Work

To make these results more reliable and the analysis tool more powerful, the areas that have been identified as requiring **Future Work** is described below:

In Chapter 4, shakedown and ratchet boundaries were analysed by the LMM and the LMM DSCA respectively with the elastic-perfectly plastic (EPP) model and isotropic hardening. The EPP model may provide over conservative plastic deformation for a material showing cyclic hardening characteristic, but less conservative for a material showing cyclic softening. In reality, materials show combined isotropic and kinematic hardening behaviours under cyclic load, which real shakedown and ratchet boundaries have a load-bearing capacity more than the results with the EPP model. However, the current LMM is not able to consider the combined hardening behaviour. Hence it requires further development of the LMM which enables to consider Ramberg-Osgood parameters and kinematic hardening behaviour, in the shakedown analysis.

In Chapter 6, the main novelty of the research is to analyse the creep-cyclic plasticity behaviour of the tube plate and to predict creep-fatigue damage, through the modified LMM eDSCA. The modified LMM eDSCA is the extended version of the original LMM eDSCA which was designed to calculate creep deformation using mathematically derived equations that combine the time hardening power law and elastic follow-up. Thus it has limitations in calculating creep deformation using other creep constitutive models, such as the strain hardening power law, the exponential law, and the hyperbolic sine law. Further modifications implementing the other creep constitutive models into the LMM eDSCA will be needed, which allow calculating more accurate creep deformation for materials that show different creep process. Besides, it requires implementation of the post-processing code for creep-fatigue damage assessment developed in the modified LMM eDSCA into Plug-In software provided in Abaqus for user easy to utilise.

In Chapter 7, the LMM eDSCA calculate creep deformation with assumptions that creep stress relaxation follows the elastic follow-up, but the structural creep recovery mechanism has the

significant stress relaxation that causes changes in the sign of creep stress within a dwell period, which the elastic follow-up cannot express the relaxation. Thus the structural creep recovery mechanism was identified by the conventional full incremental cyclic analysis. However, the LMM eDSCA is very flexible numerical procedures, and it can be modified to calculate creep deformation under the significant relaxation.

References

1. Saito, S., *Role of nuclear energy to a future society of shortage of energy resources and global warming*. Journal of Nuclear Materials, 2010. **398**(1): p. 1-9.
2. Buckthorpe, D., *1 - Introduction to Generation IV nuclear reactors*, in *Structural Materials for Generation IV Nuclear Reactors*, P. Yvon, Editor. 2017, Woodhead Publishing. p. 1-22.
3. Sabharwall, P., S.M. Bragg-Sitton, and C. Stoots, *Challenges in the development of high temperature reactors*. Energy Conversion and Management, 2013. **74**: p. 574-581.
4. Ohshima, H. and S. Kubo, *5 - Sodium-cooled fast reactor*, in *Handbook of Generation IV Nuclear Reactors*, I.L. Pioro, Editor. 2016, Woodhead Publishing. p. 97-118.
5. Tomkins, B. and M.F. Hamza, *Structural Integrity Issues in the Nuclear Industry*, in *Reference Module in Materials Science and Materials Engineering*. 2017, Elsevier.
6. Viswanathan, R. *An overview of failure mechanisms in high temperature components in power plants*. in *ICF10, Honolulu (USA) 2001*. 2013.
7. Koul, A. and W. Wallace, *Importance of Physics-based Prognosis for Improving Turbine Reliability Part 2: A Turbine Disc Case Study in a Fleet Environment* by. 2018.
8. Vardar, N. and A. Ekerim, *Failure analysis of gas turbine blades in a thermal power plant*. Engineering Failure Analysis, 2007. **14**(4): p. 743-749.
9. Lupinc, V., *Creep and Fatigue in High Temperature Alloys*, 1981: p. 7-40.
10. Viswanathan, R. and J. Stringer, *Failure mechanisms of high temperature components in power plants*. Journal of engineering materials and technology, 2000. **122**(3): p. 246-255.
11. NH-Boiler, A. and P.V. Code, *Section III, Division 1, Subsection NH, Class 1 Components in Elevated Temperature Service*. American Society of Mechanical Engineers, New York, NY, 2009.
12. Ainsworth, R., *R5: Assessment procedure for the high temperature response of structures*. British energy generation Ltd, 2003. **3**.
13. Chen, H. and A. Ponter, *The 3-D shakedown and limit analysis using the linear matching method*. Int. J. Pressure Vessels Piping, 2002. **78**: p. 443-451.

14. Habibullah, M.S. and A. Ponter, *Ratchetting limits for cracked bodies subjected to cyclic loads and temperatures*. Engineering fracture mechanics, 2005. **72**(11): p. 1702-1716.
15. Barbera, D., H.F. Chen, and Y.H. Liu, *Creep fatigue life assessment of a pipe intersection with dissimilar material joint by linear matching method*. Applied Mechanics and Materials, 2016. **853**: p. 366-371.
16. Gorash, Y. and H. Chen, *Creep-fatigue life assessment of cruciform weldments using the linear matching method*. International Journal of Pressure Vessels and Piping, 2013. **104**: p. 1-13.
17. Jackson, G., H. Chen, and D. Tipping, *Shakedown and creep rupture assessment of a header branch pipe using the Linear Matching Method*. Procedia Engineering, 2015. **130**: p. 1705-1718.
18. Chen, H., W. Chen, and J. Ure, *A direct method on the evaluation of cyclic steady state of structures with creep effect*. Journal of Pressure Vessel Technology, 2014. **136**(6): p. 061404.
19. Beesley, R., H. Chen, and M. Hughes, *On the modified monotonic loading concept for the calculation of the cyclic j -integral*. Journal of Pressure Vessel Technology, 2015. **137**(5): p. 051406.
20. Lytwyn, M., H. Chen, and M. Martin, *Comparison of the Linear Matching Method to Rolls-Royce's Hierarchical Finite Element Framework for ratchet limit analysis*. International Journal of Pressure Vessels and Piping, 2015. **125**: p. 13-22.
21. Ure, J., H. Chen, and D. Tipping, *Verification of the linear matching method for limit and shakedown analysis by comparison with experiments*. Journal of Pressure Vessel Technology, 2015. **137**(3): p. 031003.
22. Melan, E., *Theorie statisch unbestimmter Systeme aus ideal-plastischem Baustoff*. 1936: Hölder-Pichler-Tempsky in Komm.
23. Koiter, W.T., *General theorems for elastic-plastic solids*. 1960: North-Holland Amsterdam.
24. Manson, S., *Fatigue: a complex subject—some simple approximations*. Experimental mechanics, 1965. **5**(4): p. 193-226.
25. Muralidharan, U. and S. Manson, *A modified universal slopes equation for estimation of fatigue characteristics of metals*. Journal of Engineering Materials and Technology, 1988. **110**(1): p. 55-58.
26. Lee, K.-S. and J.-H. Song, *Estimation methods for strain-life fatigue properties from hardness*. International Journal of Fatigue, 2006. **28**(4): p. 386-400.

27. Ong, J., *An improved technique for the prediction of axial fatigue life from tensile data*. International Journal of Fatigue, 1993. **15**(3): p. 213-219.
28. Mitchell, M., *Fundamentals of modern fatigue analysis for design*. 1996.
29. Park, J.-H. and J.-H. Song, *New estimation method of fatigue properties of aluminum alloys*. Journal of engineering materials and technology, 2003. **125**(2): p. 208-214.
30. Baumel Jr, A. and T. Seeger, *Materials data for cyclic loading. Supplement 1*. Elsevier Science Publishers, P. O. Box 211, 1000 AE Amsterdam, The Netherlands, 1990., 1990.
31. Meggiolaro, M. and J. Castro, *Statistical evaluation of strain-life fatigue crack initiation predictions*. International Journal of Fatigue, 2004. **26**(5): p. 463-476.
32. RCC-MRx, A., *Code of Design and Construction Rules for Mechanical Component in Nuclear Installations*. 2013.
33. Boyle, J.T. and J. Spence, *Stress analysis for creep*. 2013: Elsevier.
34. Meng, Q. and Z. Wang, *Creep damage models and their applications for crack growth analysis in pipes: A review*. Engineering Fracture Mechanics, 2016.
35. Bree, J., *Elastic-plastic behaviour of thin tubes subjected to internal pressure and intermittent high-heat fluxes with application to fast-nuclear-reactor fuel elements*. The Journal of Strain Analysis for Engineering Design, 1967. **2**(3): p. 226-238.
36. Barbera, D., H. Chen, and Y. Liu, *Advances on creep-fatigue damage assessment in notched components*. Fatigue & Fracture of Engineering Materials & Structures, 2017.
37. Cho, N.-K. and H. Chen. *Investigation of structural creep strain recovery and its impact on structural integrity*. in *24th International Conference on Structural Mechanics in Reactor Technology*. 2017.
38. Cho, N.-K., et al., *Enhanced fatigue damage under cyclic thermo-mechanical loading at high temperature by structural creep recovery mechanism*. International Journal of Fatigue, 2018.
39. Barbera, D., H. Chen, and Y. Liu, *On Creep Fatigue interaction of components at elevated temperature*. Journal of Pressure Vessel Technology, 2016. **138**(4): p. 041403.
40. Spindler, M.W., *An improved method for calculation of creep damage during creep-fatigue cycling*. Materials Science and Technology, 2013. **23**(12): p. 1461-1470.
41. Takahashi, Y., B. Dogan, and D. Gandy. *Systematic evaluation of creep-fatigue life prediction methods for various alloys*. in *ASME 2009 Pressure Vessels and Piping Conference*. 2009. American Society of Mechanical Engineers.

42. Liu, D., D.J. Pons, and E.-h. Wong, *The unified creep-fatigue equation for stainless steel 316*. Metals, 2016. **6**(9): p. 219.
43. Holmström, S. and P. Auerkari, *A robust model for creep-fatigue life assessment*. Materials Science and Engineering: A, 2013. **559**: p. 333-335.
44. Manson, S., *A simple procedure for estimating high-temperature low-cycle fatigue*. Experimental Mechanics, 1968. **8**(8): p. 349-355.
45. Wilshire, B., P. Scharning, and R. Hurst, *A new approach to creep data assessment*. Materials Science and Engineering: A, 2009. **510**: p. 3-6.
46. Asayama, T. and Y. Tachibana, *Collect available creep-fatigue data and study existing creep-fatigue evaluation procedures for Grade 91 and Hastelloy XR*. 2007, ASME Standards Technology, LLC.
47. Pétesch, C., et al. *RCC-MRx edition 2015: Overview of three years of developments*. in *ASME 2015 Pressure Vessels and Piping Conference*. 2015. American Society of Mechanical Engineers.
48. Mackenzie, D., J. Boyle, and R. Hamilton, *The elastic compensation method for limit and shakedown analysis: a review*. The Journal of Strain Analysis for Engineering Design, 2000. **35**(3): p. 171-188.
49. Dhalla, A. *A simplified procedure to classify stresses for elevated temperature service*. in *ASME transactions, PVP division conference*. 1987.
50. Seshadri, R., *Inelastic evaluation of mechanical and structural components using the generalized local stress strain method of analysis*. Nuclear Engineering and Design, 1995. **153**(2-3): p. 287-303.
51. Chen, H. and A.R. Ponter, *Shakedown and limit analyses for 3-D structures using the linear matching method*. International Journal of Pressure Vessels and Piping, 2001. **78**(6): p. 443-451.
52. Yang, P., et al., *Limit analysis based on a modified elastic compensation method for nozzle-to-cylinder junctions*. International Journal of Pressure Vessels and Piping, 2005. **82**(10): p. 770-776.
53. Muscat, M. and D. Mackenzie, *Elastic-shakedown analysis of axisymmetric nozzles*. Journal of pressure vessel technology, 2003. **125**(4): p. 365-370.
54. Muscat, M., R. Hamilton, and J. Boyle, *Shakedown analysis for complex loading using superposition*. The Journal of Strain Analysis for Engineering Design, 2002. **37**(5): p. 399-412.
55. Polizzotto, C., *On the Conditions to Prevent Plastic Shakedown of Structures: Part I—Theory*. Journal of applied mechanics, 1993. **60**(1): p. 15-19.

56. Abdalla, H.F., M.M. Megahed, and M.Y. Younan, *A simplified technique for shakedown limit load determination*. Nuclear Engineering and Design, 2007. **237**(12): p. 1231-1240.
57. Chen, H. and A.R. Ponter, *Linear Matching Method on the evaluation of plastic and creep behaviours for bodies subjected to cyclic thermal and mechanical loading*. International Journal for Numerical Methods in Engineering, 2006. **68**(1): p. 13-32.
58. Chen, H. and A.R. Ponter, *A direct method on the evaluation of ratchet limit*. Journal of Pressure Vessel Technology, 2010. **132**(4): p. 041202.
59. Chen, H. and A.R. Ponter, *A method for the evaluation of a ratchet limit and the amplitude of plastic strain for bodies subjected to cyclic loading*. European Journal of Mechanics-A/Solids, 2001. **20**(4): p. 555-571.
60. Beesley, R., H. Chen, and M. Hughes, *A novel simulation for the design of a low cycle fatigue experimental testing programme*. Computers & Structures, 2017. **178**: p. 105-118.
61. Barbera, D., H. Chen, and Y. Liu, *Creep-fatigue behaviour of aluminum alloy-based metal matrix composite*. International Journal of Pressure Vessels and Piping, 2016. **139-140**: p. 159-172.
62. Giugliano, D.B., D.; Chen, H.; Cho, N.; Liu, Y.;; *Creep-fatigue and cyclically enhanced creep mechanisms in aluminium based Metal Matrix Composites*. 2018.
63. Wen, J.-F., et al., *Effects of stress level and stress state on creep ductility: evaluation of different models*. Journal of Materials Science & Technology, 2016. **32**(8): p. 695-704.
64. Li, J., et al., *Plastic limit loads for pipe bends under combined bending and torsion moment*. International Journal of Mechanical Sciences, 2015. **92**: p. 133-145.
65. Li, J., et al., *Limit loads for pipe bends under combined pressure and out-of-plane bending moment based on finite element analysis*. International Journal of Mechanical Sciences, 2014. **88**: p. 100-109.
66. Li, S.-J., et al., *Effect of bend angle on plastic limit loads of pipe bends under different load conditions*. International Journal of Mechanical Sciences, 2017. **131**: p. 572-585.
67. Leu, S.-Y. and J.-S. Li, *Shakedown analysis of truss structures with nonlinear kinematic hardening*. International Journal of Mechanical Sciences, 2015. **103**: p. 172-180.

68. Peng, H., et al., *Shakedown analysis of engineering structures under multiple variable mechanical and thermal loads using the stress compensation method*. International Journal of Mechanical Sciences, 2018. **140**: p. 361-375.
69. Surmiri, A., A. Nayebi, and H. Rokhghireh, *Shakedown-ratcheting analysis of Bree's problem by anisotropic continuum damage mechanics coupled with nonlinear kinematic hardening model*. International Journal of Mechanical Sciences, 2018. **137**: p. 295-303.
70. Zheng, X., H. Chen, and Z. Ma, *Shakedown boundaries of multilayered thermal barrier systems considering interface imperfections*. International Journal of Mechanical Sciences, 2018. **144**: p. 33-40.
71. Abdalla, H.F., *Shakedown boundary determination of a 90° back-to-back pipe bend subjected to steady internal pressures and cyclic in-plane bending moments*. International Journal of Pressure Vessels and Piping, 2014. **116**: p. 1-9.
72. Abdalla, H.F. *Shakedown Boundary of a 90–Degree Back–to–Back Pipe Bend Subjected to Steady Internal Pressures and Cyclic Out–of–Plane Bending Moments*. in *ASME 2014 Pressure Vessels and Piping Conference*. 2014. American Society of Mechanical Engineers.
73. Chen, H., et al., *Shakedown and limit analysis of 90 pipe bends under internal pressure, cyclic in-plane bending and cyclic thermal loading*. International Journal of Pressure Vessels and Piping, 2011. **88**(5): p. 213-222.
74. Chen, X., B. Gao, and G. Chen, *Ratcheting study of pressurized elbows subjected to reversed in-plane bending*. Journal of Pressure Vessel Technology, 2006. **128**(4): p. 525-532.
75. Cho, N.-K. and H. Chen, *Shakedown, ratchet, and limit analyses of 90° back-to-back pipe bends under cyclic in-plane opening bending and steady internal pressure*. European Journal of Mechanics-A/Solids, 2017.
76. Oh, C.-S., Y.-J. Kim, and C.-Y. Park, *Shakedown limit loads for elbows under internal pressure and cyclic in-plane bending*. International Journal of Pressure Vessels and Piping, 2008. **85**(6): p. 394-405.
77. Huang, L. and L. Geng, *Discontinuously Reinforced Titanium Matrix Composites: Microstructure Design and Property Optimization*. 2017: Springer.
78. Zhang, C., et al., *Evolution of microstructure and tensile properties of in situ titanium matrix composites with volume fraction of (TiB+ TiC) reinforcements*. Materials Science and Engineering: A, 2012. **548**: p. 152-160.

79. Tjong, S.C. and Y.-W. Mai, *Processing-structure-property aspects of particulate- and whisker-reinforced titanium matrix composites*. Composites Science and Technology, 2008. **68**(3-4): p. 583-601.
80. Yang, Z., et al., *In situ synthesis of hybrid and multiple-dimensioned titanium matrix composites*. Journal of alloys and compounds, 2006. **419**(1-2): p. 76-80.
81. Liu, D., et al., *High temperature mechanical properties of a laser melting deposited TiC/TiAl5 titanium matrix composite*. Journal of Alloys and Compounds, 2010. **496**(1-2): p. 189-195.
82. Huang, L., L. Geng, and H. Peng, *Microstructurally inhomogeneous composites: is a homogeneous reinforcement distribution optimal?* Progress in Materials Science, 2015. **71**: p. 93-168.
83. Giugliano, D., D. Barbera, and H. Chen, *Effect of fiber cross section geometry on cyclic plastic behavior of continuous fiber reinforced aluminum matrix composites*. European Journal of Mechanics - A/Solids, 2017. **61**: p. 35-46.
84. He, T., et al., *Effect of particle size ratio on microstructure and mechanical properties of aluminum matrix composites reinforced with Zr₄₈Cu₃₆Ag₈Al₈ metallic glass particles*. Materials Science and Engineering: A, 2019. **742**: p. 517-525.
85. Kimmig, S. and J.-H. You, *Cyclic plastic behavior of unidirectional SiC fibre-reinforced copper composites under uniaxial loads: An experimental and computational study*. Composite Structures, 2018.
86. Böhm, H.J. and W. Han, *Comparisons between three-dimensional and two-dimensional multi-particle unit cell models for particle reinforced metal matrix composites*. Modelling and Simulation in Materials Science and Engineering, 2001. **9**(2): p. 47.
87. Han, W., A. Eckschlager, and H.J. Böhm, *The effects of three-dimensional multi-particle arrangements on the mechanical behavior and damage initiation of particle-reinforced MMCs*. Composites science and technology, 2001. **61**(11): p. 1581-1590.
88. Segurado, J., J. LLorca, and C. González, *On the accuracy of mean-field approaches to simulate the plastic deformation of composites*. Scripta Materialia, 2002. **46**(7): p. 525-529.
89. Gentile, L.G., D.; Cestino, E.; Frulla, G.; Minisci, E.,, *OPTIMISATION BASED ANALYSIS OF THE EFFECT OF PARTICLE SPATIAL DISTRIBUTION ON THE ELASTIC BEHAVIOUR OF PRMMC*. ECCM-6th European Conference on

- Computational Mechanics (Solids, Structures and Coupled Problems)-Glasgow, 2017.
90. Al Kassem, G. and D. Weichert, *Micromechanical material models for polymer composites through advanced numerical simulation techniques*. PAMM, 2009. **9**(1): p. 413-414.
 91. Giugliano, D., et al., *Cyclic plasticity and creep-cyclic plasticity behaviours of the SiC/Ti-6242 Particulate Reinforced Titanium Matrix Composites under thermo-mechanical loadings*. Composite Structures, 2019.
 92. Giugliano, D.C., Nak-Kyun; Chen, Haofeng. , *Cyclic plasticity and creep-cyclic plasticity behaviours of the SiC/Ti-6242 Particulate Reinforced Titanium Matrix Composites under thermo-mechanical loadings*. Composite Structures (Under Review), 2018.
 93. Badea, L., et al., *Creep behavior of Ti-6Al-4V from 450° C to 600° C*. University Polytechnica of Bucharest Scientific Bulletin, Series B, 2014. **76**(1): p. 185-196.
 94. Sonntag, R.E., et al., *Fundamentals of thermodynamics*. Vol. 6. 1998: Wiley New York.
 95. Jiuyi, L., Q. Caifu, and L. Huifang, *Thermal stress analysis on the thick tubesheet with square layout of tubes*. International Journal on Interactive Design and Manufacturing (IJIDeM), 2018. **12**(1): p. 243-251.
 96. Zhang, K., et al., *5 - Boiler design for ultra-supercritical coal power plants*, in *Ultra-Supercritical Coal Power Plants*, D. Zhang, Editor. 2013, Woodhead Publishing. p. 104-130.
 97. Barbera, D., H.F. Chen, and Y.H. Liu, *On the Creep Fatigue Behavior of Metal Matrix Composites*. Procedia Engineering, 2015. **130**: p. 1121-1136.
 98. Spindler, M., *ECCC Data Sheets 2014*. UK: ETD Ltd, 2014. **47**(2).
 99. Spindler, M., *The multiaxial creep ductility of austenitic stainless steels*. Fatigue & fracture of engineering materials & structures, 2004. **27**(4): p. 273-281.
 100. Spindler, M., *An Improved Method to Calculate the Creep-Fatigue Endurance of Type 316H Stainless Steel*. 2006. 1673-1682.
 101. Huang, J.-Y., et al., *High-cycle fatigue behavior of type 316L stainless steel*. Materials transactions, 2006. **47**(2): p. 409-417.
 102. Zinkle, S.J. and G. Was, *Materials challenges in nuclear energy*. Acta Materialia, 2013. **61**(3): p. 735-758.
 103. Skelton, R., *Crack initiation and growth during thermal transients*, in *Component Reliability under Creep-Fatigue Conditions*. 1998, Springer. p. 17-86.

104. Ainsworth, R.A. and R5_Panel, *Assessment procedure for the high temperature response of structures*, in *EDF Energy Nuclear Generation Ltd.* 2014.
105. Spindler, M., *An improved method for calculation of creep damage during creep-fatigue cycling*. *Materials Science and Technology*, 2007. **23**(12): p. 1461-1470.
106. White, P. *The fast reactor state variable model for cyclic inelastic analysis of type 316 stainless steel*. in *Transactions of the 12. international conference on Structural Mechanics in Reactor Technology (SMiRT). Volume L: Inelastic behaviour of solids and structures*. 1993.
107. Miller, D., C. Hamm, and J. Phillips, *A mechanistic approach to the prediction of creep-dominated failure during simultaneous creep-fatigue*. *Materials Science and Engineering*, 1982. **53**(2): p. 233-244.
108. A Fookes, S.X.L., D J Smith, and M W Spindler, *Stress Relaxation during Dwells for Creep and Fatigue Cycling of Type 316H Stainless Steel at 550°C*, in *2nd Int. ECCC Conf., Creep & Fracture in High Temperature Components - Design & Life Assessment*. 2009.
109. Bolton, J., *The consequences of recovery for the analysis of creep in steel structures*. *International Journal of Pressure Vessels and Piping*, 2010. **87**(5): p. 266-273.
110. Chaboche, J.-L., *Constitutive equations for cyclic plasticity and cyclic viscoplasticity*. *International journal of plasticity*, 1989. **5**(3): p. 247-302.
111. Chaboche, J.-L., *On some modifications of kinematic hardening to improve the description of ratchetting effects*. *International journal of plasticity*, 1991. **7**(7): p. 661-678.
112. Lemaitre, J. and J.-L. Chaboche, *Mechanics of solid materials*. 1994: Cambridge university press.
113. Dean, J., et al., *A procedure for extracting primary and secondary creep parameters from nanoindentation data*. *Mechanics of Materials*, 2013. **65**: p. 124-134.
114. Jin, S., H. Harmuth, and D. Gruber, *Compressive creep testing of refractories at elevated loads—Device, material law and evaluation techniques*. *Journal of the European Ceramic Society*, 2014. **34**(15): p. 4037-4042.
115. Manson, S. and G.R. Halford, *Fatigue and durability of metals at high temperatures*. 2009: ASM International.
116. Gong, Y., et al., *Determination of material properties in the Chaboche unified viscoplasticity model*. *Proceedings of the Institution of Mechanical Engineers, Part L: Journal of Materials: Design and Applications*, 2010. **224**(1): p. 19-29.

117. Fakaruddin, M.A., A.M. Hafiz, and K. Karmegam, *MATERIALS SELECTION FOR WET CYLINDER LINER*. IOSR Journal of Engineering (IOSRJEN) e-ISSN, 2012: p. 2250-3021.
118. GONERA, M. and O. SANDIN, *Thermal Analysis of a Diesel Piston and Cylinder Liner using the Inverse Heat Conduction Method*.
119. Wells, C. and C. Sullivan, *Interactions between creep and low-cycle fatigue in Udimet 700 at 1400 F*, in *Fatigue at high temperature*. 1969, ASTM International.